Conducting CO_2 reduction at a bipolar membrane electrode assembly

Combining known technological niches to achieve higher current densities

A master thesis by

M. Sassenburg

In partial fulfilment of the requirements for the degree of

Master of Science
in Sustainable Energy Technology

at the Delft University of Technology

To be defended at
9:30 May 14, 2018

Supervisors:	Dr. W.A. Smith Dr. ir. D.A. Vermaas
Thesis Committee	Prof. dr. B. Dam
Daily supervisor:	Ir. M. Blommaert

TU Delft Delft University of Technology

Abstract

A comparative study of three different membrane electrode assemblies for electrochemical CO_2 reduction is performed in a flowcell setup utilizing gaseous CO_2 as a reagent. The membrane electrode assembly consists of a bipolar or exchange membrane, an Ag-mesh catalyst and a gas diffusion layer. The counterreaction occurring on the opposite of the electrode assembly is oxygen evolution performed in a 1 M KOH anolyte. While using a fixed cell potential of 2.5 V, it was found that the bipolar membrane configuration produces 4 to 6 times more current versus an anion exchange membrane assembly due to the low local pH enabled at the cathode due to the bipolar membrane. This difference comparatively benefitted both CO_2 reduction and the competing H_2 evolution. It was further found that the surrounding infrastructure, namely the titanium sample holder, was almost exclusively performing H_2 evolution, both inhibiting reactions on the Ag-mesh and preventing the formed products from being transported to the cathodic gas phase. Instead, all formed products were detected in the anolyte compartment. To circumvent these issues the sample holder was removed, and ionomer solution was applied to the Ag-mesh increase conductivity between the bipolar membrane and the Ag catalyst. During operation the membrane ultimately delaminated due to internal gas accumulation. The main conclusions from this work are that the examined membrane electrode assemblies using Ag-mesh as a cathode are unable to perform CO_2 reduction while the Ag-mesh is located too far from the gas diffusion layer. Even with layer compression between all components, only trace amounts of CO were produced, implying that contact between the CO_2 reduction catalyst and the CO_2 source was not sufficiently present. Membrane electrode assemblies might then be improved by utilising a layer of conductive liquid between the membrane and Ag-mesh. In an alternative approach a gas diffusion electrode was produced through the sputtering of Ag directly onto the gas diffusion layer. Even without optimisation this system outperformed all produced membrane electrode assemblies in terms of CO_2 reduction.

Keywords: CO_2 reduction, bipolar membrane, BPM, anion exchange membrane, AEM, membrane electrode assembly, MEA, flowcell, gas diffusion electrode.

Table of Contents

List of symbols and abbreviations

AEM = anion exchange membrane

AEMEA = anion exchange membrane electrode assembly

BPM = bipolar membrane

BPMEA = bipolar membrane electrode assembly

C-C bond = carbon-carbon bond (molecular binding)

CC(U)S = carbon capture (utilization) and storage

C.D. = current density

CEM = cation exchange membrane

CO_2RR = CO_2 reduction reaction

DMAc = N,N-dimethylacetamide

EC*/PEC = electrochemical/photo electrochemical

F.E. = Faradaic efficiency

F-T = Fischer-Tropsch

GDL = gas diffusion layer

HER = hydrogen evolution reaction

MEA = membrane electrode assembly

MFC = (ElectroCell's) Micro Flow Cell

MPL = microporous layer (component of the GDL)

M.W. = molecular weight

OER = oxygen evolution reaction

PCET = proton coupled electron transfer

PTFE/Teflon = polytetrafluoroethylene

RHE = Reversible Hydrogen Electrode

SCR = Space Charge Region

SHE = Standard Hydrogen Electrode

sPEEK = sulfonated poly(ether ether ketone)

U / V = potential / voltage

wt.% = weight percent

η = overpotential

*N.B.: ElectroCell also uses EC as their abbreviation and logo. In this report ElectroCell will not be abbreviated to avoid confusion with the term electrochemical.

1. Introduction: The Future of Energy

While moving towards a more renewable future, further emphasis is being put on the continuously rising CO_2 concentration in the atmosphere, which recently went over 400 ppm [1]. Although the exact responses of our ecosystem to this increasing concentration is not clear, it is likely to be the cause of global warming and the recent surge in extreme weather events across the globe [2]. There have been multiple international attempts to reduce emissions through the Kyoto protocol [3] and the Paris Agreement [4], or by capturing CO_2 before it enters the atmosphere by means of carbon capture (utilization) and storage (CC(U)S) [5]. None of these or otherwise known methods have clearly proven to be an economically feasible way to reverse or even stabilize the CO_2 accumulation.

Another factor is the continuously increasing energy consumption per capita combined with the increasing world population. According to the World Energy Council (WEC) [6] the best-case scenario states that by 2050 the population will increase by 25% (8.7 billion), while the energy demand will rise by roughly 123% (47.9 billion MWh), due to greatly increased electricity usage and the electrification of rural areas. However, adding further clean electricity sources is not a means to an end alone, resulting in further problems that need to be addressed.

Although the rapidly growing renewable energy sector of solar and wind can help compensate for the increasing energy demand, it does not balance out two other important factors. The first factor to consider is the time-of-use energy disparity between consumption and production of renewable energy on both daily and seasonal timescales. For day-night cycles it is likely that batteries can overcome the temporary shortage by storing excess daytime energy. However, batteries leak energy slowly and for winter times it might be more attractive to store this energy in a more stable synthetic fuel. The second factor is our current reliance on a great deal of carbon containing products that cannot be supplied by clean energy. A great variety of daily products consist of energy dense carbon-carbon (C-C) bond materials and these products are mainly retrieved from heavy oil fractions and other fossil fuels. Even though modest attempts are made to reduce the amount of fossil-based products - for instance shops that exchange plastic bags for paper ones - this hardly scratches the surface of the enormous oil-industry. Besides, most carbon-based products have become part of our daily lives and cannot simply be interchanged with other materials. In a fully sustainable future it is mandatory that we become independent of fossil fuels, motivating the need for a renewable method of producing energy dense C-C bonds.

A potentially attractive way to deal with the CO_2 problem, an abundance of intermittent electricity and the need for renewable C-C bonds, is through electrochemistry. It is possible to electrochemically reduce CO_2 into CO and/or hydrocarbons that can function as intermediate building blocks or directly as synthetic fuels. Subsequently, syngas (a mixture of CO and H_2 mixture) can be used in Fischer-Tropsch synthesis [7] to produce hydrocarbons. This already implies two possible pathways for renewable C-C bond formation. With these possibilities in mind, the goal of most electrochemical research has been to minimize the potential losses occurring thought the system in order to increase the energy efficiency of the studied reaction.

The electrochemical reduction of CO_2 is often combined with an oxygen evolution counter reaction and can be seen as a reversed combustion reaction in which electrical energy is put back into CO_2 to reform into more valuable carbon containing molecules with oxygen as a side product. The oxygen evolution reaction in specific requires a relatively small energy input, but in practice this value lies much higher due to inherent resistances and poor catalysts. One possible means to reduce the cost of this reaction is by implementing a bipolar membrane, which allows the use of two separated reaction media, which can then be optimized for both catalysts.

Aside from the efficiency of the reaction, another barrier to implementation of CO_2 reduction technologies is the low current density obtainable in a typical aqueous reactor. Due to the low solubility of CO_2 in water along with poor diffusion characteristics near the catalyst surface, CO_2 molecules cannot reach the active surface fast enough, thus the maximum reaction rate of CO_2 molecules is limited. As a result, current densities for the reduction of CO_2 have been stagnating around 30-40 mA/cm^2 [8] for liquid phase reactions. A recent technoeconomic analysis by Kenis et al. indicates that a minimum current density of 100 mA/cm^2 is required to convert enough CO_2 to CO and make the reaction economically attractive [9].

An interesting method for circumventing the liquid CO_2 limitations is by making use of a membrane electrode assembly (MEA). This setup allows for the use of gaseous CO_2 by combining a gas diffusion layer with a liquid conducting membrane and an active catalyst layer in-between, greatly shortening the diffusion pathway of CO_2. After the reaction, dissolved products such as CO, H_2 and short hydrocarbons can diffuse back into the gas phase where they can be separated in a post processing step. Although the mechanisms behind the use of a MEA are much more convoluted than a traditional setup, research has proven that utilizing such a setup is a successful method to increase current density by roughly a tenfold [10-12]. Nevertheless, the field of gas-based electrochemistry is still in its infancy and a great deal of additional research efforts are required to determine the most effective MEA type and configuration.

Previous CO_2 reduction research was mainly focussed on finding the best catalyst material and electrolyte conditions in mechanistic studies in order to increase selectivity and activity. The use of MEA's show a severe increase in kinetics and advanced transport limitations, which changes the relevance of many of the involved factors, therefore also changing the direction of future research. **In this thesis different MEA configurations will be built, characterized and compared in order to shine a light on what conditions are optimal for achieving higher current densities for the electrochemical reduction of CO_2.** The scope of the research will be answering the following research questions:

- Which of the tested MEA setups provides the highest current at a fixed cell potential?
- What are the effects of altering different components in an MEA setup in terms of reaction selectivity and stability?
- How does the bipolar membrane impact the current density?

During this research membranes, electrolytes and gas diffusion layers are altered to compare the different components and monitor the change of characteristic parameters. The current density and selectivity is further measured as a function of cell potential. Although a great deal of research has been done on CO_2 reduction catalyst materials in aqueous setups with standardized testing methods [13], the field of membrane electrode assemblies has no clear benchmarking method yet. This makes current MEA research arbitrary from laboratory to laboratory. Since the MECS and TP groups at the TU Delft have little to no experience with MEA based systems for the CO_2RR, the overarching goal of this research is to obtain a functional system that can act as a benchmarking method and platform for future gas-diffusion based CO_2 reduction research.

This report is set up as follows: The theory and parameters of CO_2 reduction and MEA components will be discussed in Chapter 2. In Chapter 3 the methodology of the performed experiments as well as the characteristics of the used electrochemical cell will be explained. Chapter 4 displays the results of the experiments while Chapter 5 discusses the found results and reflects them against relevant literature. The discussion section will also be used to reflect and determine how to proceed with CO_2 reduction research at a systems level in general and, more specifically, within the MECS research group.

2. Theory: Reactions, flowcell and MEA

During this research the conversion of CO_2 will be studied. Therefore, a basic understanding of the electrochemical principles behind the occurring reactions will be discussed first. The considered reactions are the CO_2 reduction reaction (CO_2RR) and the oxygen evolution reaction (OER). Both reactions have been studied and described thoroughly in the past in terms of mechanism and working principles and are explained according to literature in section 2.1. The CO_2RR will be discussed thoroughly, whereas the OER is more of a complementary reaction and will thus be described in lesser detail. Secondly, despite the thermodynamics of the two half reactions remaining the same in any setup, the used flowcell system is quite different from the conventionally used H-cell. Section 2.2 will discuss both configurations and system parameters in detail. Finally, the function and working principles of each component in the membrane electrode assembly will be explained in section 2.3. Special attention will be given to describing the mechanisms of different ion exchange membranes.

2.1 Electrochemical half reactions

As with every electrochemical reaction, the driving force behind the reaction is the potential-driven transfer of electrons from one molecule to another in order to create a system that is in thermodynamic equilibrium. Therefore, this reaction requires an oxidizing agent, which gives up electrons at the anode, and a reducing agent, which takes up electrons at the cathode. Naturally, these two reactions are in balance to maintain electroneutrality. However, a wide variety of ionic intermediates may exist momentarily, complicating the reaction. After going over the CO_2 reduction, the competitive H_2 evolution and O_2 oxidation half reactions, a separate section is dedicated to the concepts of total cell potential and overpotential.

2.1.1 CO_2 reduction

Although this research focusses on the conversion of CO_2 to CO at the cathode, CO_2 can be reduced to a variety of products depending on catalyst material, applied potential, morphology and reactant concentrations. The catalyst material determines the binding strength of all involved species (reactants, intermediates and products) and mainly controls the selectivity of the reaction. It is possible to tune the reaction towards high selectivity of one product or towards a wide variety of molecules. Examples of high CO selective materials in the CO_2 reduction reaction(CO_2RR) are catalysts such as oxide-derived silver (OD-Ag) [14] and gold nanoparticles (Au-NP) [15] with a selectivity of respectively 80% and 90% due to their strong binding to CO_2 and weak binding to CO [16], thus releasing CO as it is produced. Oppositely, copper gives a wide array of products. Jaramillo et al. [17] showed that at least 16 different carbon containing species were formed from CO_2 on metallic copper (Cu) due to the relatively strong binding to CO, which allowed CO to be an intermediate for further products. Carbon containing products on Cu included alcohols, aldehydes, carboxylic acids and ketones, albeit in small quantities. By changing morphology, mixing catalytic elements and changing reaction conditions it is possible to tune the selectivity of products, as shown by Ma [18]. However promising it may sound, the field of CO_2 reduction research relies on mechanistic understanding of the CO_2 reduction reaction, for which even the most elementary steps for the simple conversion (CO_2 to CO) are still under heavy debate [19]. Koper et al. [20] has used online mass spectrometry to monitor the quantity of intermediates and products during the CO_2RR on Cu in order to figure out mechanisms and deduce rate determining steps. Accordingly, it was found that the first electron uptake to adsorb CO_2 ($CO_2(g) + e^- \rightarrow COO^-_{ads}$) is rate limiting, unless more complex products (C_{2+}) are formed. It was also shown that from a mechanistic point of view it is likely that C_1 products are formed from adsorbed CO at moderate overpotentials (CH_4 @ -0.8 V versus RHE) and that C_2 products are formed from the same CO intermediate, but as a dimer at lower overpotentials (C_2H_4 @ -0.5 V versus RHE). Their proposed reaction pathway on Cu is depicted in fig. 1.

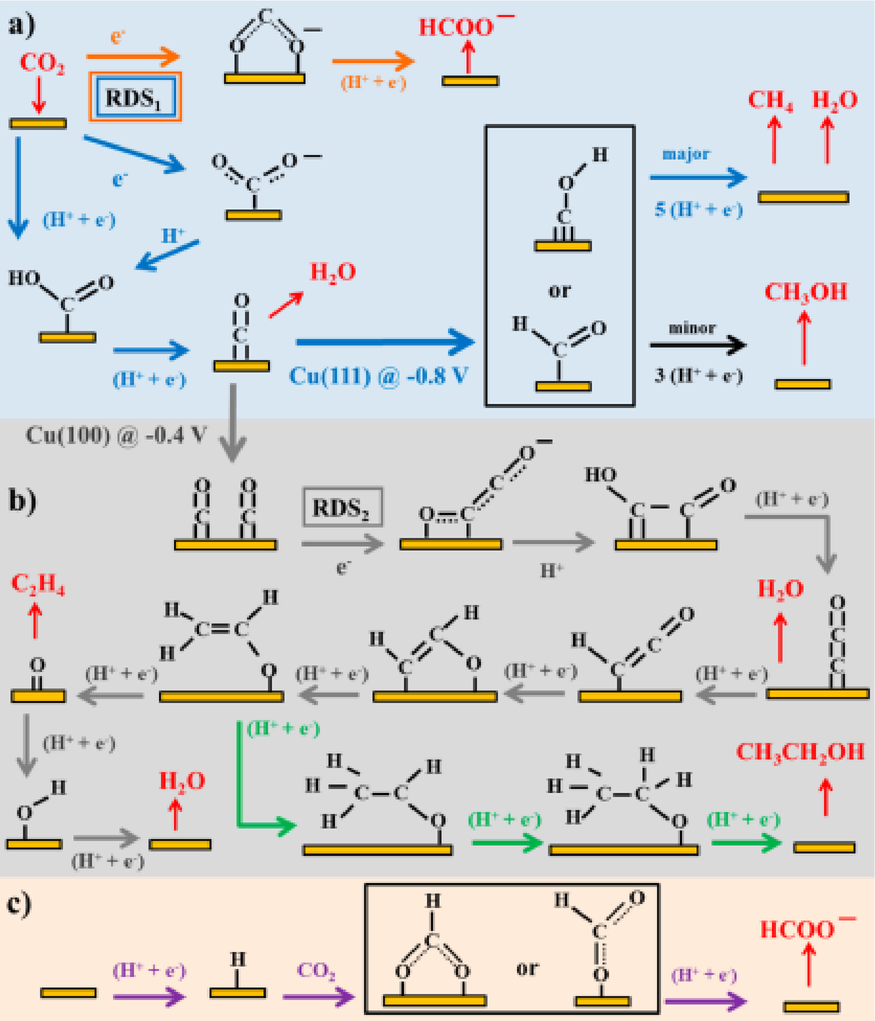

Figure 1. Proposed reaction pathways for the electrocatalytic reduction of CO_2 on Cu. Differently coloured arrows are used for different products. In this proposed scheme there are two rate determining steps (RDS). RDS_1 is the initial uptake of an electron by CO_2 in order to absorb to the surface. The initial blue and orange arrows depict a variability in possible mechanisms. RDS_2 is the dimerization of two nearby adsorbed CO molecules. This step requires strongly bound CO and is therefore highly dependent on catalyst material and overpotential. [20]

Despite the interesting mechanisms behind CO_2 reduction on Cu, the desired product in this project is CO, the 'simplest' product of CO_2 reduction. In respect to fig. 1 the formation of CO is complete after the formation of the adsorbed '(metal)=C=O' intermediate. As mentioned before, Cu binds CO strongly, thus it only allows a fraction of the adsorbed CO to be released from the metal surface. Metallic surfaces such as Ag, Au and Zn follow the same pathway, but almost exclusively produce CO due to their much weaker binding energy to this specific intermediate. It is not certain whether the conversion of $CO_2(g)$ to $CO(g)$ consists of three or four elementary reaction steps. This has to do with whether the first intermediate, COOH*, is formed by a proton-coupled electron transfer (PCET: H^+ and e^- react simultaneously) or by two separate steps [21]. The pathway for the PCET and the pathway for separate electron and proton transfer are shown in fig. 2. Species with an asterisk (*) indicate adsorption to the metal catalyst. A recent study on the pathways for CO_2 reduction on a Ag catalyst [22] has shown that both primary elementary pathways may occur, depending on the applied potential. After the elementary step(s) of producing the $COOH^*$ intermediate (1,1a+b) the subsequent steps for producing CO are equivalent for both pathways (2+3).

$$PCET\ Pathway$$

$$1. CO_2(aq) + {}^* + H^+(aq) + e^-$$

$$Electron\ then\ Proton\ Pathway$$

$$1a.\ CO_2(aq) + {}^* + e^- \rightarrow COO^{-*}$$

$$1b.\ COO^{-*} + H^+(aq) \rightarrow COOH^*$$

$$2. COOH^* + H^+(aq) + e^- \rightarrow\ CO^* + H_2O(l)$$

$$\underline{3. CO^* \rightarrow CO(aq) + {}^* \qquad\qquad\qquad\qquad} +$$

$$Total: CO_2(aq) + 2H^+(aq) + 2e^- \rightarrow CO(aq) +\ H_2O$$

*Figure 2 Reduction pathways for CO_2 to CO conversion. * represents an active surface site at the cathode. A species followed by * indicates an absorbed species at the catalyst surface. Both the PCET and 2-step pathways have $COOH^*$ and CO^* intermediates.*

Although it seems like this reaction would require an acidic environment (= a high proton concentration) it has been shown that CO_2 reduction can also operate in alkaline media. During operation, such a system can obtain its protons from nearby H_2O molecules directly, thus producing OH^-. So, during reaction in an acidic medium protons will be consumed and during reaction in a basic medium hydroxyls will be produced. Kinetically speaking, it is favourable in terms of activity to operate in low pH, since this allows for either easier proton access or easier disposal of hydroxyls. This, however, greatly promotes hydrogen evolution, which is discussed more in the following section. Regardless of which starting medium is used, in both instances the local pH near the cathode surface increases over time.

The pH of solution has implications on product selectivity as well. Whenever pH increases the availability of protons decreases and therefore PCET is less likely to occur. Consequentially, in an alkaline environment products from separate electron transfers, such as ethylene (C_2H_4) are promoted [23]. Although it is not likely such products will be formed on a CO_2-to-CO selective catalyst, it is important to understand how possible undesired products may be influenced by operating in a mostly unexplored alkaline environment. *(Another factor that is influenced by pH is the concentrations of inorganic carbon species, which can be CO_2, HCO_3^- and CO_3^{2-}.)*

2.1.2 H_2 evolution

An alternative reduction reaction that can occur at the cathode is the hydrogen evolution reaction (HER). The HER only uses protons and electrons to form hydrogen ($2H^+ + 2e^- \rightarrow\ H_2$). Since the 2 electrons and protons cannot just all find their way to one another in solution, this reaction requires a conductive catalyst where at least one proton can be stabilized and free access for electrons is available. In comparison to the CO_2RR, which utilizes a variety of intermediates that also need to be stabilized, the HER is a much more straightforward reaction. In the pathway for CO_2 reduction (fig. 1-2) it was shown that many of the elementary steps require protons as well. Both the CO_2RR and HER compete for these surface adsorbed protons and are therefore considered to be competitive reactions. In section 2.1.4 it will be discussed that the HER requires electrons with a slightly lower potential in respect to the CO_2RR. This makes selecting a catalyst for a selective CO_2RR all the more difficult.

2.1.3 O_2 evolution

Whereas the goal of this research is CO_2 conversion, a counterreaction is required to provide the cathodic reaction with electrons. The most straightforward way to provide these electrons is by performing the oxygen evolution reaction (OER) at the anode. This reaction converts H_2O molecules, which are always available in abundance, into oxygen, protons and electrons. The pathway for this half reaction is the same as for the OER occurring during water-splitting ($2H_2O \rightarrow 2H_2 + O_2$) and is depicted in fig. 3. [24]

$$Oxygen\ Evolution\ Pathway$$

$$1. H_2O(l) + \ ^* \rightarrow OH^* + H^+(aq) + e^-$$

$$2. OH^* \rightarrow O^* + H^+ + e^-$$

$$3. H_2O(l) + O^* \rightarrow HOO^* + H^+ + e^-$$

$$\underline{4. HOO^* \rightarrow O_2(g) + H^+ + e^- + \ ^* \qquad +}$$

$$Total: 2H_2O(l) \rightarrow O_2(g) + 4H^+ + 4e^-$$

Figure 3 Oxidation pathway for water to oxygen. O^*, OH^* and HOO^* are very unstable intermediates, leading to a high required potential to perform this reaction

The main problem with this half reaction is that due to the stability of the H_2O molecule and the pathway along unstable intermediates (OH^*, O^*, HOO^*) a high potential is required to get oxygen evolution going. Since this half reaction provides 4 protons and electrons and the CO_2RR uses only 2 protons and electrons per CO_2 molecule, double the amount of CO_2 is reduced per produced O_2. It has been found that the OER half reaction, operates with the smallest losses at a high pH environment. This does however put strain on the choice of catalyst, as it needs to be stable around the pH 14 region. Some of the used catalysts, that can operate the OER stably in strongly alkaline solutions with minor excess losses, are iridium oxide (IrO_x) and nickel iron oxide ($NiFeO_x$). The next section will elaborate further on potential and losses.

2.1.4 Cell potential

One of the most important parameters in electrochemical systems, due to its implications on the technoeconomic feasibility, is the applied cell potential. This value describes the relative electrical energy each electron can *potentially* exert on an atom or molecule. An applied potential in an electrochemical setup is required for multiple reasons. Besides driving a reaction into a n otherwise thermodynamically unfavourable position, the applied potential is also required to create and overcome intermediates such as adsorbed species (H^*, $COOH^*$) and to surpass several resistances in the system.

When discussing potentials in electrochemistry, the standard hydrogen electrode (SHE) can be used as a standard reference. The SHE has a defined standard electrode potential (E_0) of 0 V at 1 bar, 298 K and 1M H^+ (pH 0) for the previously described HER that serves as a reference. Since the HER requires protons it performs worse as the proton concentration decreases, thus giving it a pH dependence. This dependence comes from the Nernst equation[1a] [25], where R is the ideal gas constant, T is the temperature, z is the amount of electrons for the reaction, F is Faraday's constant and Q is the reaction quotient. When filled in for the HER (z = 2, ln(Q) = -2*ln [H^+] = -2*2.303*log [H^+]) this causes the SHE to shift its potential according to equation [1c]:

$$E = E_0 + \frac{RT}{zF} * \ln(Q) \qquad [1a]$$

$$E = E_0 - 2 * 2.303 * \frac{8.314*298}{2*96485} * \log[H^+] \qquad [1b]$$

$$E = E_0 - 0.0592V * pH \qquad [1c]$$

However, a more practically used reference electrode that is preferred over the SHE is the reversible hydrogen electrode (RHE). The reason for this is that the RHE takes pH effects directly into account according to the Nernst equation and therefore making it pH independent.

When equation [1] is put to use it makes sense to use the RHE scale over the SHE. For instance, the HER reaction in an acidic medium of pH 0 is defined as 0 V vs SHE as well as vs RHE. Since the reaction consumes protons it is logical that a lower proton gradient, thus a higher pH, has more difficulty in performing this reaction. When the same reaction is performed in a pH 14 solution the SHE will therefore display -0.829 V (= 0 – 0.0592*14 V), since the potential value is dependent of pH. The RHE potential for the HER will however incorporate the pH in its potential, resulting in a potential that is still 0 V. Although the relative potential between any two reactions will still be correct for both the SHE and the RHE in a homogeneous solution of any given pH, the SHE does not communicate the relative potential between the two half reactions properly when two heterogeneous compartments with different pH are present. To demonstrate this the potential of the OER is first explained.

The required potential for the adsorption and conversion of species is specific for each reaction. In this project three reactions are of importance: At the anode only the OER occurs as was described in section 2.1.2. The conversion of the stable H_2O molecule to the much more reactive O_2 molecule goes against the natural balance that would be present when no potential was applied. In order to reverse this process the relative thermodynamic energy difference between the H_2O molecule and the O_2 molecule needs to be bridged. The energy difference of these molecules, thus the minimal required potential to perform the OER half reaction is 1.23 V vs RHE at pH 0. This is the greatest contribution to the total cell potential due to a larger overpotential that must be applied. Opposite to the HER at the cathode, this reaction produces protons and consumes hydroxyls and will therefore occur more easily in a high pH environment. As previously mentioned the RHE is chosen over the SHE as a reference. In Table 1, 3 different situations are used in combination with equation [1c] to clarify this case.

Table 1 HER and OER potentials vs RHE and SHE. E^0_{cell} is the potential difference between the two half reactions or the minimum theoretical cell potential required to operate the given conditions and is defined as $E^0_{cathode}$ - E^0_{anode} = E^0_{HER} - E^0_{OER}. The RHE potentials are independent of pH, whereas the SHE shows a significant drop in E^0_{cell} when performing the HER in pH 0 and the OER in pH 14.

Reaction	**RHE**	**SHE**
HER (pH 0)	0 V	0 V
OER (pH 0)	1.23 V	1.23 V
E^0_{cell} (ΔpH = 0)	**-1.23 V**	**-1.23 V**
HER (pH 14)	0 V	0 V – (14 * 0.0592) V = -0.829 V
OER (pH 14)	1.23 V	1.23 V – (14 * 0.0592) V = 0.401 V
E^0_{cell} (ΔpH = 0)	**-1.23 V**	**-1.23 V**
HER (pH 0)	0 V	0 V
OER (pH 14)	1.23 V	1.23 V – (14 * 0.0592) V = 0.401 V
E^0_{cell} (ΔpH = 14)	**-1.23 V**	**-0.401 V**

As shown in Table 1, the theoretical potential E^0_{cell} between the HER and OER is independent of pH in the case of using the RHE. The SHE takes the effect of pH into account using the Nernst equation and shows that in the HER(pH 0) – OER (pH 14) case needs a much lower potential to operate. This is given the fact that an acidic and a basic environment can coexist in one setup. The bipolar membrane allows for this situation, at its own cost, and will be further explained in the Membranes section (2.3.1).

At the cathode two reactions may occur. These reactions are the aforementioned CO_2RR and HER. The CO_2RR to CO is the desired reaction and occurs at – 0.11 V vs RHE. This reaction is combined with the OER (1.23 V vs RHE) at the anode and requires a theoretical potential of -1.34 V vs RHE. The HER is a competing reaction consuming both protons and electrons required for the CO_2RR. Although it is thermodynamically more favourable to combine the OER with the HER, the HER requires 2 protons near the reaction surface in order to produce H_2. This feature can be exploited to selectively reduce CO_2 instead of producing H_2 by using a material with a higher affinity towards adsorbing CO_2 than H^+. Each catalyst material has its own specific binding energy to reagents, intermediates and products and the goal of catalysis is to lower the energy barrier between reagent and product by making the intermediate step energetically more favourable, effectively reducing the required potential. As an example, the earlier mentioned catalysts Ag, Au and Cu have different binding energies to CO, resulting in different products at the same applied potential.

In fig. 4 the Gibbs free energy diagrams for the CO_2RR and for the HER on Ag and Au are displayed. The initial reagents and final products are desorbed from the metal surfaces and therefore have the same thermodynamic potential (-0.11 V for the CO_2RR, 0.00 V for the HER). Since both Au and Ag metals are similar in binding energies, most intermediate products have similar energy levels. Factors such as the orientation of reactive sites, however, have a significant effect on the observed binding energy of intermediates. This indicates that it might be favourable to nanostructure catalysts in order to increase the amount of corners and edges or expose various facets. When comparing the CO_2RR and the HER it is noticeable that the HER can overcome the intermediate energy barrier at a lower potential than the CRR. The result is that regardless of which metal surface is chosen as a catalyst for CO_2 reduction, the selectivity of CO and other carbon containing products can never reach 100% due to the consumption of electrons and adsorbed protons in the competing HER.

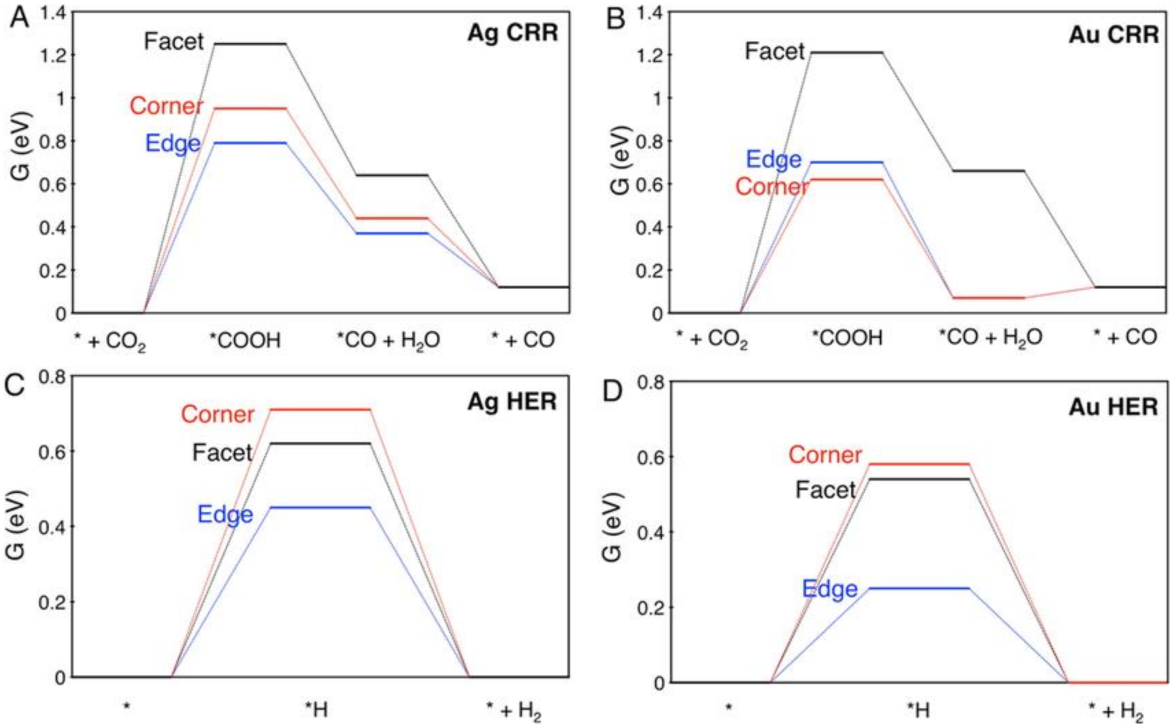

Figure 4 Gibbs free energy diagram for the CRR (=CO_2RR) and the HER on Ag and Au. As can be seen from these graphs, the thermodynamic minimum energy for the CO_2RR and HER is far less than the energy required to overcome their respective intermediates, $COOH^*$ and H^*. It is also shown that the facets of the active surface area can play a major role in reducing the energy required to overcome the intermediates. [26]

Besides the theoretical potential necessary to perform a set of half reactions there are many factors in the system that give rise to additional resistances. These resistances cause the theoretical potential to be insufficient to perform the given set of half reactions and imply the need for additional potential over the entire cell. The additional potential is also known as the *overpotential*, since it describes the amount of volts needed *over* the theoretical minimum. The symbol used for overpotential is the fifth letter of the Greek alphabet, η (èta), and includes all possible energy barriers. The overpotential and the theoretical potential together form the total voltage applied over the cell and can be referred to as the (total) cell potential (E_{cell}). The components of the total cell potential can be expanded as

$$E_{cell} = E_{rev} + \eta_{anode} + \eta_{cathode} + \eta_{membrane} + i * R_{ohmic} \qquad [2]$$

where E_{rev} is the reversible potential required to perform the reaction, η_{anode} and $\eta_{cathode}$ the overpotentials on respectively the anode and cathode, $\eta_{membrane}$ the potential required to overcome the membrane resistance and $i*R_{ohmic}$ the voltage losses due to the finite conductivity of the electrolyte. Moreover, η_{anode} and $\eta_{cathode}$ mainly consist of activation losses and mass transport limitations near the active surface. These overpotentials tend to grow with increased current density, since a higher current density requires faster conversion, which translates to increased surface activity and faster molecular transport. Some papers may refer to different names for overpotentials, such as $\eta_{mass\_transport}$ and $\eta_{activation}$ [27], instead of the parameters in equation [2], but all describe the same set of losses.

2.2 H-cell vs. Flowcell

In electrochemical research there are two types of cells available to test the activity, selectivity and stability of any catalyst. The conventional way to perform electroanalytic research is by utilizing a so-called H-cell. Some of the most renown researchers in the field of CO_2 reduction, such as Hori [28], Kanan [29-30] and Jaramillo [31] as well as many others [32-34], have been using the H-cell in the past to study a vast variety of metal heterogeneous (= surface) catalysts. Whereas the use of this setup has its benefits, more recent studies by the Kenis group [35] and others [36-37] have been leaning towards the use of an alternative system: the flowcell. A literature survey by Janaky et al. [38] was used to make the following graph, relating CO_2 research papers and citations to the amount of papers utilizing this alternative system (fig. 5)

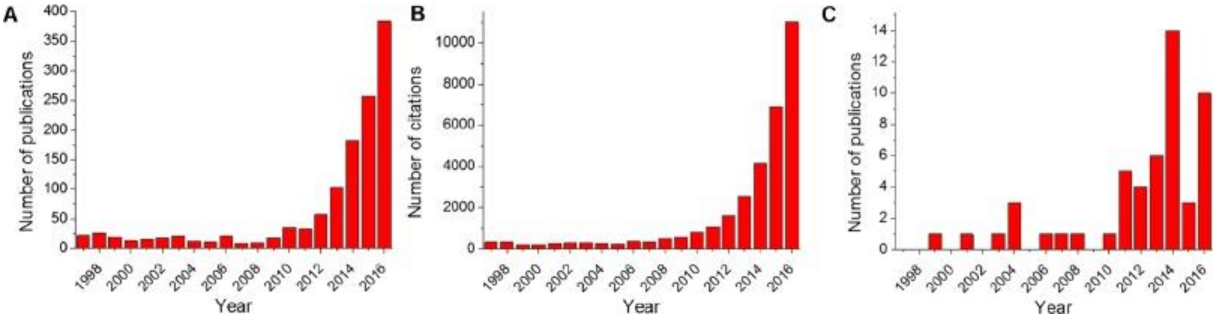

Figure 5 Literature survey on (P)EC CO_2 reduction papers. A: number of publications on CO_2 reduction. B: citations of papers in A. C: number of publications claiming to have utilized a flowcell setup.

In this section the H-cell and its features are explained first, then the flowcell and its benefits over the conventional system are discussed.

2.2.1 H-cell

Prior to the rapid development of heterogeneous catalysis for CO_2 reduction (≃pre-2010, see fig. 5) almost all exploratory work was performed in an H-cell configuration. Although there are no records for why exactly this is the case, it is most likely this setup is used due to its simplicity and the reproducibility of results. A single compartment electrochemical H-cell is shown in fig. 6 [39]. A double compartment cell, used for instance in membrane and/or double flat electrode experiments, is shown in fig. 7. The sturdy Teflon (PTFE) body of these cells has high corrosive resistance and combination with rubber O-rings make for a leakproof compartment. Multiple top inlets allow for the insertion of a wide variety of adjustments, such as reference electrodes, pH meters, gas inlets, electrolyte injection/sampling (for NMR/electrolyte characterisation) and gaseous product collection (for gas chromatography). Due to the formation of pH gradients in the electrolyte during operation it is desired to mix to avoid diffusional resistances in the electrolyte. This is possible in most H-cell setups by simply adding a magnetic stirrer and putting the cell on a magnetic hotplate, also allowing for heating where desired. The stirrer produces a turbulent flow throughout the compartment and helps with the release of gaseous products from the electrode surface. Since liquid flow is only regulated by the magnetic stirrer, and not with any mechanical pump exerting pressure, the amount of variables is kept to a minimum while most variables, such as mixing speed, temperature and pressure remain fairly constant.

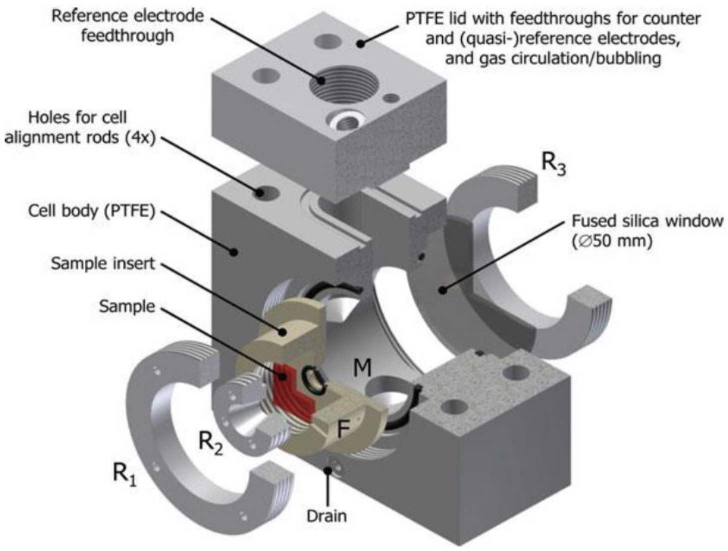

Figure 6 Technical schematic for a generic Teflon electrochemical H-cell. The rigid Teflon body enables the use of a wide variety of corrosive electrolytes (pH 0-14). The simple sample holder ($F+R_1+R_2$) allows for fast, leakproof assembly and the standardized electrode surface area offers reproducibility and comparison between samples. This specific setup had a glass window (within R_3) to perform photoelectrochemical experiments, or to observe gas evolution in situ. A magnetic stirrer can be added at M to mix the electrolyte.

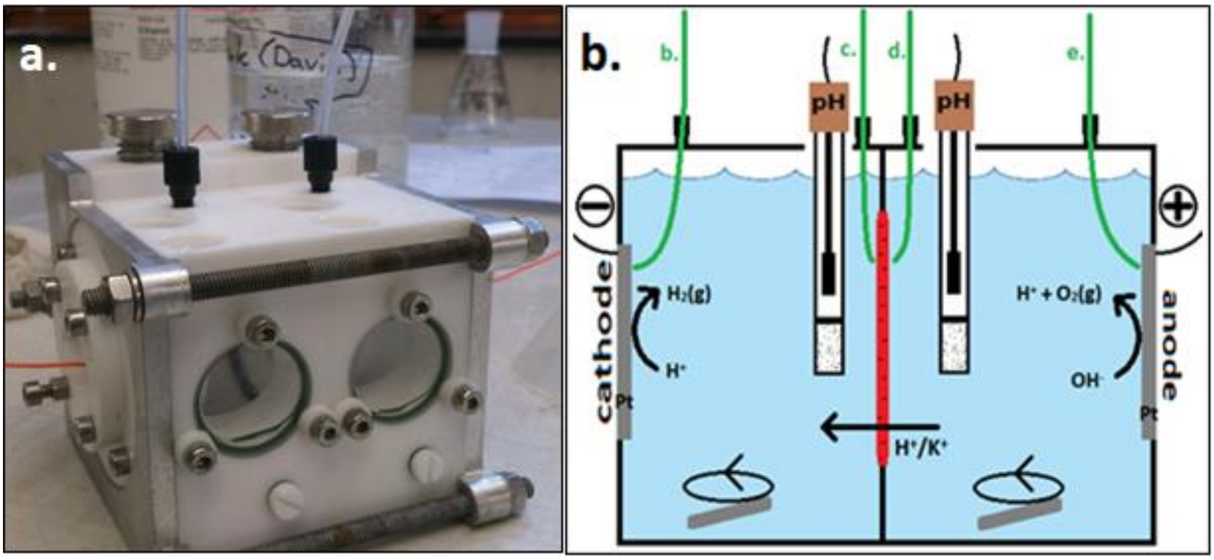

Figure 7 (a.) Double compartment electrochemical cell as used in a previous water splitting experiment. (b.) Schematic representation of the double compartment cell in a. The red layer represents a Nafion® membrane as was used. When a membrane is utilized a secondary magnetic stirrer is required to mix both compartments.

2.2.2 Flowcell

More recent electrochemical (CO_2) studies focussed on working with a flowcell/microfluidic cell. In theory this cell is quite similar to the conventional H-cell, with one major adjustment; flowing electrolyte. In previous work the main focus of research resided with finding the right catalyst for different products by e.g. measuring the effects of surface nanostructuring. Since the quality (or selectivity) of products was far more important than the quantity (or activity) of production, simple H-cell measurements sufficed. Nowadays CO_2 reduction research has progressed as such that selectivity is no longer the main issue, even though some mechanisms are still not fully understood. Because of this, producing higher current densities (>100mA/cm^2) and working at a system-level is gaining more interest in order to slowly advance towards commercialisation [40].

The specific setup and components used in this research will be described in detail in chapter 3.2, however, the overall flow cell setup is compared here to the H-cell system. Whereas an H-cell consists mainly of a single (or double) rigid Teflon compartment, a flowcell is usually built up from multiple thin layers (mm scale) with specific shapes in order to more controllably flow electrolyte throughout the system from an external reservoir. Despite the fact that the use of multiple layers makes for a system prone to leakage, it does offer greater flexibility in terms of customizing the system to suite different needs while keeping electrolyte usage to a minimum. The freedom in layering is almost endless since it enables the use of many individually specialized components of different materials, and the eventual necessity for cell stacking, which is outside of the scope of this research. An example of such a flowcell is given in a study performed by Mallouk et al. after the use of a BPM and gaseous CO_2 in a flowcell setup and is depicted in fig. 8. Since the aforementioned study has much in common with this research (both utilizing gaseous CO_2 in a flowcell setup with an MEA) its results will be used in the Discussion as a measure of comparison.

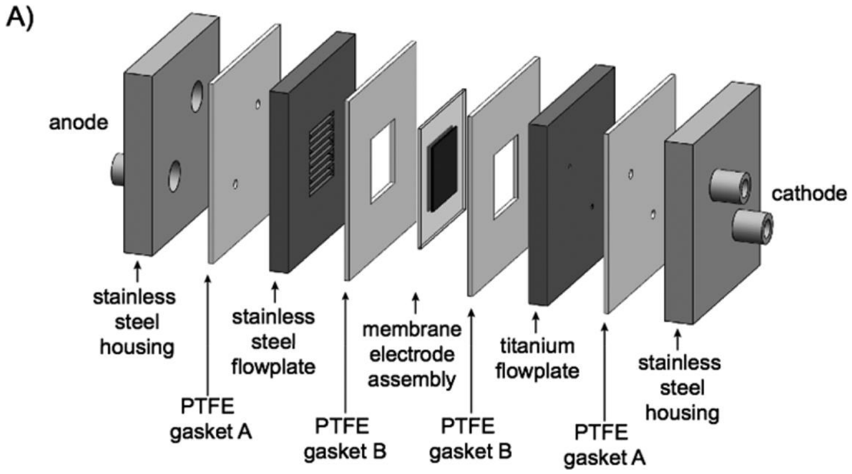

Figure 8. Expanded view of an MEA based flowcell as used in the research by Mallouk et al. [41]

Commonly used components in flowcells [42] are metal endplates and hardware (nuts/bolts) for mechanical compression, Teflon end frames for electrolyte in- and outlets, flow frames with turbulence mesh, gaskets to prevent leakage, direct electrode materials or sample holders, membranes and gas diffusion layers. The last-mentioned component, gas diffusion layers, is becoming increasingly prominent in the field of CO_2 reduction due to the low solubility of CO_2 in aqueous solutions [43]. This will be further elaborated on in section 2.3.3.

2.3 Membrane electrode assembly

The focal point of this research is understanding and producing an effective membrane electrode assembly (MEA). The MEA system can be used to combine liquid and gas phase reactions and limits product crossover while providing both half reactions with their respective required reagents. In theory the MEA only has two constituents; A membrane and an electrode catalyst closely packed together. However, the utilization of a MEA serves a specific purpose when combined with a gas diffusion layer. By combining a membrane, a catalyst layer and a hydrophobic gas diffusion layer (GDL) the system is capable of performing the CO_2RR in a liquid electrolyte while using a gaseous CO_2 feed stream. A slightly different configuration which integrates the electrode with the gas diffusion layer is also known as a gas diffusion electrode (GDE) in which the membrane is a separate component at some distance away. To avoid confusion: Since this research focusses on all three layers being packed closely together, without integrating the electrode within the GDL, the system will be referred to as a MEA with GDL (and not a membrane with GDE). Section 2.3.1 explains the use of different ion exchange membranes, with special attention paid to the use of bipolar membranes and their effect on the required potentials described in section 2.3.2. The use of gaseous CO_2 as a reagent and the functionality of the GDL are covered in section 2.3.3.

2.3.1 Ion exchange membranes

A membrane is typically placed between the anode and cathode electrolyte chambers to prevent products from crossing to the other side of the electrochemical cell and reverting back into the initial reagents. Membranes can further be implemented to even reduce the overpotentials needed to drive the reaction and increase the system efficiency. In theory there are three categories of ion exchange membranes available: cation exchange membranes (CEM), Anion exchange membranes (AEM) and bipolar membranes (BPM) which can be used depending on the choice of electrolytes and reaction conditions. In this research only the AEM and BPM will be used and their effects compared, however, since the BPM consists of both a CEM and an AEM it is helpful to understand all three types.

The CEM, known for DuPont's commonly used Nafion® membrane, is a membrane that allows the transport of cations such as H^+, but also of electrolyte co-ions (K^+, Na^+). This transport is facilitated by the composition of the CEM; A carbonfluor polymer backbone provides the CEM with sturdiness, preventing product crossover, while impregnated sulfonated side groups (SO_3^-) provide the membrane with a negatively charged character. The negatively charged SO_3^- groups are immobilised and allow for the attraction and transport of counterions (H^+/K^+) along the membrane while co-ions (OH^-/Cl^-) are being repelled from its surface.

The AEM operates similar to the CEM, but with a positively charged characteristic instead of a negative one. Whereas both CEM and AEM have a carbonfluor backbone to attribute strength, the functional SO_3^- group in a CEM is replaced by a quaternary amine (NR_4^+) side group in the AEM. Because of the positive nature of the immobilized NR_4^+ group the transport of anions such as OH^- and Cl^- is enabled while repelling cations. SO_3^- and NR_4^+ are chosen as functional groups since their electrostatic affinity towards counterions is present, but not strong enough to form stable molecular bonds, which would otherwise result in passivation of the functional group. The CEM and AEM molecular and schematic membrane structures are displayed in fig. 9. The molecular structures depicted in this figure are not standardized for all CEMs and AEMs. Important to note is that although both ion exchange layers are charged, neutrally charged molecules (H_2O) can be co-transported with ions across the membrane as well. Currently, a wide variety of reinforcement structures and functional groups are available to tune selectivity, pH stability, thickness and resistance as desired [44].

Another membrane, the bipolar membrane, has quite recently been picked up as a potentially beneficial element in electrochemical cells. This membrane consists of a combined cation- and anion exchange membrane effectively allowing the system to be separated into two separately functioning compartments, enabling the effective use of two individual electrolytes for the anode and cathode compartments. As a result, the anode and cathode can be optimized independent of each other without compromising the electrode environment. This is particularly valuable when the efficiencies of the individual half reactions are strongly tied to the reaction environment, which is the case for CO2RR, HER and OER.

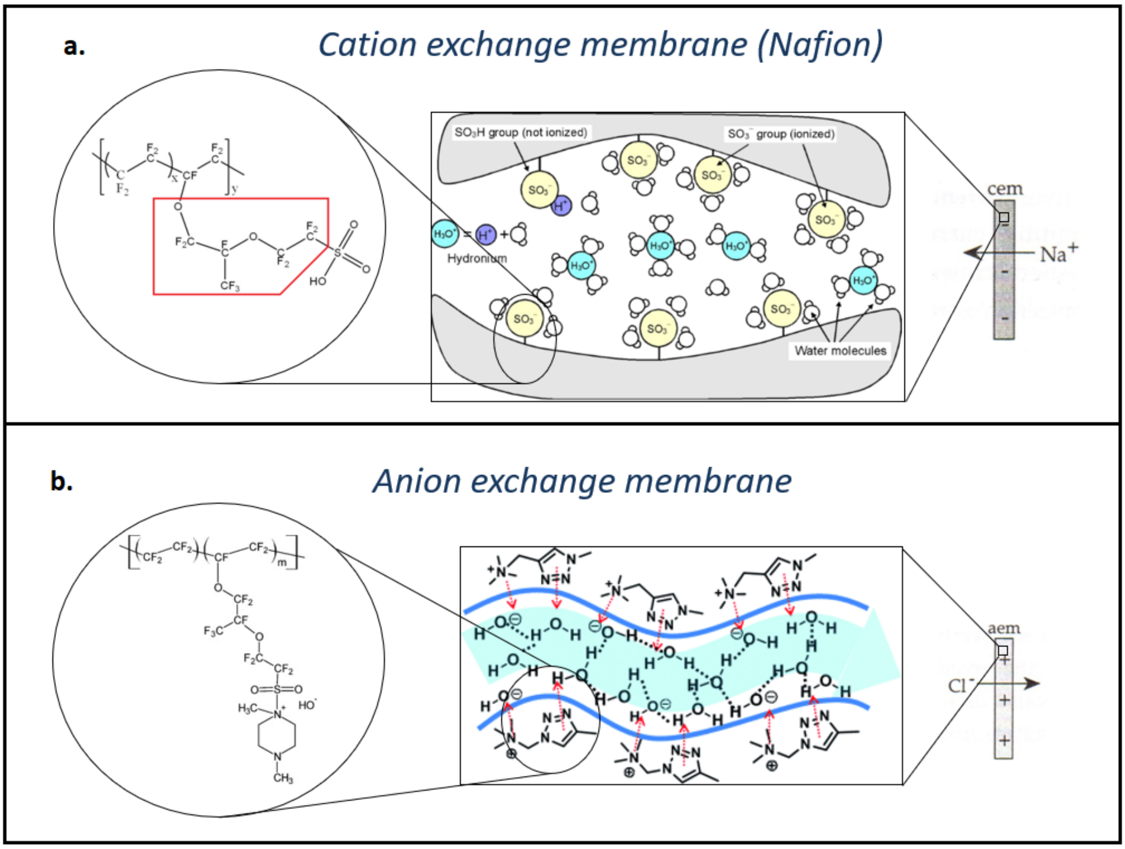

Figure 9 a: Molecular structure of a Nafion® CEM. The carbonfluor backbone provides strength and the SO_3^- *group enables cross membrane transport of protons/hydronium ions while repelling anions [45]. The red outlined area containing secondary chain carbonfluors is often targeted for modifications. b: Molecular structure of an AEM. The* NR_4^+ *group attracts and conducts hydroxyl groups without binding to them, while cations are repelled. [46].*

2.3.2 The bipolar membrane and its effect on potentials in the CO_2RR

The final membrane to discuss is the bipolar membrane (BPM) (not to mistaken with a bipolar plate). This specific type of membrane consists of three layers [47]. In order to produce a BPM a cation and anion exchange membrane are simply pressed together after pre-treatment with an alkaline solution containing metallic salt to improve adhesion [48]. Due to the close proximity of the positively charged AEM and the negatively charged CEM, the interface of the two layers neutralize one another, giving rise to an essential third layer: the space charge region (SCR). This interface layer is estimated to be ≈600–10,000Å thick [49]. In this area a strong electric field is present due to the nearby oppositely charged layers, parallel to a p-n junction as seen in photovoltaics, where the fixed charges in the AEM (NR_4^+) and CEM (SO_3^-) resemble positive and negative doping concentrations [50]. After formation of the BPM, remaining salt ions at the interface are expelled through the respective layers. Whereas the use of a single layer ion exchange membrane is to exchange ions, the goal of the BPM is to transport nothing across the membrane. Instead, within the SCR, water (H_2O) can be dissociated into hydroxyls (OH^-) and protons (H^+)/hydronium ions (H_3O^+), due to the presence of the electric field, at an incredibly fast pace (≈10^7 times faster than autonomous dissociation of water). Afterwards the OH^- and H^+ ions saturate the AEM and CEM, respectively, and are transported through. As mentioned previously, water is still able to move through the AEM and CEM, providing the reagent for this dissociation at the interface layer. The basic functionality of the BPM is shown schematically in fig. 10.

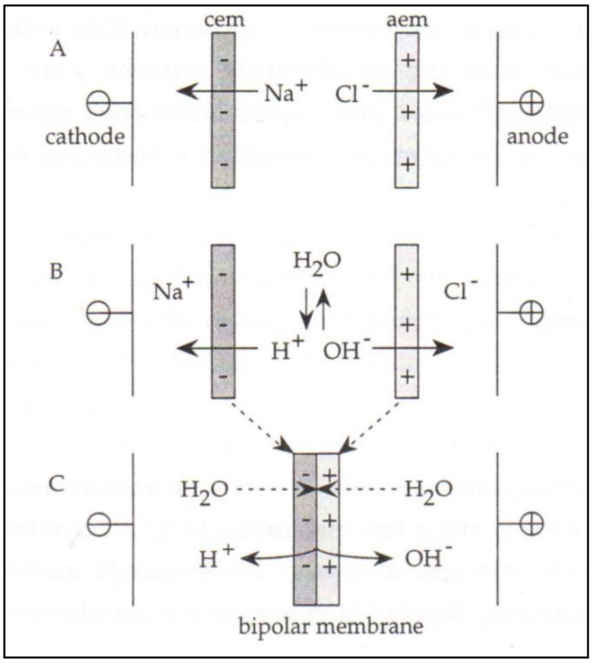

Figure 10 A: After putting the CEM and AEM close together solution ions (Na^+/Cl^-) are being expelled. B: Consequently, the only ions between the two mono-ionic membranes become hydroxyls and protons originating from the dissociation of water. C: Putting together the two ion exchange membranes results in a system similar to B., however, water molecules are now required to move from the bulk solutions to the BPM interface and after dissociation, hydroxyls and protons are transported back to the bulk according to their charge. [51]

Historically this membrane was first mentioned in 1956 by Frilette [52] for use in the biochemical industry. The BPM did, however, get picked up by the chemical industry in the '60s to perform electrodialysis. By utilizing the hydroxyl and proton formation, acids and bases could be regenerated from the massive amount of dilute wastewaters and salts produced as unwanted side products in chemical plants. [53-55]. After being picked up as an interesting membrane, much research has been done after the exact properties of the BPM.

In terms of potential, all ion exchange membranes have a specific characteristic, caused by the saturation of counter-ions within. The bipolar membrane takes this even further due to the presence of oppositely charged ions in the AEM and CEM. Fig. 11 shows the concentration and electrical potential profile for the BPM at thermodynamic equilibrium. The concentrations of fixed charge groups in the AEM (anion-exchange resin) and CEM (cation-exchange resin) are constant throughout the membrane, giving rise to the concentration gradients of mobile ions. Starting from the anolyte (left) and following the concentration of C_+^m (mobile cations): As the bulk approaches the positively charged AEM, the concentration of cations decreases, due to electric repulsion, down to the minimum concentration within the AEM. Although the system is designed to prevent ion crossover, the membranes are not perfectly selective, resulting in a minor cation concentration present throughout the anion exchange membrane. At the interface layer (=2λ) the polarity of the system switches rapidly, depleting the area of most mobile ions. When the CEM is approached, C_+^m increases significantly, up to a saturation concentration, equal to the concentration sum of fixed charge groups and mobile anions ($C_+^m = C_-^f + C_-^m$). Near the catholyte bulk diffusion causes the high cation concentration to lower towards the catholyte bulk concentration. For the mobile anions (C_-^m) a similar concentration profile can be found, but mirrored in the SCR. The result of these oppositely charged concentrations is visible in the potential gradient; The high anion concentration in the AEM causes a positive electrical potential difference to be present between the anolyte and the AEM (indicated by $\Delta U_{Don,1}$). Vice versa, the high

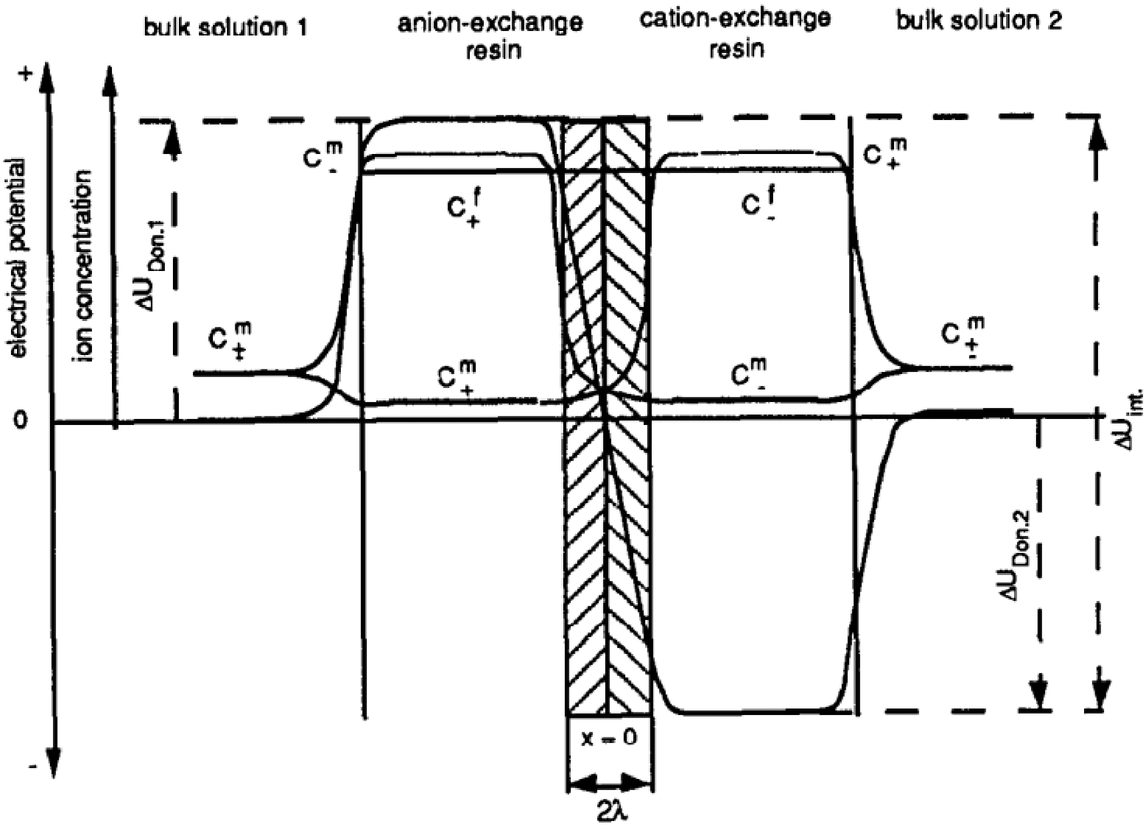

Figure 11 Concentration and electrical potential profiles for the bipolar membrane at thermodynamic equilibrium (no applied potential). The ion concentrations are labelled as such: C^m and C^f indicate the concentrations of mobile and fixed charges. C_+ and C_- indicate positive and negative charges. The relative electrical potential levels are indicated by $\Delta U_{Don,1}$, $\Delta U_{Don,2}$ and ΔU_{int}. 2λ represents the space charge region. [51]

cation concentration in the CEM causes a negative potential difference between the catholyte and the CEM ($\Delta U_{Don,2}$). At the interface layer these effects amplify one another, resulting in a strong potential gradient over a short distance (ΔU_{int}), which is defined as a strong electric field. The parameters $\Delta U_{Don,1}$ and $\Delta U_{Don,2}$ refer to the Donnan potential difference caused by the difference in internal and external (near membrane) ion concentrations and is shown in equation 3.

$$\Delta U_{Don}(V) = 2\frac{k \cdot T}{e} * ln\frac{c^f_\pm}{c^m_\pm} \qquad [3]$$

This equation looks very similar to the last term of the Nernst equation. The fixed charge groups cause an internal acidity of ≈pH 0 in the CEM and ≈pH 14 in the AEM [56] and the BPM potential is equivalent to $\Delta U_{BPM} = \Delta U_{int} - (\Delta U_{Don,1} + \Delta U_{Don,2})$, therefore the total potential over the BPM can be simplified via equation 4 to equation 5.

$$\Delta U_{BPM}(V) = 2\frac{k \cdot T}{e} * (\Delta pH_{AEM-CEM} - (\Delta pH_{AEM-anolyte} + \Delta pH_{catholyte-CEM})) \qquad [4]$$

$$\Delta U_{BPM}(V) = 0.0592 * \Delta pH_{anolyte-catholyte} \qquad [5]$$

where $\Delta pH_{anolyte-catholyte}$ is the difference between the anolyte and catholyte solutions near the surface of the AEM and CEM. Although it seems like this relation imposes a significant additional loss on the system (e.g. [pH catholyte] – [pH anolyte] = 0 - 14 → ΔU_{BPM} = 0.83 V), the fact of the matter is that the pH conditions themselves are beneficial for the half reactions occurring at the electrodes. This is explained through the Table 2, which compares a pH 0-0 to a pH 7-14 situation by using equation 5 for the membrane potential and the Nernst equation for the half reaction potentials.

Table 2 Potential comparison for the CO_2 reduction with a bipolar membrane in two different systems. The pH 0-0 case describes an acidic 1M H^+ environment in both catholyte and anolyte compartments. The pH 7-14 case compares a neutral catholyte with a basic 1M OH^- anolyte. For this table it is assumed overpotentials are negligible to clarify a proof of principle.

Location (Red/Ox)	**Reaction**	**pH 0-0**	**pH 7-14**
BPM	$H_2O \rightarrow OH^- + H^+$ (x4)	$\Delta U_{BPM} = \Delta U_{0,BPM}$ $= 0.00V$	$\Delta U_{BPM} = \Delta U_{0,BPM} + 0.059 * \Delta pH$ $= 0.00V + 0.059 * 7$ $= 0.413V$
Cathode (CO_2RR)	$CO_2 + 2H^+ + 2e^- \rightarrow CO + H_2O$ (x2)	$E_{Red} = E_{0,Red}$ $= -0.11V$	$E_{Red} = E_{0,Red} - 0.059 * pH_{cath}$ $= -0.11 - 0.059 * 7$ $= -0.523V$
Anode (OER)	$4OH^- \rightarrow O_2 + 2H_2O + 4e^-$ (x1)	$E_{Ox} = E_{0,Ox}$ $= 1.23V$	$E_{Ox} = E_{0,Ox} - 0.059 * pH_{an}$ $= 1.23V - 0.059 * 14$ $= 0.401V$
Total	$\mathbf{2CO_2 \rightarrow 2CO + O_2}$	$\boldsymbol{E_{tot}} = \Delta U_{BPM} - E_{Red} + E_{Ox}$ $= \mathbf{1.34V}$	$\boldsymbol{E_{tot}} = \Delta U_{BPM} - E_{Red} + E_{Ox}$ $= \mathbf{1.34V}$

In previous research current density was shown to be an important factor on the potential behaviour of the BPM [57]. At lower current densities the system works at practically no overpotential regardless of pH, thus allowing any combination of favourable environments to be chosen for the cathode and anode reactions according to Table 2. As a result, the bulk pH values of both electrolytes could be used to determine the overpotential over the membrane. However, at higher current densities, the ion transport from the CEM and AEM to both electrolytes becomes mass transport limited, resulting in a local pH equal to that of the membrane layers and different from the bulk. If these values are implemented in equation 5 it is found that for higher current densities the potential difference becomes 0.83 V, regardless of the bulk pH, as was experimentally proven. The current density dependence of the overpotential and local pH is schematically shown in fig. 12.

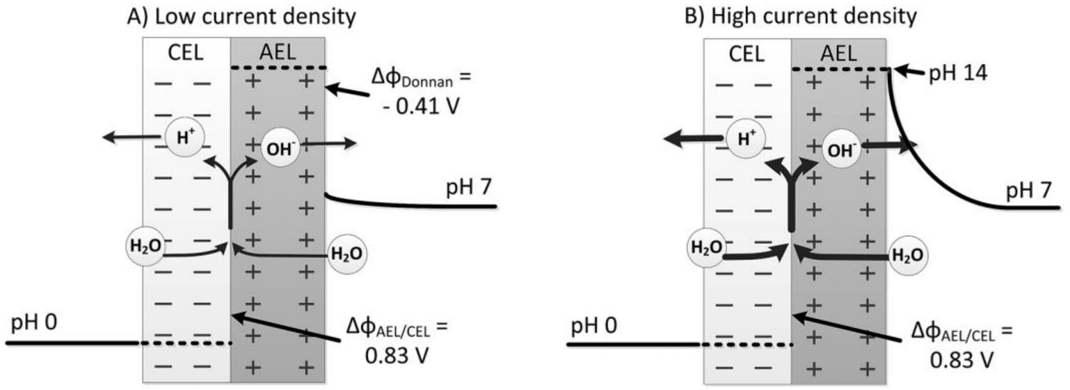

Figure 12 Current density dependence of overpotential over a bipolar membrane for a pH 0 catholyte and a pH 7 anolyte. A: at low current density the local pH difference between the AEL and the anolyte is 7 pH units, this indicated a favourable outflow of hydroxyls from the AEL to the bulk, thus lowering the membrane potential by 0.41 V. B: as current density is increased the local pH of the anolyte near the AEL becomes polarized, resulting in no favourable outflow of ions and a BPM overpotential equal to the potential over the interface layer (0.83V). [57]

2.3.3 Solubility of CO_2, gas diffusion layer and the MEA

The low solubility of CO_2 is one of the main limitations to upscaling current CO_2RR research. At standard temperature and pressure the solubility of CO_2 in water is ≈34mM, which translates to a maximum available current density of ≈30mA/cm^2 [58]. In practice, average current densities for liquid CO_2 reduction are found to be slightly lower at 10-20mA/cm^2. Although these current densities are high enough for doing mechanistic/selectivity studies, practical devices to store electricity in fuels, such as electrolysers that produce H_2, operate at current densities of 100-300mA/cm^2 in alkaline AEM conditions and reach even higher values (800-1600mA/cm^2) for acidic CEM electrolysers [59]. These numbers and related research show that CO_2 reduction can only become cost competitive if higher current densities at low overpotentials (150mA/cm^2 @ 1 V η_{cell}) are achieved [60]. This is impossible in liquid electrolytes, even when going to extreme conditions to increase CO_2 solubility significantly, e.g. sub-zero temperatures and >10bar pressures.

Fig. 5 shows the increase in the prevalence of flowcell setups reported in literature. In the same paper it was also mentioned that one of the reasons for this shift is the potential application of a gas diffusion layer (GDL) in order to increase the overall conversion of CO_2. The GDL allows for the use of gaseous reagents to be transported through, while reacting with liquid media on the other side. This functionality is enabled by its hydrophilic-hydrophobic structure. A GDL consists of a carbon bilayer structure; a thick macroporous carbonfiber based backing layer that provides mechanical properties, such as strength and compressibility, and a thin microporous carbon black based layer that prevents liquid crossover. To ensure the prevention of liquid crossover both layers have been treated with PTFE, a hydrophobic polymer. Common concentrations of PTFE in the macroporous and microporous layers are around 5% and 20%, respectively. In PEM fuel cell technology the GDL is a standard component, where some research even specialized on the optimization of the GDL in this system [61-62]. In fig. 13 a schematic representation of the GDL in combination with an applied catalyst layer (CL) and a membrane is displayed. This combination of GDL, CL and membrane is also referred to as a membrane electrode assembly (MEA), and has proven to be an effective method of increasing the current density of the CO_2RR.

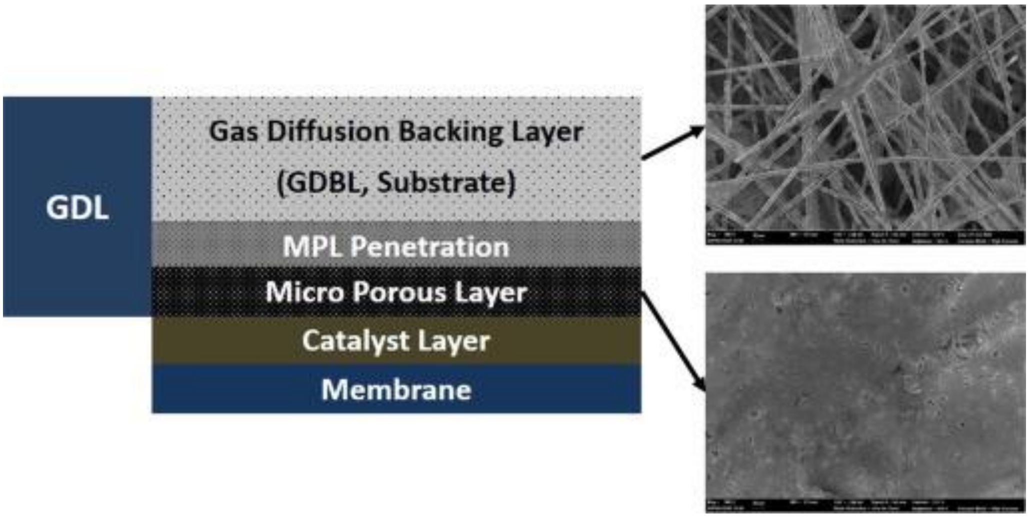

Figure 13 schematic representation of a membrane electrode assembly: a gas diffusion layer is combined with a catalyst layer (CL) and a membrane. The microporous layer is directed towards the catalyst layer, where liquid electrolyte is present. The macroporous layer provides strength and allows unhindered gas flow, relative to the microporous layer. The displayed MPL penetration area is a transition region constructed during production, where the carbon black based MPL covers the GBDL partially. [63]

The increase in current density is not only attributed to the use of a gaseous layer, but also to the application of the catalyst layer to the GDL. Due to the carbon based structure of the GDL its electric conductivity is sufficient enough to efficiently provide electrons to the CL. Since the CL needs to be slightly porous in order for membrane reagents (protons) and GDL reagents (CO_2) to interact, the use of a sprayed catalyst layer on top of the MPL is often used. This procedure of catalyst material interstitial to the GDL produces a so-called gas diffusion electrode (GDE). The active catalyst surface area in a GDE is increased while the quantitative amount of material used is reduced, due to the dispersion of catalyst particles on and in the MPL. The combination of utilizing gaseous CO_2 on a conductive backing area and a well dispersed catalyst results in an overall increase of current density, as shown in a survey by Kenis et al. where in multiple cases current densities over 100 mA/cm^2 were obtained [64]. Other research found even higher current densities could be achieved (200 mA/cm^2). Some of this research seemed genuine [65] however, other cases had issues, such as not displaying measurements, the application of toxic and unstable ionic liquids or the use of extreme overpotentials (V_{cell} = 5 V) [66].

3. Methodology

In the previous chapter a theoretical background and the current state of research was given. This chapter first discusses the experimental goals of the research (3.1). The specifications of the used electrochemical cell, as well as the setup and connections between all used components, will then be discussed (3.2). Afterwards, the preparation procedures for the MEAs (3.3) and electrolytes (3.4) are mentioned. This chapter closes by discussing the methods used to characterize the MEA through potentiostatic measurements, gas chromatography and SEM imaging (3.5).

3.1 Experimental plan

The primary goal of this research is to compare the activity, selectivity and stability of three different MEA systems in order to determine what components are beneficial and what type of system should be focussed on in future work. The activity and stability can be measured by means of chronoamperometry in which the quantity and time dependence of current at a stable potential are measured. The selectivity is determined using the Faradaic efficiency calculation for produced hydrogen and CO. In order to see the effect of component changes in the MEA composition, the amount of variables in each system is minimized by using the same type of electrodes, electrolyte, gas diffusion layers, assembly methods of the flowcell and assessment methods for each setup. In two setups the BPM will be tested and in one setup the AEM will be used. The AEM setup does not have a cation selective membrane, and will therefore operate at the pH of the bulk electrolyte solution. In this case the AEM is only used to prevent product crossover. For the BPM experiments, measurements are performed with and without a supporting cation ionomer solution. The cation ionomer solution is a liquid version of the CEM and is used to create a closer, more direct connection between the active cathode catalyst and the CEM layer of the BPM. Therefore, the only alterations made to the flowcell setups resides at the MEA component and can be described by the parameters in Table 3. As can be seen from Table 3 the only two interchanges made are the membrane type and the application of ionomer solution between the membrane and Ag-mesh.

Table 3 Different flowcell setups for comparison. Setup 1 consisting of a BPM – Ag-mesh – GDL will be used as the main reference for comparison of setups 2 and 3.

Setup no.	MEA name	Membrane type	Cathode catalyst	Gas diffusion layer
1	Bipolar membrane electrode assembly (**BPMEA**)	BPM	Ag-mesh 80	Sigracet 39BC
2	Anion exchange membrane electrode assembly (**AEMEA**)	AEM	Ag-mesh 80	Sigracet 39BC
3	ionomer coated bipolar membrane electrode assembly (**ionomer BPMEA**)	BPM + Cation ionomer	Ag-mesh 80	Sigracet 39BC

Further details and illustrations of the base setup are given in section 3.2, as well as a detailed description of the ElectroCell flowcell. In section 3.3 the MEA working principle and its component materials will be discussed, including the reasoning behind the use of different membranes and the ionomer solution. The stability and activity of the systems will be compared by performing cyclic voltammetry and chronoamperometry measured with a potentiostat, while the selectivity will be measured with gas chromatography.

3.2 Electrochemical cell configuration

For all experiments performed in this research the Micro Flow Cell® by ElectroCell is used. The Micro Flow Cell® (MFC) is the smallest (10 cm^2 electrode area) commercial electrochemical cell in a line of high quality electrochemical systems that can be modified to fit a desired purpose. Fig. 14 shows the exterior look of the MFC used in this research which has been customized for gaseous CO_2 utilisation.

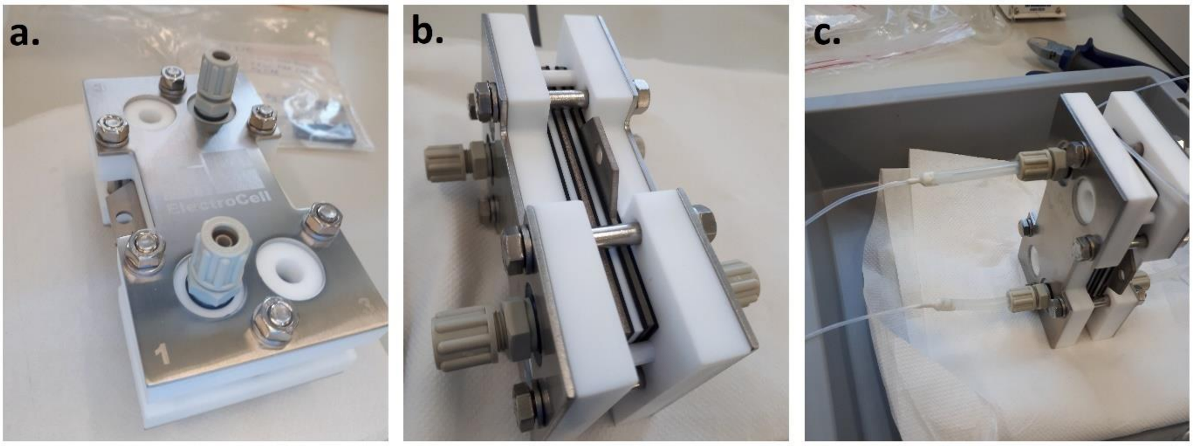

Figure 14 Exterior view of ElectroCell's Micro Flow Cell: a. Front view of the liquid anode compartment (indicated by 1 and 3 on the stainless steel endplate). The cathode, which is indicated similarly by 2 and 4 on the opposite side, is designed as a gas in- and outlet. Six size 10 bolts and nuts are used to compress system to avoid leakage. b. Side view: The bolts and nuts go through the Teflon end frames yet around the layered structure of the interior. The anode and cathode consist of Ni(s) blocks that stick out at the centre in order to connect them via an external circuit. c. During operation the MFC is placed in an upright position. The bottom tube connections are inlets and the top 2 connections are outlets.

As can be seen from fig. 14, the cell itself is a robust block made from polytetrafluoroethylene (PTFE) providing mechanical strength. On the stainless steel endplates numbers 1 to 4 are displayed, indicating different chambers where fluids enter and exit the cell. For this cell only chambers 1 and 2 are in operation for liquid and gas respectively. The internal layers, shown in 14b, alternate between rubber gaskets and electrodes/PTFE flow frames. Technical Data of the MFC (and other devices by ElectroCell) can be found in Appendix A. Although the technical data describes many aspects of the system, it does not give clear indications of the parameters of the used cell, due to customisation of the internal layers. The complex interior of the cell is illustrated in an expanded view of the cell (see fig. 16, N.B. stainless steel endplates, bolts and a polyvinylidene fluoride mesh (PVDF, a non-reactive thermoplastic fluoropolymer) are left out for clarity).

Going through fig. 16 from the cathode side (A) to anode side (B): The PTFE end frame (A) is used as the inlet for gaseous CO_2. The first rubber gasket transports gas through channel 2 while channel 4 is sealed and unused for these experiments. The centre cut-out (10 cm^2) is due to the standardized production of gaskets. The PTFE flow frame with internal PVDF turbulence mesh (fig. 15) is used to distribute gas through the cell and limits the formation of 'dead zones' (stagnant regions during flow). A second gasket, this time without holes, is used to conduct gaseous reactants and products between the PTFE flow frame and the cathode/GDE. The cathode/GDE is where the MEA resides and the CO_2RR takes place on a 10 cm^2 area, where the CO_2 gas phase transitions into a liquid KOH electrolyte. This compartment will be zoomed in upon and discussed in detail in section 3.3.

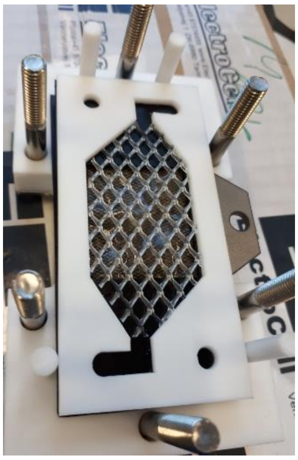

Figure 15. PVDF turbulence mesh is applied to annul dead zones.

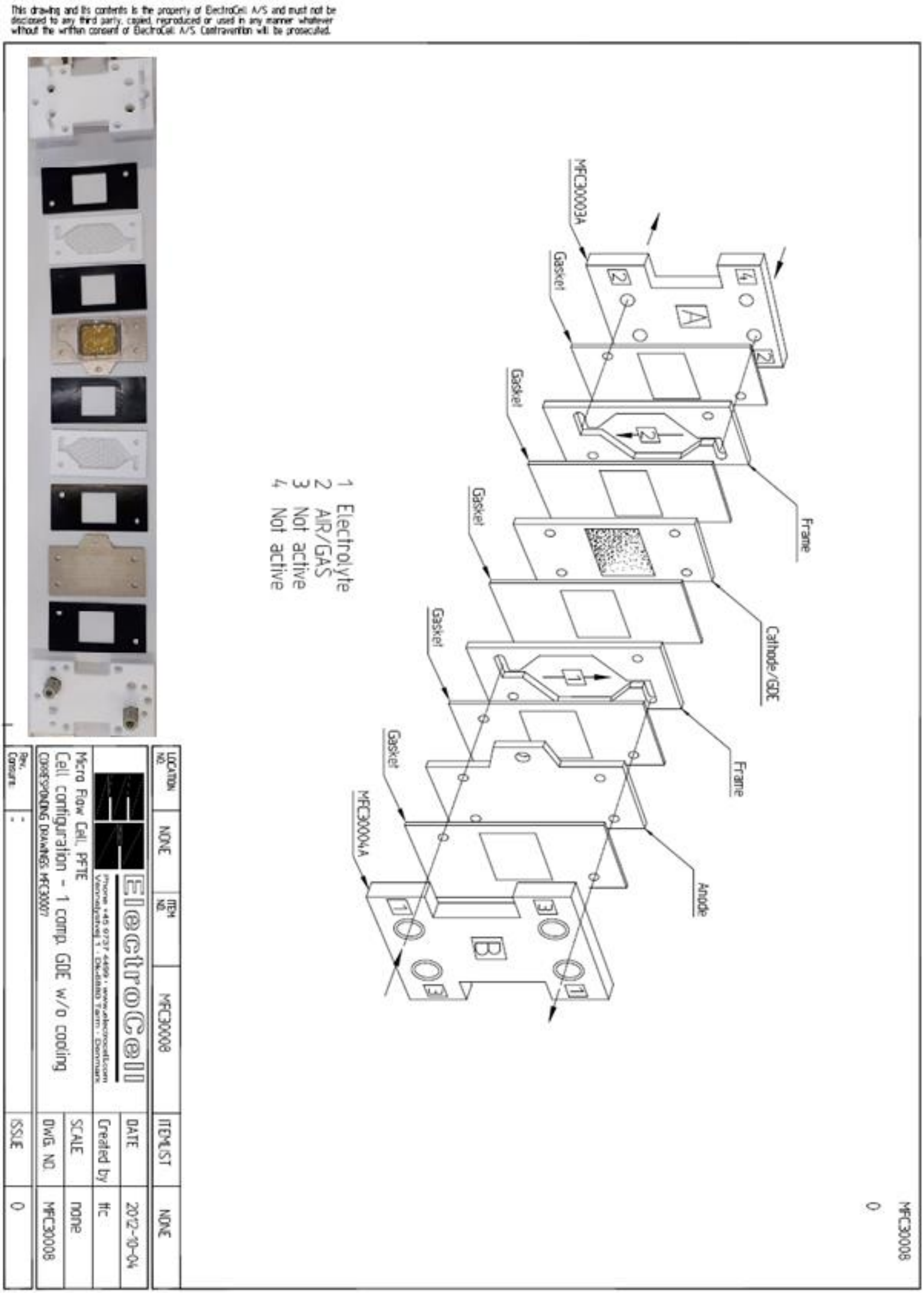

Figure 16 Expanded view of the interior of the Micro Flow Cell. Arrows inside the cell are used to indicate liquid (1) and gas (2) flow directions. [written permission to reproduce this technical drawing is given by ElectroCell]. The inserted image is the real representation of the same components.

After a third gasket a PTFE flow frame identical to the one on the gas side is used on the liquid side of the cell to mix and transport electrolyte (1M KOH) through the compartment. Whereas the flow direction on the gas side is not really relevant (since the flow is governed by pressure and not by gravity), the flow on the liquid side goes from bottom to top in order to allow formed O_2 to rise up in the electrolyte and thus find its exit route. Reversed flow (top to bottom) on the liquid side can cause undesired gas build-up within the cell, reducing active catalyst area in contact with the electrolyte. After a fourth gasket with punched holes for electrolyte transport the anode plate can be found. This plate is made of Ni(s) and is used to perform the OER. Although Ni(s) is not an optimal catalyst for oxygen evolution, the focus of this research is on the MEA/cathode, therefore an unoptimized (yet stable) Ni(s) anode has more of a complementary nature and will suffice for the comparison of these experiments. After the anode plate a final gasket with punched holes (for in/outlet 1, inactive entries 3 are closed off) can be found before closing the cell with the second PTFE end frame (B). The entirety of the cell components as shown in fig. 16 is encased in stainless steel end frames and tightened by 10 mm nuts and bolts as was depicted in fig. 14. The external compression of the cell is done by applying a 4 Nm moment to each of the bolts with a torque wrench to provide a uniform pressure on the cell and causes the softer rubber layers to indent and close any spacing between individual layers, providing a leakproof whole.

3.3 MEA working principle and preparation

In the previous section the cathode/GDE compartment was skipped for the moment due to the complexity of the system. In reality the cathode/GDE area houses the MEA and the GDL. To clarify, fig. 17 a. shows a schematic drawing of the flowcell in the BPM setup and 17b zooms in on the components within the cathode/GDE compartment. Figure 17b in particular contains a lot of information, since it includes the (theoretical) pathways of all involved molecular species, assuming there are no other products than CO and H_2. The working principle of this system from left to right is as follows:

The anolyte solution provides H_2O to the BPM (Fumasep FBM, FuelCellStore), where it can penetrate through the AEM to reach the SCR. Here H_2O is split into OH^-, which returns to the anolyte via the AEM to fuel the OER, and H^+/H_3O^+, which travels through the CEM to be used in the CO_2RR/HER. Simultaneously, on the opposite side of the cell, the gas compartment is filled with CO_2. The GDL (Sigracet 39BC, FuelCellStore) allows for free CO_2 transport through the large pores of the carbon paper backing (5% PTFE) on the gas side. To prevent liquid crossover, the liquid side of the GDL consists of a so-called microporous layer (MPL), which has a much denser structure and higher hydrophobicity (23% PTFE) [67]. Although the MPL prevents liquid crossover, it is mentioned that this layer can be mass transport limiting at high current densities. After traveling past the GDL it is not sure whether CO_2 stays in a gaseous phase, or undergoes short distance dissolution before it reaches the Ag catalyst. Since it is difficult and time consuming to determine the exact working principles at the GDL interface this aspect is outside of the scope of this project.

After H^+/H_3O^+ is transported through the CEM of the BPM, it can be used alongside CO_2 in the CO_2RR (or in the competitive HER) at the Ag catalyst (Silver Gauze, 1024 mesh/cm^2, 0.12 mm wire diam., MaTecK). During the CO_2RR, H^+ and CO_2 are effectively converted into H_2O and CO. Parallel to this reaction the HER converts H^+ into H_2 as an unwanted side product (although the CO-H_2 mixture can be used as syngas, higher purity CO has greater value). Since CO and H_2 have poor solubility and the BPM prevents product crossover to the anolyte, these products tend to migrate back into the gas phase. Oppositely, the H_2O side product of the CO_2RR cannot permeate though the MPL, but can be absorbed back into the BPM to fuel the water dissociation step, as well as keeping the membrane moistened.

Product details of the BPM, GDL and Ag-mesh can be found in Appendix B.

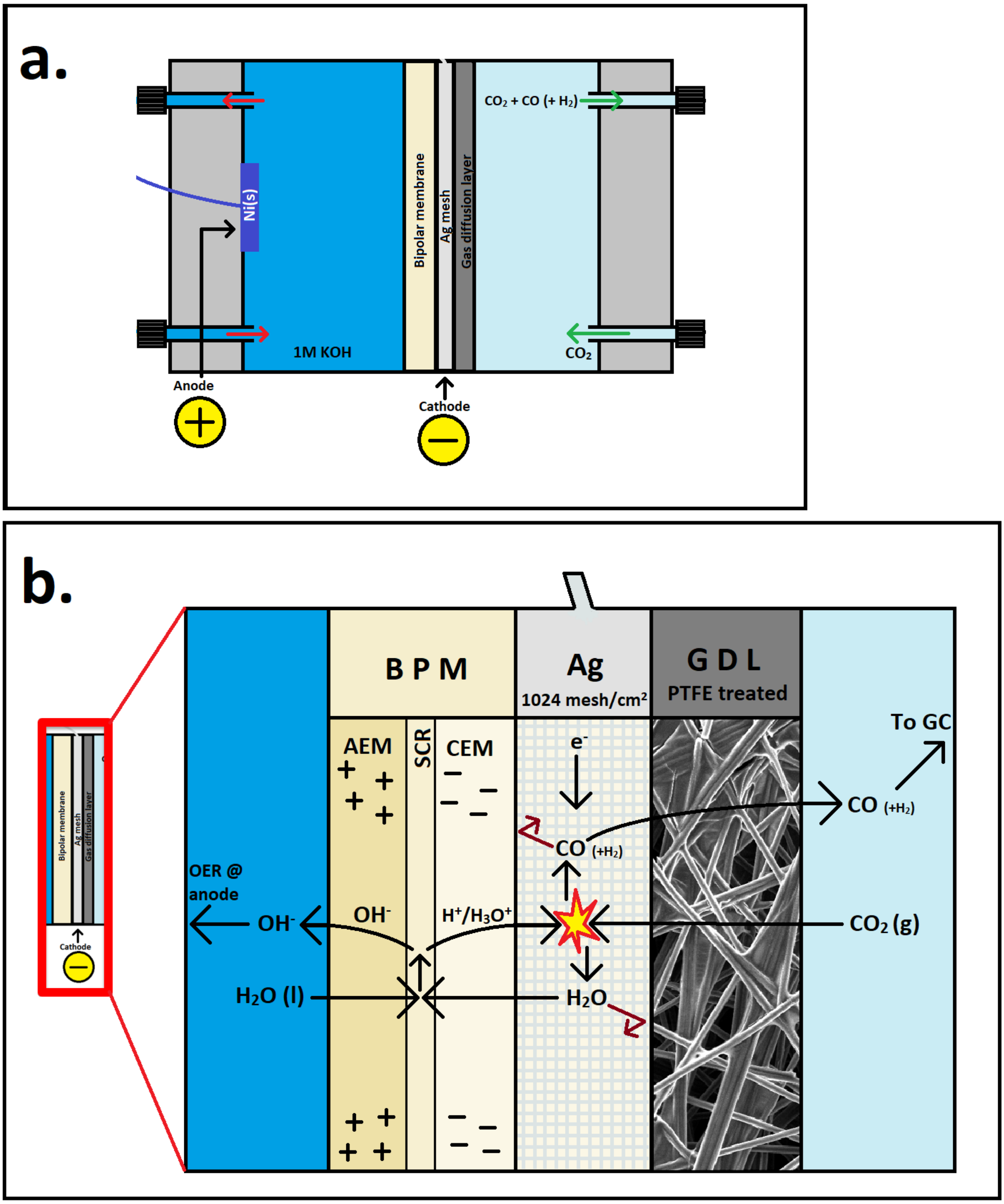

Figure 17 a. Schematic view of the flowcell operating with a liquid and gaseous compartment for the BPM setup. At the anode the OER is displayed. b. Zoom-in of the cathode/GDE compartment. Here the BPM, Ag cathode and GDL are closely packed together. The theoretical molecular pathways show the functionality of each component. One important assumption is that the gaseous products (CO/H_2*) formed at the Ag-mesh cannot move through the BPM, and vice versa the liquid products (*H_2O*) cannot be transported through the PTFE treated GDL (dark red arrows).*

In the first experiment the BPM, Ag-mesh and GDL are simply pressed together in the cathode/GDE compartment, as shown in fig. 17, with the help of a Ni mask to keep the layers pressed together and a silicon spacer to prevent liquid from seeping through the edges of the GDL to the gas compartment.

The second experiment interchanged the BPM for an AEM while using the same Ag-mesh and GDL configuration. The BPM was able to maintain a pH difference between the anode and cathode, thus resulting in a basic anolyte and a local (in the cathode/GDE region) neutral/acidic catholyte. When an AEM is utilized the anolyte remains unchanged, however, the catholyte no longer has a separate 'BPM protected' environment and will become alkaline as well. Because of this the CO_2RR cannot be supplied with H^+ to fuel its reaction, but has to obtain its protons directly from H_2O, thus producing OH^- which increases local pH even further. These reaction conditions take away the extra cost of the BPM, but induce extra potential losses to perform the CO_2RR, due to the basic environment. According to the same reasoning it is expected that the AEM setup will require a higher activation potential to start forming products that require H^+, due to the high local pH near the active catalyst area. In other words, at a constant applied voltage less current will be produced, but in exchange hydrogen evolution, which relies solely on the H^+ concentration, will be suppressed, resulting in a higher selectivity towards CO.

The third experiment uses the same BPM - Ag-mesh - GDL configuration as the first setup, but in addition it has an applied ionomer solution between the BPM and Ag-mesh, consisting of 20 wt.% sPEEK polymer solution in N,N-dimethylacetamide (DMAc) (Fumion® FKE-solution-2, FumaTech BWT GmbH). The goal of applying this layer is improving proton conductivity and transport while still allowing CO_2 to reach the reactive surface. Another benefit of this is reducing the distance between the reactive surface of the Ag-mesh and CEM side of the BPM, which allows the direct use of protons from this layer instead of dissolution . On the other hand the increased proton gradient towards the reactive surface might go paired with increased H_2 formation or CO_2 active site blockage at the Ag-mesh. Since no literature can be found for a feasible application method of this chemical compound it is assumed that the vapor pressure of the DMAc solvent is sufficient to remove itself during and/or after application, thus leaving the sPEEK polymer on the CEM side of the BPM. The method of application that will be used is spin-coating, which should provide a uniform heterogeneous layer of ionomer, providing both covered and uncovered areas at the Ag-mesh with regular intervals. Before applying the ionomer solution to the (expensive) Ag-mesh, the spin-coating method will first be practiced on a stainless steel mesh with similar physical properties (sample size, mesh size and wire diameter) to determine the most effective application method to achieve the desired result. This is done by changing the applied quantity of ionomer solution ($m_{ionomer}$), the rotational speed of the spin-coater (RPM) and the duration of spin-coating (t).

3.4 Electrolyte preparation

In order to exclude electrolyte contributions from the comparison of the different MEA systems a single favourable electrolyte is chosen and kept constant throughout all experiments. The electrolyte is mainly present as anolyte (electrolyte in the anode compartment) and is thus tuned towards the optimisation of OER. As shown in Table 1 hydroxyls cause the OER to perform at a lower potential. Therefore a 1 molar potassium hydroxide (1M KOH) solution is chosen as the anolyte for each experiment. KOH is an alkaline medium which consists of 1M OH^- anions and 1M K^+ cations. Theoretically a hydroxyl concentration of 1M result in a pH of 14, however in practice this value will decrease over time (to pH 13.5-14) due to acidification by dissolution of atmospheric CO_2. Although ion crossover of K^+ across the membranes has a minor effect on ionic resistance as well as pH, it is assumed that in all experiments this effect is similar. The preparation of the 1M solution is done for each experiment by diluting a 45 wt.% KOH stock solution (Alfa Aesar, 45%) with Milli-Q water (R = 18.2 MΩ.cm) according to Table 4. For each experiment a 50 mL solution is prepared. A pH measurement is taken from the solution to ensure a 'near-pH 14' mixture is achieved.

Table 4 Preparation calculation for a 50 mL 1M KOH solution from a 45 wt.% KOH stock solution.

Target solution	1 M KOH = 1 mol KOH/L sol.
M.W. KOH	56,11 g KOH/mol
45 wt.% KOH	56,11 / 0,45 = 124,68 g KOH(45)/mol
concentration	1 M = 124,68 g KOH(45)/L
50 mL solution	**6,234 g KOH(45)/ 50 mL H_2O**

3.5 Experimental setup and equipment

Besides the cell configuration as shown in fig. 16 and 17a, the schematic of 17a can be expanded to display the total experimental setup including all components and measurement devices that are part of the setup (fig. 18). Note that this setup was initially used for the BPMEA case as indicated by the BPM near the Ag-mesh cathode. For the AEMEA case the BPM was interchanged with an AEM.

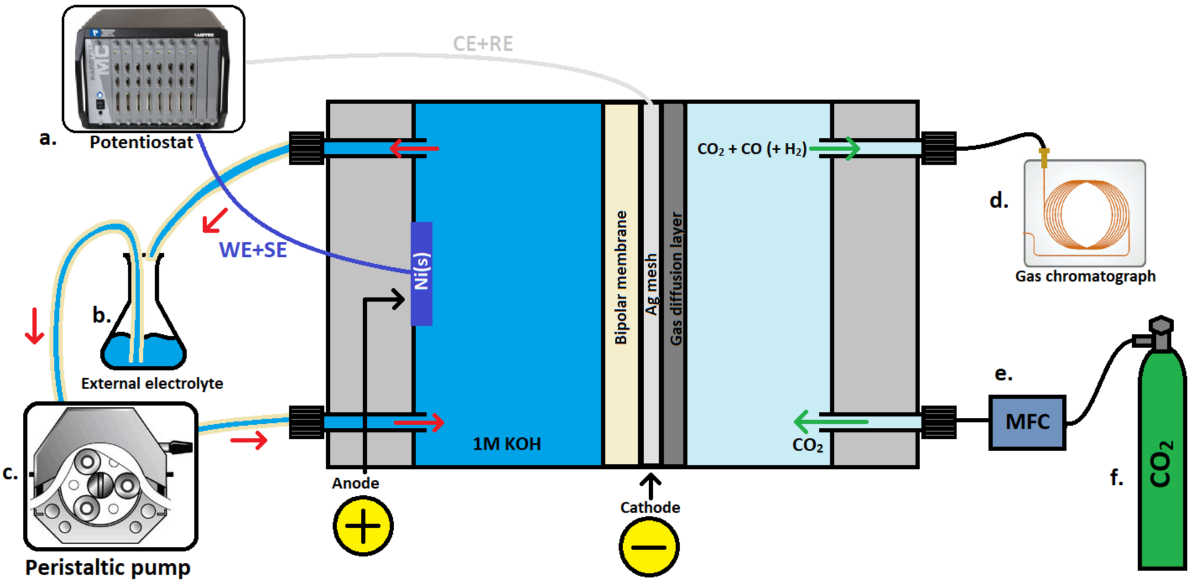

Figure 18 Experimental setup with all external cell components, including (a.) a potentiostat for electrochemical characterisation, (b.) an external electrolyte compartment, (c.) a peristaltic pump for electrolyte circulation, (d.) a gas chromatograph for product identification and quantification, (e.) a mass flow controller for CO_2 and (f.) a high pressure CO_2 bottle.

Going through the setup according to the alphabetical annotations in fig. 18 the following components can be found:

The potentiostat (fig 18a) used in this research is a ParSTAT 4000 (Princeton Applied Research [68]) allowing for a great variety of single-channel electrochemical measurements. This system is basically a strong controllable battery, and simulates the application of e.g. excess grid power. Initially a 1 mm diameter reference electrode was present in the anolyte to perform a 3-electrode measurement, however, due to the rapid gas evolution the small electrode sensor was often blocked and thus provided inconsistent voltages during operation. This led to the use of a single channel 2-electrode operation over the entire cell, since the main goal of the research is to measure differences between different cathode configurations, while the OER at the anode is assumed to be non-limiting. The potentiostat measures via 4 different electrical connections to the cell. The Working and Counter Electrodes (WE and CE) are used to measure current, while the Sense and Reference Electrodes (SE and RE) are used to monitor voltage. The WE and SE are connected to the anode, the CE and RE are connected to the cathode. These connections cause an applied positive voltage to respond with a positive current. More detail on potentiostat measurements can be found in section 3.6.1.

The external electrolyte compartment (fig 18b) is a 100 mL Erlenmeyer flask in which the previously described 1 M KOH anolyte was placed. The inlet of the cell is fed from the bottom of the vial, while the outlet drips back into the vial from above the liquid level to allow formed gas products to escape, as is depicted by the length of the in- and outlet tubing in fig. 18. In order to avoid acidification of the electrolyte by atmospheric CO_2, the Erlenmeyer was taped off at the top after insertion of the tubing.

During experiments, where GC measurements were performed on the cathode side, it was found that the amount of current consumed did not match the quantity of measured cathode products, implying that not all products were collected. In order to measure cathodic product crossover to the anolyte, the GC was connected to the anolyte compartment instead of the cathode gas outlet. To facilitate the anodic GC measurement a simple Erlenmeyer would not suffice and so the anolyte compartment was redesigned to be airtight as shown in fig. 19. This compartment allowed gaseous products at the anode (O_2 and crossover products (H_2, CO)) to be taken away by an inert carrier gas to consecutively be fed to the GC. More details on the GC and this setup can be found in section 3.6.2.

Figure 19 Altered anolyte compartment for GC measurements made from a deposition cell. In order to adequately measure gas products at the anode an airtight system is required, while being able to circulate electrolyte.. This is achieved by internally applying rubber O-rings and using 4 in-/outlets: 1. anolyte outlet coming from the cell. 2. anolyte inlet going to the pump/cell. 3. GC outlet taking the gas products away. 4. inert carrier gas inlet. This can be either Ar, He or N_2. The two inlets indicated with an X and tape on top are sealed from within by a circular rubber instead of an O-ring

The peristaltic pump (fig 18c) is used to circulate electrolyte through the cell via the external circuit. The used pump was a Masterflex® L/S Precision Variable-Speed Console Drive (Cole-Parmer). This device uses a peristaltic motion to compress the tubing partially and thereby push the electrolyte towards the cell at an accurate rate. To ensure that the peristaltic motion would not damage the tubing, specialized PharMed® BPT tubing (Saint Gobain) is used, which has high chemical (for pH) and mechanical (for compression) durability. The connection to PTFE tubing of different size was ensured by using 2-component epoxy (LOCTITE®), this was also done for connections to the cell.

The gas chromatograph (fig 18d) used in this research is a CompactGC4.0 (GAS-analyses). After calibration, this robust system utilises three separate columns simultaneously, allowing for the detection of most gasses. Channel 1 uses flame ionisation detection (FID), which detects products based on boiling point. This line is used to detect hydrocarbon products. During this research it is expected to only form CO and H_2, but no hydrocarbons, therefore this line will only be used as a check for irregularities. The second and third columns make use of thermal conductivity detectors (TCDs) that respond to the electrical conductivity of the sampled gas compared to a reference gas. Since each atomic species has its own thermal conductivity, this method can be used to detect a great variety of products. The reason for measuring with two separate TCD columns in the GC is the use of different internal reference gasses. The second column (TCD-1) makes use of helium (He) as its carrier gas. This makes it helpful for monitoring O_2 and CO, but has inconsistencies when measuring the H_2 content of a stream, since He and H_2 are comparable elements in terms of thermal conductivity. A similar situation is present in the third column (TCD-2), which makes use of argon (Ar) reference carrier gas. This makes it a potent device for quantifying H_2. Argon does, however, have similar thermal conductive properties to O_2. By choosing an appropriate carrier gas and detecting responses in different columns the concentrations, and thus the selectivity of products, can be identified. More on the specific GC measurements can be found in section 3.6.2.

The inflow of CO_2 is regulated by a mass flow controller (fig 18e) and allows for accurate tuning of the gas compartment inflow. The mass flow controller (Bronkhorst High-Tech) is used to provide a CO_2 stream at a rate between 10 and 20 mL/min. The rate of gas flow is one of the required parameters to calculate the selectivity, since the flowrate determines the dilution of the formed products in gas phase. The gas flow rate given by the mass flow controller is checked using a handheld flow meter before and after the cell to ensure no gas leakage is present in the gas compartment.

The CO_2 gas flow originates from a CO_2 bottle (fig 18f) which contains pure CO_2 with only trace quantities of contaminations. To ensure no unknown species end up in the data, background measurements were taken directly from the bottle, as well as backgrounds after putting the cell in place, without applying a current.

NOTE: before using the setup as shown in fig. 18, a bubbler was placed between the mass flow controller and the cell. Similar research [69] utilizing gaseous CO_2 streams in a MEA or GDE configuration have been found to humidify the gas streams in order to promote the reaction rate and/or selectivity towards desired products. Despite of this, applying the bubbler caused atmospheric leakage to occur, resulting in a GC measurement of a near-ambient mixture of N_2 and O_2. After being unable to adapt the bubbler to work leakproof as intended it was decided to put this component aside until further progress is achieved.

3.6 Methods of characterisation

To characterize the samples and obtain information on the effectivity of different cell configurations the following methods of characterisation have been used. The two major characterisation tools are the potentiostat measurements and the GC measurements, as previously mentioned. A third technique, SEM imaging, is used to visualise and obtain insight in the physical representation of some of the components, as well as to empirically determine the optimal spin-coating method for ionomer application. Since this research mainly focussed on a system operation point of view, some techniques that focus on bulk chemistry (like XPS and EDX) were not used. In this section the characterisation methods and the performed experiments for each respective technique will be discussed.

3.6.1 Potentiostat measurements

Figure 20 The ParSTAT 4000 by Princeton Applied Research

In order to compare the different systems, the ParSTAT 4000 potentiostat (fig. 20) will be used to apply a fixed potential to the cell at a level where a significant current of 100mA is obtained. Although industrial purposes will require even higher currents, the value of 100mA is a good first requirement for figuring out how to operate without damaging the system.

The initial experiment performed is cyclic voltammetry (CV), by which the current of the system will be measured as the total cell potential is cycled between a wide range of 0 and 3 V. This not only allows a suitable potential to be found for use in future experiments, but also ensures that catalysts reach a stable state prior to chronoamperometry tests. This experiment is performed on the BPM - EC GDE configuration. After performing the initial CV experiment and identifying a potential needed to achieve a 100 mA current, the following compositions are exposed to the empirically determined potential for 1 hour in a so-called chronoamperometry measurement.

A chronoamperometry measurement directly shows the activity and stability of the setup by measuring the produced current over time. Once a baseline is established for the BPM – EC GDE configuration, the same cell potential is applied to the other configurations, starting with the BPMEA setup. A consistent applied potential will allow for experience with the customized system to be gained and allow for issues with the setup to be more easily detected and circumvented along the way. Examples of these issues could be based on leakage, cell construction, product collection and external component connection (e.g. tubing and bubbler). The third measured system will be the AEMEA, which replaces the BPM with an AEM, while the fourth and final setup applies the ionomer solution to the BPMEA configuration. By taking and comparing the chronoamperometry data of all four experimental configurations, the optimal configuration will be determined by the displayed activity and stability at the fixed potential. It is important to note that these results are preliminary indicators of efficiency and require matching gas chromatography data to become conclusive.

3.6.2 Gas chromatography

Gas chromatography (GC) will be conducted simultaneously with the potentiostat measurements using the system shown in fig. 21. As explained through fig. 18 the GC uses three separate columns to detect the constituents and quantities of the products in the gas feed. From these values the Faradaic efficiency (F.E.) can be calculated. This efficiency describes the selectivity of each product by comparing the amount of electrons (or charge) put into that one product versus the total amount of electrons that are consumed at the cathode. After taking a product sample every 3 minutes, the GC lets these samples run through each column and monitors the electrical response from the FID or TCD. The quantity of products are converted into a peak area. Before running these experiments a calibration is

Figure 21 The gas chromatograph by Global Analyser Solutions™

performed on three bottles with known quantities of possibly interesting chemicals. The calibration provides the GC with a ratio of peak area vs concentration, which can be extrapolated to convert an experimentally found peak area into a concentration in ppm. The concentration can then be used in the equation for Faradaic efficiency [6-8]:

$$F.E. = \frac{\theta_{prod}}{\theta_{total}} = \frac{\theta_{prod}}{I * t} \qquad [6]$$

$$\theta_{prod} = z * N_{prod} * F = z * \left(\frac{A_{peak}}{\alpha_{prod}} * \varphi\right) * \frac{P}{R * T} * F \qquad [7]$$

$$F.E. = \frac{z * \left(\frac{A_{peak}}{\alpha_{prod}} * \varphi\right) * \frac{P}{R * T} * F}{I * t} \qquad [8]$$

In equation [6] $\theta_{prod/total}$ indicates the number of electrons used in the reaction of the interested product/in total. I*t is the potentiostat measured current times the duration of the experiment. Equation [7] describes the amount of electrons attributed to the product of interest, where z is the stoichiometric number of involved electrons per molecule of formed product, N_{prod} is the total amount of product and F is Faraday's constant. Since it is difficult to determine N_{prod}, the ideal gas law (PV = NRT -> N = PV/RT) can be used to calculate this term. The pressure (P), gas constant (R) and Temperature (T) have straightforward values. The volume (V) can be determined from the GC measurement. The GC integrates peak area A_{peak} and uses the calibration curve constant (α_{prod}) to calculate the concentration of the product. This value can then be multiplied by the flowrate of the carrier gas (φ) to find the volume of the product. Equation [6] and [7] can be combined into equation [8] to calculate the Faradaic efficiency.

3.6.3 SEM imaging

A scanning electron microscope (SEM) is used to visualize samples on a micrometer to nanometer scale, depending on what magnification is interesting to the sample at hand. The used SEM (JEOL JSM-6010LA, fig. 22) makes use of a medium energy (1-20kV) electron beam in vacuum that scans over the surface with a spot size (beam width) of 20 to 100 nm. The secondary electrons scatter off the surface and their energies are measured. The energies are averaged for each location and displayed in contrast to the energy levels of other locations. Using a larger spot size gives a smoother image because of the averaging of many scattered electron energies, whereas a small spot size gives greater detail (smaller features can be distinguished). The downside of a smaller spot size is that images become in grainy and noisy due to the larger deviation in energies of a smaller amount of electrons. Besides secondary

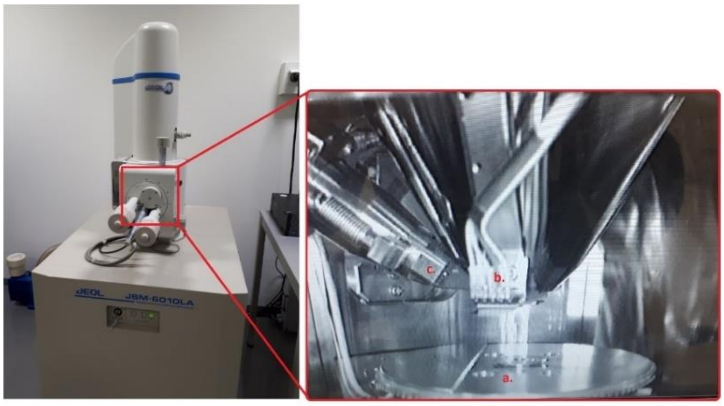

Figure 22 The JEOL JSM-6010LA scanning electron microscope (SEM). The right image shows the internal structure of the SEM, with the most important components indicated. a. The sample holder, b. the electron beam and c. the secondary electron detector.

electrons SEM can also be used to measure Auger electrons to determine surface composition, high energy EDX electrons for bulk composition and backscattered electrons for crystallinity information, but this research only makes use of the secondary electrons to obtain topographical information.

energy EDX electrons for bulk composition and backscattered electrons for crystallinity information, but this research only makes use of the secondary electrons to obtain topographical information.

The SEM was first used to look at the Sigracet 39BC GDL. This is done for two reasons: on one hand to practice with the SEM on a simple structure, on the other hand to display the difference between plain carbon paper and carbon paper with a microporous layer, which plays an important role in providing gas transport and acting as a hydrophobic barrier. After using the SEM to these means, it is was also used for finding an adequate ionomer application method. The ionomer solution, being 20 wt.% sPEEK in DMAc, had no clear instruction on application, nor was a comparable application method found online. Therefore, the optimal method of spin-coating was determined by changing spin-coating parameters and looking at their respective SEM images. After finding an effective application method on a stainless steel mesh, similar approaches were used for applying ionomer to a BPM + stainless steel configuration. Finally the best method was used on the BPM + Ag-mesh. The production of the final BPM + Ag-mesh was measured by SEM after operation, since sample preparation for the SEM required cutting the sample down to the size of the SEM sample holder.

4. Results

In this section the results for performed experiments are shown. Some experiments lead to direct discussion, which will be mentioned here as well, since these unforeseen results formed the basis for new insights and additionally performed experiments. During all experiments the ElectroCell Micro Flow Cell is used as was schematically displayed in fig. 16. A picture of the real cell build-up is shown in fig. 23 and it can be assumed this setup is used for all experiments unless specified otherwise. To compare different systems the cathode/GDE sample holder (segment 23 e.) is altered between experiments and its composition requires special attention for each experiment.

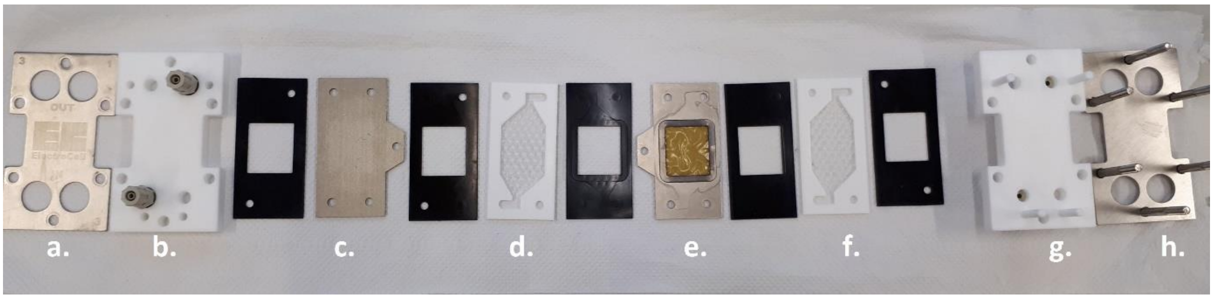

Figure 23 Practical build-up of the ElectroCell Micro Flow Cell. From left to right (excluding the black rubber gaskets): a. anode endplate, b. anode end frame, c. Ni anode, d. anolyte (KOH) flow frame, e. Ti sample holder for cathode/MEA (with visible BPM), f. cathode (gas) flow frame, g. cathode end frame, h. cathode end frame (with bolts). Only section e. is changed for different experiments.

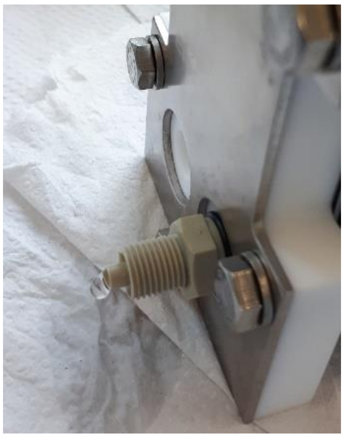

Figure 25 leakage from the gas compartment.

Prior to performing any potentiostat/GC measurements a the cell was built several times to address any leakage of liquid and gas that may arise during operation. It was determined that in order to prevent electrolyte leakage between layers a stronger force on the cell was required. This was achieved by obtaining and applying a torque wrench to increase the momentum on the nuts and bolts up to 4-5 Nm, making the rubber gaskets squeeze more tightly between other layers. Another early stage problem was found on the gas and liquid side inlets. The liquid side inlet had a connection issue between different sizes of tubing. This was fixed by using epoxy to all staged tubing transitions. The gas compartment also showed liquid leakage in the bottom outlet as seen in fig. 24 when using a commercial GDL instead of the EC GDE. Since this was not a connection issue, but an internal issue (there should be no liquid on the gas side) the cathode/GDE was inspected for a closer look. During this time the need of a microporous layer on top of carbon paper was unapparent, resulting in electrolyte seeping through the open pores of the untreated carbon paper (at that time Toray® 060/120 was used). As is shown in fig. 25, localized droplets were visible on multiple spots of the carbon paper. After some it was found that a microporous layer as described in the theory was required to prevent this issue. Sigracet 39BC was then applied in place of plain carbon paper, but some liquid was still observed to seep through the edges of the GDL. This was avoided in the first CV experiments using an additional silicon gasket within the cathode/GDE.

Figure 24 Electrolyte seeping through the GDL towards the gas phase. Red circles indicate visible droplets.

4.1 Cyclic Voltammetry

The first experiments in this research were performed on the ElectroCell bought gas diffusion electrode (EC GDE) as depicted in fig 26. The EC GDE was combined with a BPM in the cathode/GDE compartment and, as with all experiments, measured against the Ni anode in 1M KOH.

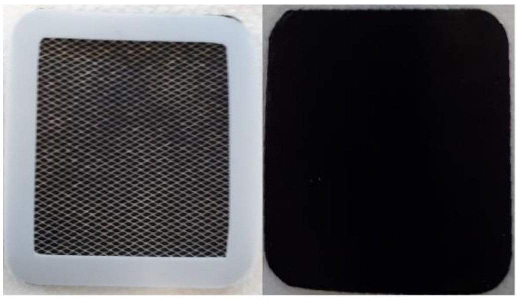

Figure 26 The ElectroCell GDE. Left: the cathode side of the GDE with MPL, integrated Ag mesh and external PTFE frame. Right: the gas side of the GDE consisting of dense carbon fibres.

In fig. 27 the cyclic voltammetry (CV) from 0 to 3 V is shown before and after running the EC GDE for a 1 hour chronoamperometry. As can be seen, both the initial and after 1 hour of operation CVs look similar. After 1 hour of chronoamperometry the CV shows a later onset potential (0.8 V vs. 0.5 V), but a slightly higher maximum current (280 mA vs. 260 mA @ 3V) is found in comparison to the before measurement. The goal of taking these CVs was to determine at what potential to operate the system in order to achieve a current of at least 100 mA, indicated by the orange horizontal line. The forward oxidation curve (upper dark blue line) reaches this value at 2.4 V and 2.35 V respectively for before and after chronoamperometry. To ensure the difference in current for different cell compositions would be measured a slightly higher constant cell potential of 2.5 V was chosen. This is indicated by the orange vertical line. At this potential an initial current of 130-140 mA is measured. During the reverse oxidation curve a current of 90 mA was observed. As can also be seen from this graph is that when higher potentials are applied (>2.8 V) fluctuating values are found. Increased bubble transport out of the cell was detected at the anolyte outlet when operating in this region.

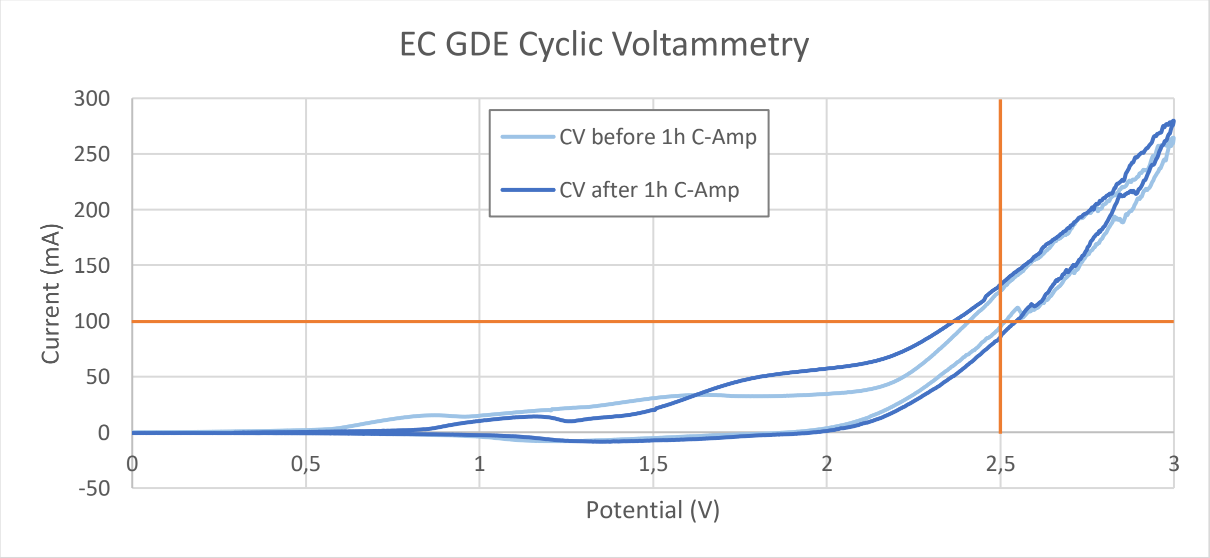

Figure 27 Cyclic voltammetry for the EC GDE sample before (light blue) and after (dark blue) 1 hour of chronoamperometry.

A CV was also taken from the BPMEA, of which the cathode/GDE composition is displayed in fig. 28. The initial CV measurements with the BPMEA did not include the silicon spacer shown on the right. The planar surface area of the sample holder was 30 mm x 34 mm (= 10 cm^2). Due to the use of a porous Ag-mesh the absolute surface area of the sample was estimated to be 6.2 cm^2 (calculation in Appendix B). After liquid crossover was detected at a later stage around the edges of the (not perfectly cut) Sigracet 39BC GDL, a silicon spacer with shape identical to that of the cathode/GDE closing frame was added between the GDL and cathode/GDE frame. By compressing all layers, including the silicon spacer, the frequency of liquid crossover events was reduced significantly.

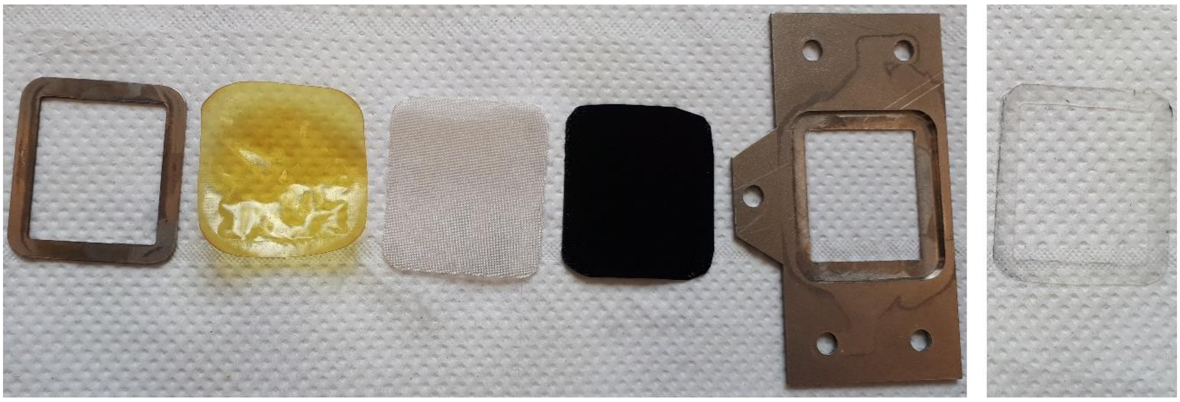

Figure 28 Configuration of the BPMEA in the cathode/GDE compartment. From left to right: Cathode/GDE closing frame, BPM, Ag-mesh, Sigracet 39BC GDL, cathode/GDE frame and the silicon spacer which was later added to prevent liquid crossover.

A double sweep CV of the BPMEA system was taken from 0 to 5 V at a rate of 0.1 V/s as is displayed in fig. 29. The increase in maximum potential over this sweep from 3 V to 5 V is done for two reasons. First to express the current instability due to increased bubble formation when operating above 3 V and second, this experiment directly shows that the system is capable of producing high currents above 100 mA/cm^2. The highest measured currents were 1440 mA and 1140 mA at 4.83 V_{cell} for the first and second sweep respectively. The slightly lower peak voltage is likely the result of the relatively fast sweep rate of 0.1 V/s. The corresponding currents translate to current densities of 232 mA/cm^2 and 184 mA/cm^2 respectively. At the chosen 2.5 V potential the current is initially found to be 257 mA, but stabilized afterwards at 194 mA for the first reverse oxidation curve and second sweep.

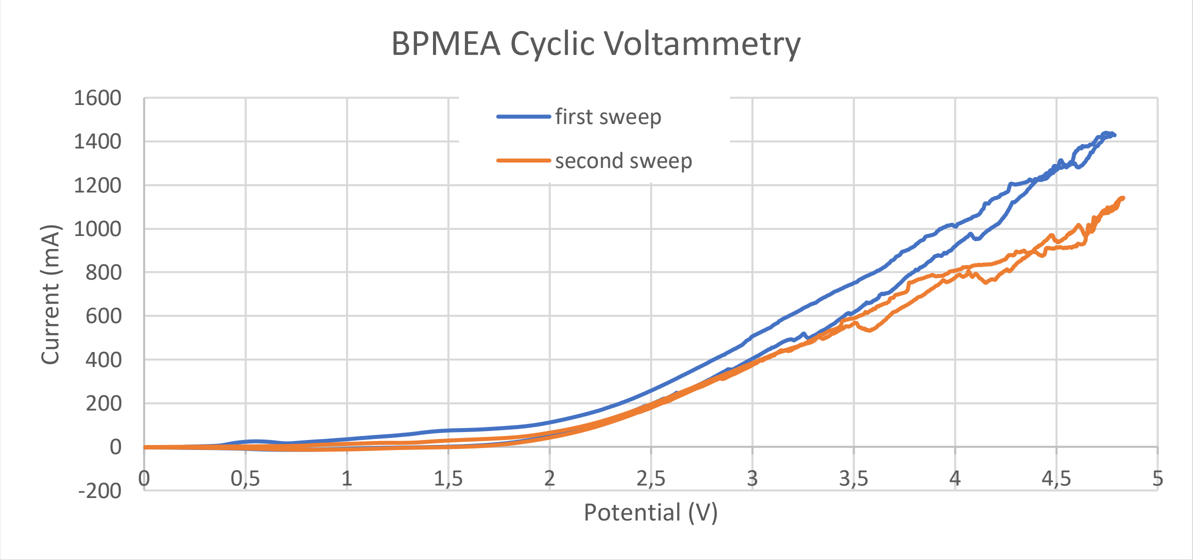

Figure 29 Cyclic voltammetry for the BPMEA system. At high applied potentials (>3 V) fluctuations in current became visible due to bubble formation at the surface. At higher potentials (>4.5 V) current densities over 100 mA/cm^2 were obtained.

4.2 Chronoamperometry and gas chromatography of the BPMEA and AEMEA

The next step was applying the set cell potential of 2.5 V to the BPMEA and AEMEA systems and monitor the current by chronoamperometry as well as the formed products in the gas phase by gas chromatography (GC) in order to compare both systems. During the first measurements it was found that only a fraction of the total current registered by the potentiostat was accounted for in terms of measured products in the GC (according to the Faradaic efficiency calculated by eqn. [8]). Several issues were considered and most time of this thesis was dedicated to identifying and solving this problem. One of the methods of identifying more products was GC measuring the gasses found in the anode outlet, as is described in section 4.2.3. Moreover on the disparity between product production and detection can be found in the discussion section.

4.2.1 BPMEA

First the BPMEA was tested at a cell potential of 2.5 V. The cathode reactions are of main interest and the anode reaction has more of a complementary nature. During the first experiment a 4 mm reference electrode was used in the anolyte in a 3-electrode setup to measure the potential over the cathode, or in other words, to exclude the anode potential from the 2.5 V total cell potential. A slightly altered flow plate and application of PTFE tape allowed for the leak proof implementation of the reference electrode. The electrode implementation is depicted in fig. 30. During the 1 hour chronoamperometry the potential over the BPMEA was measured and it was found that the gas evolution in the anolyte compartment caused bubble blockage, thus electrical insulation, at the sensing part of the reference electrode. This resulted in extreme potential fluctuations during all measurements. An example of this is shown in fig. 31.

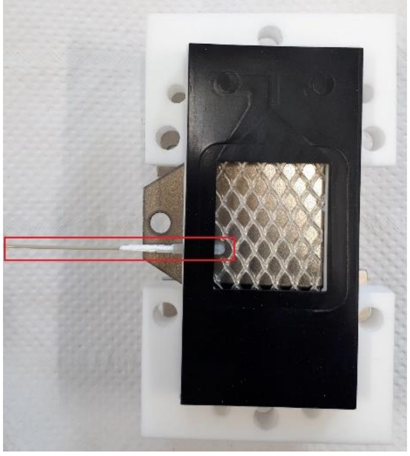

Figure 30 The 4mm reference electrode in the anolyte compartment is applied via an adapted anolyte flow plate

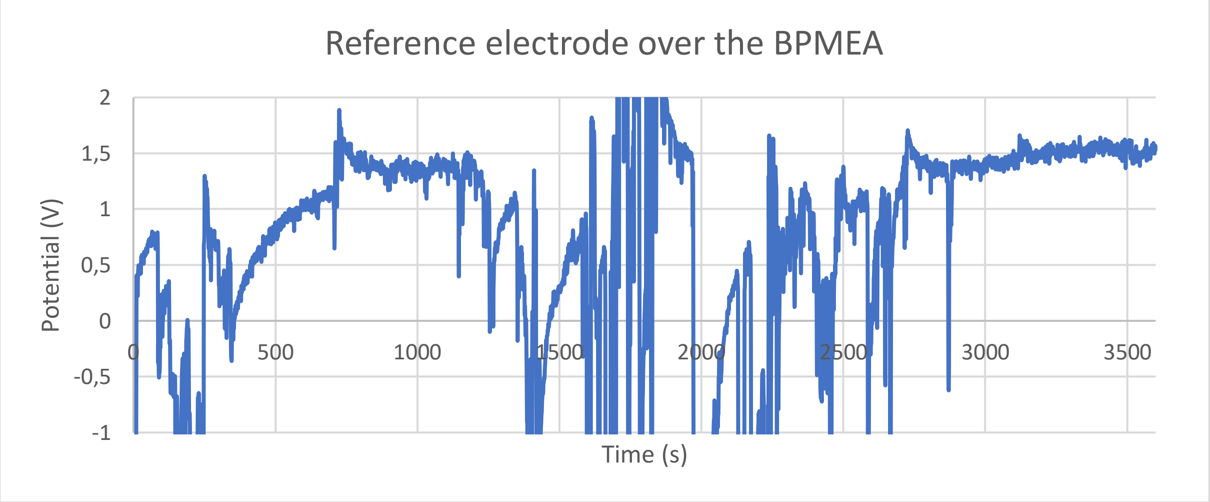

Figure 31 V-t diagram of the reference electrode measuring over the cathode/GDE compartment containing the BPMEA. This segment was measured using the reference electrode in order to determine what fraction of the stable 2.5 V cell potential was put into the cathode reaction(s). Despite the continuous fluctuation due to bubbles on the electrode some stable regions can be seen where roughly 1.5 V is used at the BPMEA.

Due to the great uncertainty and random behaviour of the reference electrode, it was opted to only measure whole cell potential and keep factors that are not interesting to this research, such as the Ni anode, anolyte solution and assembly method as stable as possible throughout all experiments.

After this test the reaction was repeated without reference electrode several times and a series of results are shown in fig. 32. The chronoamperometry measurement from the EC-GDE setup is shown by the black dotted line. Note that the EC-GDE measurement utilized the bubbler, which caused pressure build-up. When this pressure was released at around 2800 s the current momentarily spiked to 300 mA, as if the surface was cleaned/emptied due to the pressure swing. The 4 individual BPMEA measurements, which used a configuration as shown in fig. 28, did not apply a bubbler to the external gas circuit, leading to much more stable current measurements over time.

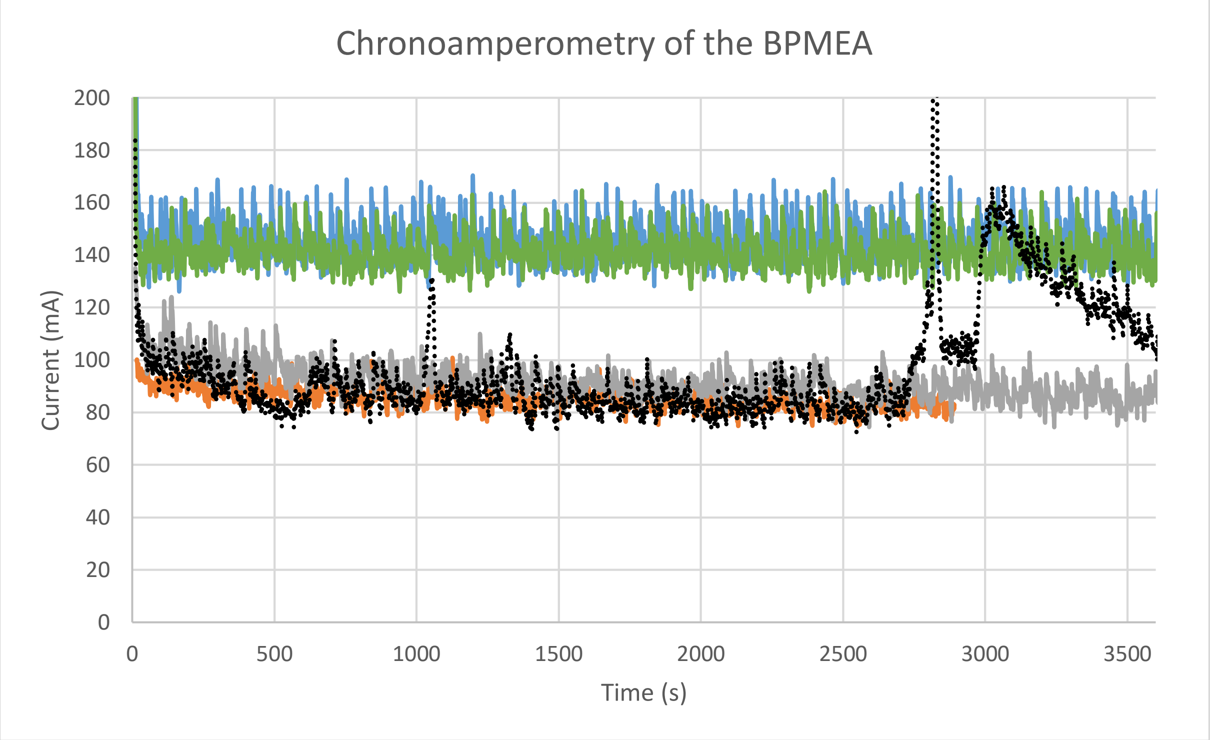

Figure 32 Chronoamperometries of 4 BPMEA systems (colored lines) and the EC GDE system (black dots) as a reference. The current fluctuation for each BPMEA measurement is roughly 20 mA. This is likely also a result from the bubble-rich surface leading to continuously changing active surface area. When different measurements of the BPMEA system are compared a variation between 90 mA and 140 mA is seen. All systems seem rather stable over the entirety of the 1 hour measurement. The lowest (orange) measurement was interrupted abruptly at 2800 s due to a disconnected cable but follows a similar stable pattern.

Aside of the continuous short term fluctuations in all experiments, which are likely to also find their origin in bubble formation leading to temporary surface passivation, a major fluctuation in the activity of different systems is measured (90 mA to 140 mA). Although this deviation is not too extreme, it is clear that some of the BPMEA systems respond different than others in a seemingly equivalent configuration. The reduction in current can have a multitude of causes. Some effects that might have a negative effect on the current are reductions in electrolyte concentration, poorer cleaning of electrodes, the use of older BPMs and GDLs or even sloppy assembly/layering leading to resistances in flow patterns.

A product identification by the GC was done on the products in gas phase simultaneous to the chronoamperometry measurements. All experiments showed similar results, but only the gas product identification of the 100 mA average (gray line) is shown in Table 5 to set an example for why the accuracy of this data is not very relevant. To calculate the F.E. a flow rate of 12.5 sccm of CO_2 and an average total current of 100 mA are used along atmospheric pressure of 1 bar and an ambient temperature of 25 °C.

Table 5 Faradaic efficiencies of products measured in the gas phase during a 1 hour chronoamperometry on the BPMEA. Each 190 s a sample is taken and all products are identified. No CO was measured for this system and merely 1.8 to 2.4 % of the total current could be attributed to H_2 in the cathode gas phase.

Time of meas.	H_2 conc. in ppm	Faradaic Efficiency H_2
0	59	0 %
190	1480	2,44 %
380	1205	1,99 %
570	1156	1,90 %
760	1111	1,83 %
950	1089	1,79 %
1140	1086	1,79 %
1330	1100	1,81 %
1520	1089	1,79 %
1710	1105	1,82 %
1900	1106	1,82 %
2090	1108	1,83 %
2280	1116	1,84 %
2470	1144	1,89 %
2660	1105	1,82 %
2850	1096	1,81 %
3040	1104	1,82 %
3230	1114	1,84 %

As can be seen from Table 5, only the F.E. of hydrogen is shown. This is the case because no other products, such as the expected CO, were measured by the GC. In some experiments traces of CO were detected (< 0.1 % F.E.), but this information is too minimal to make final conclusions. This lead to a series of discussions of what could be causing the low product detection and how to circumvent it. Details about this discussion can be found in chapter 5. Discussion. Experiments that followed from this discussion will be briefly introduced in this chapter before showing their results.

4.2.2 AEMEA

After performing the BPMEA experiments and building this configuration numerous times, the construction of the AEMEA system was done by using the same exact method except for exchanging the BPM with an AEM. This was even more straightforward than the BPMEA, since the orientation of the AEM did not matter where the BPM had to have its CEM directed towards the Ag-mesh and the AEM towards the anode.

The chronoamperometry of 1 hour at 2.5 V cell potential performed on the AEMEA system is shown in fig. 33. As can be seen from the graph the current starts out with a spike of 50 mA and stabilises at 22 mA over the course of an hour. The temporary fluctuation seen continuously is approximately 5 mA. From comparison between the chronoamperometry measurements between the BPMEA and AEMEA it can be seen that currents and fluctuation are both reduced fivefold, and that the stabilisation of the BPMEA happens much faster than the AEMEA.

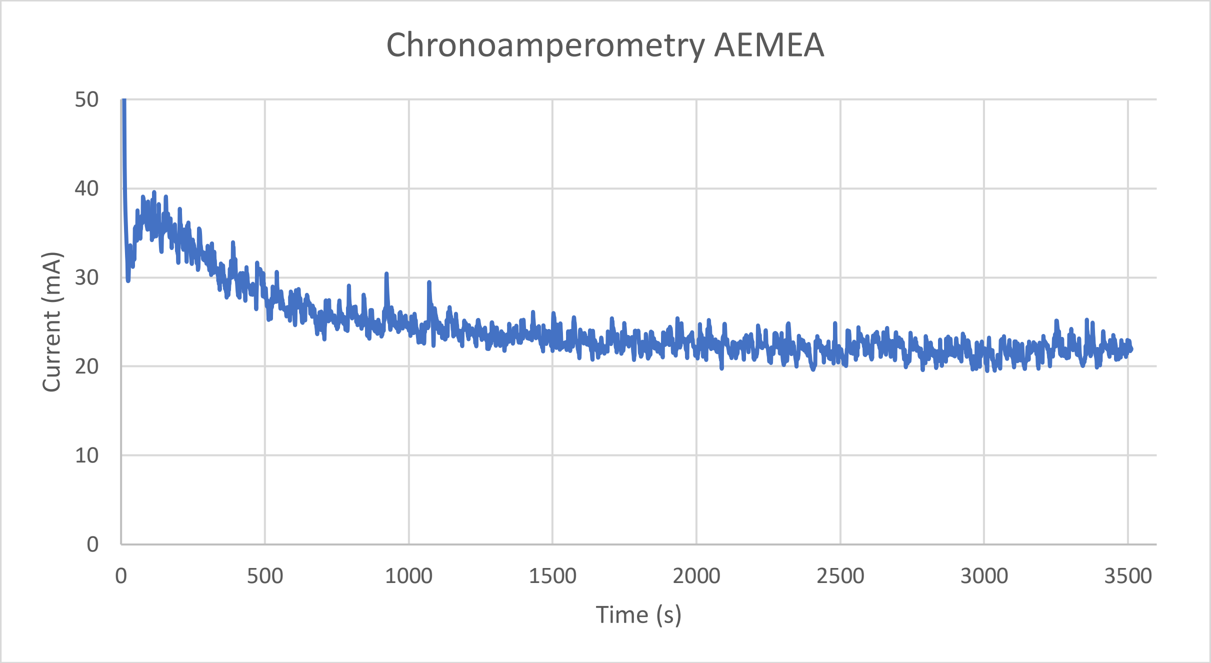

Figure 33 Chronoamperometry of the AEMEA configuration in the cathode/GDE compartment. While applying 2.5 V over the system for 1 hour, it can be seen that the current starts around 50 mA and stabilises at 22 mA. Small continuous fluctuations are attributed to bubble formation at the active surface.

The H_2 and CO concentrations obtained from the GC measurements on the AEMEA system are used to calculate the Faradaic efficiencies in Table 6 A CO_2 flow of 12.8 sccm was used. Other parameters are kept constant. The Faradaic efficiencies for hydrogen are calculated to be 4 to 15 %, indicating a larger proportional transport of formed hydrogen to the gas phase, but still far from all produced products. During the experiment some trace amounts of CO (< 0.8 % F.E.) were measured as well.

Table 6 Faradaic efficiencies of AEMEA products in the gas phase. Besides H_2, trace amount of CO are measured as well.

Time of meas.	H_2 conc. in ppm	F.E. H_2	CO conc. in ppm	F.E. CO
0	63	0,29 %	n.a.	n.a.
190	2151	11,34 %	116	0,61%
380	2490	15,01 %	128	0,77
570	1976	13,34 %	73	0,49
760	1701	11,96 %	52	0,37
950	1428	10,48 %	29	0,21%
1140	1252	9,19 %	24	0,18
1330	1089	8,35 %	13	0,10
1520	1001	7,68 %	10	0,08
1710	842	6,46 %	n.a.	n.a.
1900	760	5,83 %	n.a.	n.a.
2090	720	5,52 %	n.a.	n.a.
2280	677	5,19 %	10	0,08
2470	688	5,28 %	n.a.	n.a.
2660	658	5,05 %	n.a.	n.a.
2850	598	4,59 %	n.a.	n.a.
3040	562	4,31 %	n.a.	n.a.
3230	540	4,14 %	n.a.	n.a.

As shown in Table 6, the concentration of CO peaks early around 0,77 % and then slowly dies out over the course of 20 minutes. The first GC measurement at 0 s was a blank taken from the CO_2 bottle through the cell while the potentiostat was still off. The blank indicates that the trace amounts of CO found during operation were not coming from the gas bottle or that it was a remainder in the GC of a previous test. The degradation patterns of CO and H_2 combined show that on one hand it becomes less likely for products to be transported to the gas phase over time and on the other hand that the production of H_2 over CO becomes more dominant as the reaction goes on. However, the low fraction of measured products make any of these claims non-conclusive.

4.2.3 Anode measurements of the BPMEA and AEMEA

The disparity between formed and found products was so significant (best case: 15% of all products were measured) that this required further attention before moving on to the next experiments. After being unable to find any leakage of gas out of the cell, it was considered that products might find a way to circumvent the membrane preventing product crossover. In order to test this hypothesis it was decided to measure anode products while performing the exact same experiments as before. To do so the anolyte flask needed to be modified to be a gastight container that was fed with a carrier gas and still allowed for the circulation of electrolyte, while also enabling the extraction of gaseous products through the GC. To enable this set of specifications the compartment shown in fig. 19 was built. The cathode side gas phase entry was still fed with a 12.6 sccmCO_2 stream, while the anode products were brought to the GC with the use of carrier gasses as described in fig. 34. The chronoamperometry measurements for the BPMEA and AEMEA are shown in fig. 34 to ensure that currents of similar quantities to the previous experiments were present while measuring the anodic products. Theoretically this stream should only contain O_2 gas from the anode OER if no product crossover is happening.

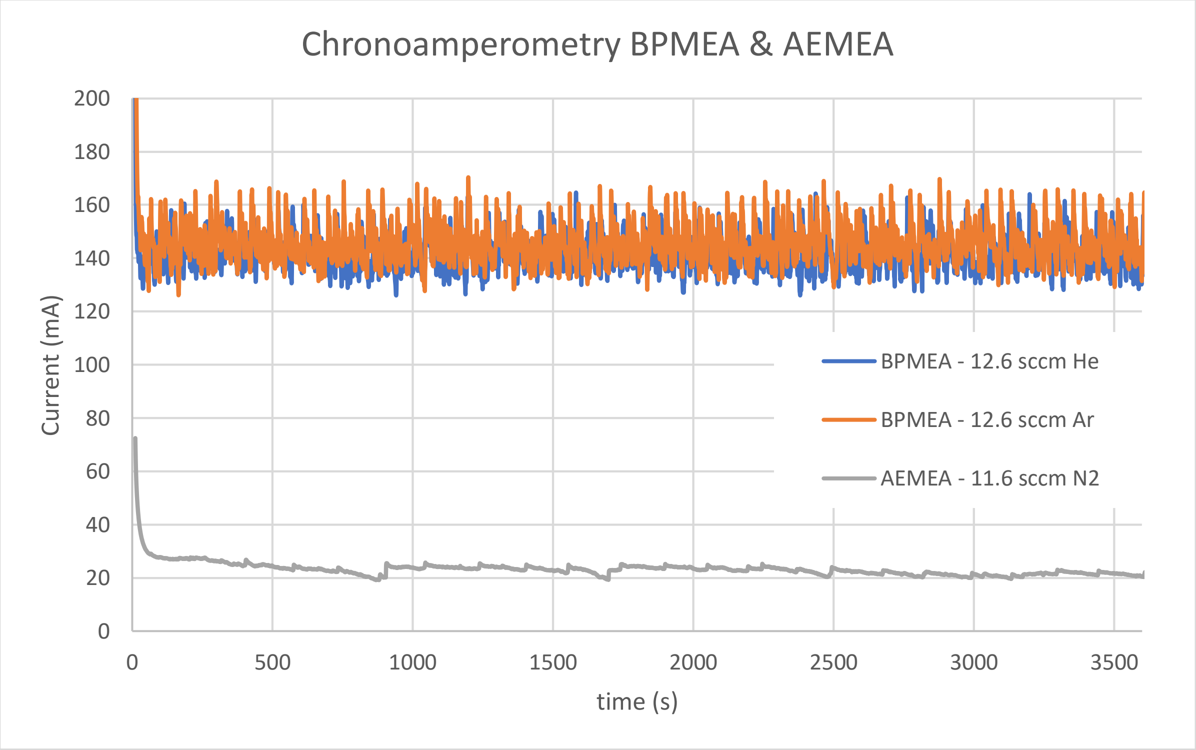

Figure 34 Chronoamperometry measurements of the BPMEA and AEMEA cells when measuring anode products with the GC. With an average current of 140 mA, the two BPMEA graphs shown here look near identical to the upper two BPMEA measurements shown in fig. 32. The AEMEA also shows consistency in respect to fig. 33 with an average current just above 20 mA. Although not visible in the BPMEA graphs, every 3 minutes the GC measurements cause a minor spike in the AEMEA cell current due to a minor pressure swing caused by the GC taking a sample.

Fig. 34 shows that similar results were obtained to the previously shown results and that the anode compartment addition as well as the use of different carrier gasses do not influence any of the systems.

Before showing the GC results of this experiment, it is important to note that two carrier gasses were considered due to their benefits and limitations to the GC. The first carrier gas, argon is used for the BPMEA system. This gas has an issue as the thermal conductivity of argon and oxygen are also close to each other (k_{Ar} = 0.016 W/(m*K), k_{O2} = 0.024 W/(m*K)). Ar as a carrier gas therefore covers the produced oxygen peak (partially) in its background. Nitrogen, the carrier gas used in the AEMEA case, does not interfere with the GC readings of hydrogen and oxygen, but does shade over the 'atmospheric background' (30% O_2, 70% N_2) found in all measurements.

The gas chromatography measurements taken from the BPMEA – 12.6 sccm Ar and AEMEA – 11.6 sccm N2 systems are shown in Table 7. During these experiments no CO was found.

Table 7 Anodic gas GC measurements of the BPMEA and AEMEA systems. As can be seen in both systems, massive amounts of hydrogen are found. The first two measurements were before the potentiostat was turned on. After stabilisation the BPMEA accounts 90% of the total current being used for H_2 that is found at the anode outlet. For the AEMEA the Faradaic efficiency goes over 100%, which is impossible, but does indicate almost all product being H_2 and leaving through the analyte exit. The overshoot of F.E. is caused by the measured concentrations far beyond the calibration limit.

BPMEA 12.6 sccm Ar		
Time of meas.	**H_2 conc. in ppm**	**F.E. H_2**
0	471	0,56
190	427	0,51
380	36034	42,75
570	65654	77,90
760	71596	84,95
950	73775	87,53
1140	74515	88,41
1330	75763	89,89
1520	76193	90,40
1710	74827	88,78
1900	75561	89,65
2090	76393	90,64
2280	75738	89,86
2470	75957	90,12
2660	75776	89,91
2850	76543	90,82
3040	75941	90,10
3230	75458	89,53

AEMEA 11.6 sccm N2		
Time of meas.	**H_2 conc. in ppm**	**F.E. H_2**
0	155	0,59
190	130	0,66
380	17394	106,40
570	43084	263,54
760	50124	306,61
950	53415	326,74
1140	53530	327,44
1330	54390	332,70
1520	53298	326,02
1710	51014	312,05
1900	45313	277,18
2090	38458	235,25
2280	32368	197,99
2470	19355	118,39
2660	9436	57,72
2850	4702	28,76
3040	2377	14,54
3230	1349	8,25

Table 7 shows the concentrations and Faradaic efficiencies of hydrogen in the anode outlet stream. The high ppm concentrations as well the Faradaic efficiencies show that the system is basically only performing hydrogen evolution and then transporting all product to the anode as expected. The extreme F.E.'s over 100% in the AEMEA case can be explained by the nature of how the GC calculates the amount of gas measured. This is done by a calibration curve from different bottles with concentrations of products between 10 and 1000 ppm. Since in this experiment values over 50000 ppm were obtained, it is likely that the calibration does not hold for that regime. Aside of that, other researchers who were more familiar with the GC system recognised that this occurs more extremely at low currents and high concentrations. Regardless of the exact numbers, this Table explains why the initial cathodic gas GC measurements almost showed no product.

4.3 Additional experiments

Due to the results found in the previous sections, it was important to momentarily change the direction of the research towards finding out what facilitated the enormous product crossover of hydrogen to the anode compartment. Two main questions arose and two experiments were designed to give an answer:

- Why is the concentration of hydrogen so much higher than the expected production of CO?
- What is the cause for the amount of product crossover from cathode products to the anode outlet, despite the use of a membrane?

A blank experiment was performed without active cathode catalyst or membrane, so without the Ag-mesh and BPM, to see if the cathode/GDE sample holder, is able to catalyse the HER by itself to such an extent. The cathode/GDE sample holder is made out of titanium and initially it was believed this material would be either inactive or self-passivating through the formation of a titanium dioxide (TiO_2) layer.

A second experiment would build a ‘business as usual’ approach of the BPMEA system, but instead of using the BPM cut to the size of the cathode/GDE sample holder (40 x 44 mm), a BPM would be cut to the size of the entire cell (46 x 95 mm). Since the big BPM would not be able to fit in the sample holder it switches places with the sample holder frame and compressed between a rubber gasket and the solid Ti cathode. This is done to assure that no gaseous products could make their way around the edges of the membrane in a similar fashion to the liquid that was able to seep through the edges of the Sigracet GDL.

Further discussion of the following results will be addressed in chapter 5.

4.3.1. Blank experiment

The factory conditions of the purchased ElectroCell were tested in a blank experiment containing a BPM, which yielded a 6 mA current. This was before knowing about the crossover or hydrogen evolution, and therefore it was assumed that the influence of the Ti cathode/GDE sample holder was minimal. Unfortunately, this data was accidentally overwritten, thus a new blank was required when the aforementioned problems came up. Instead of using the BPM, the main interest of this blank was to see whether the cathode/GDE was able to perform hydrogen evolution. To effectively perform this experiment the cathode/GDE only consisted of the sample holder, inner silicon spacer, GDL and the sample holder closing frame. Although the majority of the cathode/GDE was blocked by the rubber gaskets around it (except for the 10 cm^2 sample area). This composition allowed the applied voltage of 2.5 V to freely perform the HER. Just for consistency, the cathode gas compartment was still flushed with a 12.0 sccm CO_2 flow which lead to the GC. Fig. 35 depicts the chronoamperometry of the blank and Table 8 shows the H_2 concentrations measured by the anodic GC measurement as well as the Faradaic efficiency calculations.

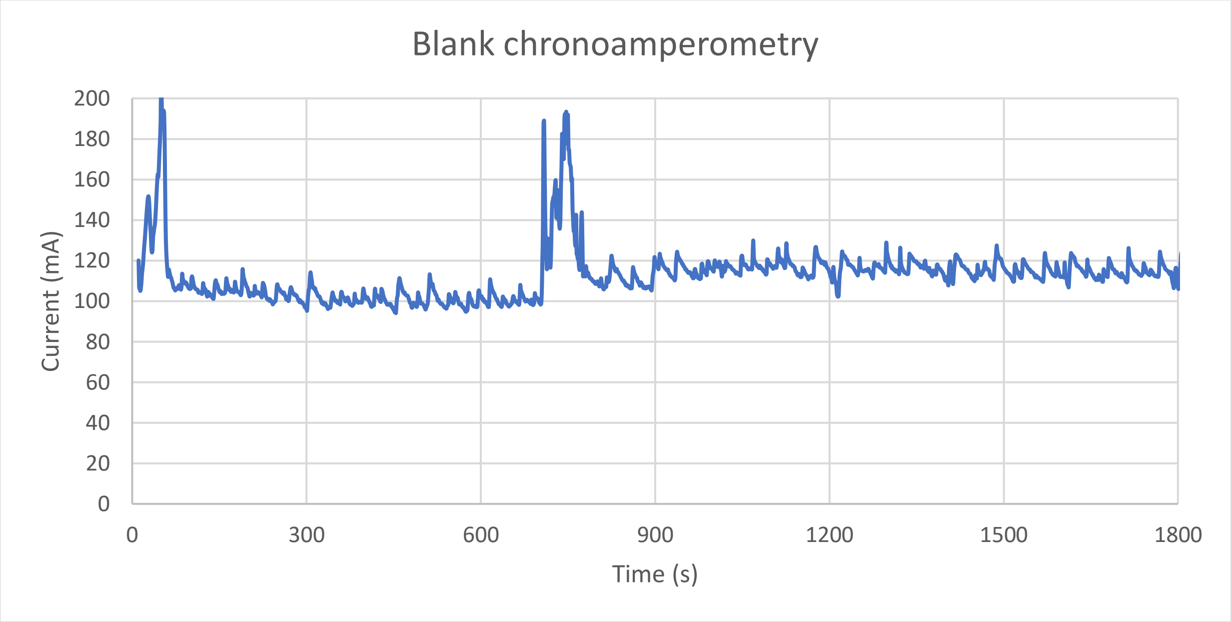

Figure 35 Chronoamperometry of the blank sample. At a potential of 2.5 V the produced current is stable around 100 to 110 mA. The fluctuations in current 700 s into the experiment are caused by pressure release due to the temporary disconnection of the GC. This result shows that the cathode/GDE sample holder is accountable for parasitically consuming a large fraction of the electrons meant for the Ag catalyst.

Table 8 Anodic GC measurement of the blank. Quantities of hydrogen exceed the calibration limit, causing Faradaic efficiencies to go over 100 %. As can be seen in fig. 35 the current during the GC measurement taken around 760 s was much higher (180 mA) than the average current of 110 mA. This caused the hydrogen concentration to momentarily spike to 200,000 ppm and the faradaic efficiency to even double the theoretical 100 % limit.

Time of meas.	H2 conc. in ppm	Faradaic Efficiency
0	262	0,27
190	39046	40,44
380	107571	111,42
570	98116	101,63
760	202155	209,40
950	77369	80,14
1140	114555	118,66
1330	115276	119,41
1520	107189	111,03
1710	104620	108,37

Another result from this blank was that small amounts of CO were detected as well, as is shown in fig. 36. During this experiment the GC gave an error for the CO calibration, making it unable to perform any analysis on these peaks. It is estimated these peaks had a faradaic efficiency of 1-5 % according to previous experiments with similar peak sizes.

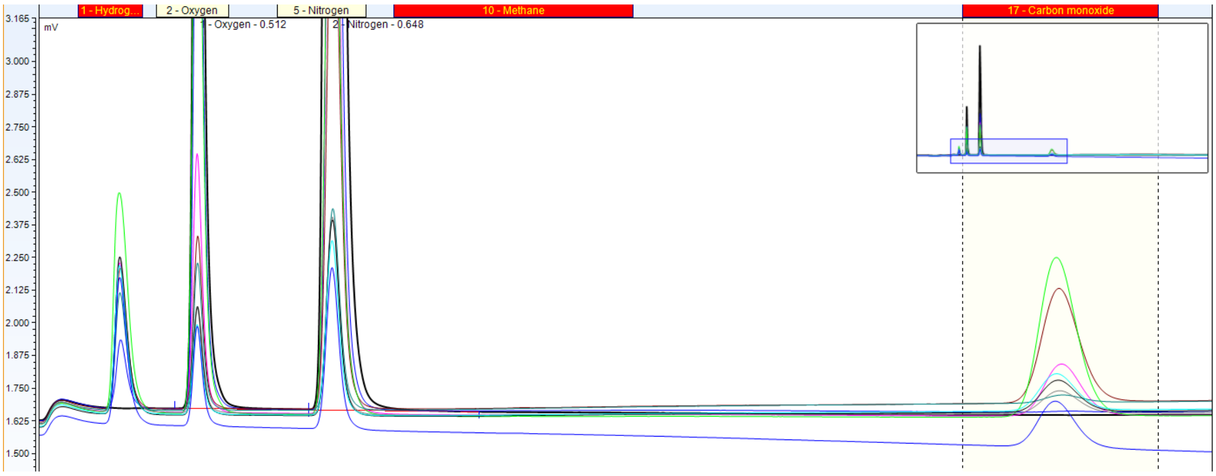

Figure 36 Screenshot of the GC TCD-2 channel during the blank experiment. As can be seen on the right hand side, small amounts of CO were formed. Due to a malfunction of the calibration these values could not be integrated and converted into Faradaic efficiencies. The size of the hydrogen peaks on the far left is not comparable to CO/do not represent the quantity of H_2, since H_2 has a much smaller response height in TCD-2 than CO. H_2 data is therefore obtained from TCD-3.

4.3.2 Big BPM

The second additional experiment using a big BPM in the BPMEA setup, as described in section 4.3, yielded the results shown in fig. 37 and Table 9. The gas compartment was flushed with 12.0 sccm CO_2. It was anticipated that by building the setup with the big BPM, the sample holder end frame would have to be placed between the BPM and the Ag-mesh. This distance of ± 1 mm caused the cell to have very poor conductive properties in the area between the BPM and catalyst, resulting in marginal currents. No cathode products were measured at the anode.

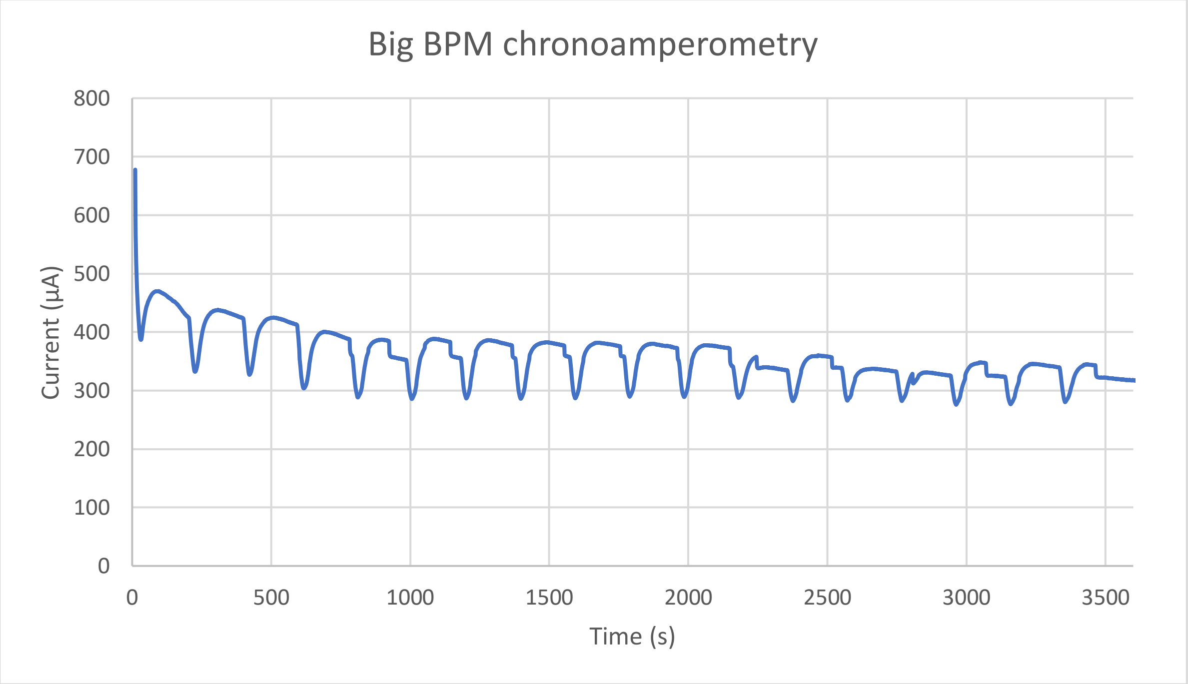

Figure 37 Chronoamperometry of the big BPM experiment . Note that the y-axis is in µA. The low currents indicated that the application of the spaced big membrane lead to a deprivation of electrolyte near the cathode thus the ability for many reactions to occur. The drops in current every 190 s interval are caused by the pressure drop from GC sampling.

Table 9 Cathodic GC measurements for the big BPM experiment. Due to the low current present, only CO could be detected in the gas phase, while H_2 was blurred away in the background. CO could be used along the µA current to determine Faradaic efficiencies, which seem to be stable around 7%.

Time of meas.	CO in ppm	Faradaic Efficiency
0	32	10,80
190	14	6,75
380	16	7,71
570	14	6,75
760	14	6,75
950	15	7,23
1140	14	6,75
1330	14	6,75
1520	13	6,27
1710	14	6,75
1900	14	6,75
2090	13	6,27
2280	15	7,23
2470	13	6,27
2660	15	7,23
2850	15	7,23
3040	15	7,23
3230	13	6,27

4.4 Ionomer BPMEA preparation

The previous experiments granted some clarity over what occurred in the cell. There was some time left to prepare for the final experiment: the ionomer BPMEA system. The goal of applying a cationic ionomer solution to the membrane + Ag-mesh was to increase proton conductivity between the membrane, the Ag-mesh catalyst and the CO_2 steam. The sPEEK-ionomer solution had no manual and no application method of it was found online. Spin-coating is an attractive way of producing a uniform layer, however no knowledge on optimized parameters was available. It was therefore required to find the best spin-coating method before applying ionomer to the expensive Ag catalyst. To practice the spin-coating of ionomer a roll of stainless steel mesh with similar physical parameters was obtained (same mesh size and wire thickness as the Ag-mesh). To determine the right parameters the following experiments were performed. Before the starting with ionomer application, SEM training was first undertaken. Then SEM images of both sides of the Sigracet 39BC were taken to gain experience with operating the SEM. These images can be found in Appendix B.

First 30 x 34 mm samples were cut and arbitrary amounts of ionomer were weighed and different spin-coating settings were applied on a plastic sample holder (no membrane). After drying SEM images were taken. The best methods found here were transferred to the second selection step where similar stainless steel samples were cut and taped against the BPM before weighing and applying ionomer. After SEM images of these samples the final selection was made using less ionomer solution and a post-treatment with water and ethanol to reduce the surface coverage of ionomer. The best method of the final selection was taken and transferred to be used on the Ag-mesh. The following results were found for all stages, including details of the recipes and SEM images of the samples.

4.4.1 Ionomer on stainless steel

The first ionomer experiments were performed on cleaned stainless steel in a sample holder. After applying the ionomer and spin-coating 8 samples according to Table 10, the samples were left to dry.

Table 10 Spin-coating recipes for the application of ionomer to the first 8 stainless steel samples. Arbitrary values for the parameters are chosen to map a variety of samples as a first approach.

Sample	Ionomer mass (g)	Rotational speed (RPM)	Duration (min)
# 1	0.27	4000	2
# 2	0.23	6000	1
# 3	0.47	6000	1
# 4	0.52	6000	5
# 5	0.25	6000	2
# 6	0.62	6000	2
# 7	0.47	9000	1
# 8	0.46	4000	5

After the samples were dried SEM images were taken of small segments of each sample, prepared as shown in fig. 38.

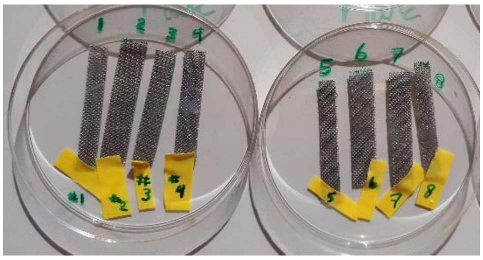

Figure 38 Prepared stainless steel + ionomer samples for SEM imaging

The SEM images are shown in fig. 39 on the next page. As can be seen from the SEM images a variety of samples was produced. While selecting an adequate spin-coating technique there were two main requirements applied to the SEM images. The sample needed to have a consistent pattern, so no aberrations. The second requirement was the availability of many three phase regions that connected ionomer (black) and uncovered stainless steel (grey).

Samples #7 and #8 used extreme rotational speed and duration, respectively, and resulted in inconsistent patterns. Sample #4 also used a long rotation time, but ended up with a uniform thick layer of ionomer covering the entire steel mesh. Samples #3 and #6 used increased amounts of ionomer, also resulting in full coverage of the surface. Sample #2 used less ionomer and has a homogeneous thin layer of ionomer over the entire mesh, without filling the mesh pores. Despite the uniform coverage, sample #2 did not show the availability of three phase regions.

The two remaining samples, #1 and #5 used similar ionomer quantities and spin-coating durations. These samples both show a consistent pattern as well as the availability of three phase regions. The recipes for these samples are therefore taken as a starting point for the next experiments. A noticeable thing is that samples #1, #2 and #5 used the lowest loading of ionomer, and therefore it is considered even less loading might result in better samples.

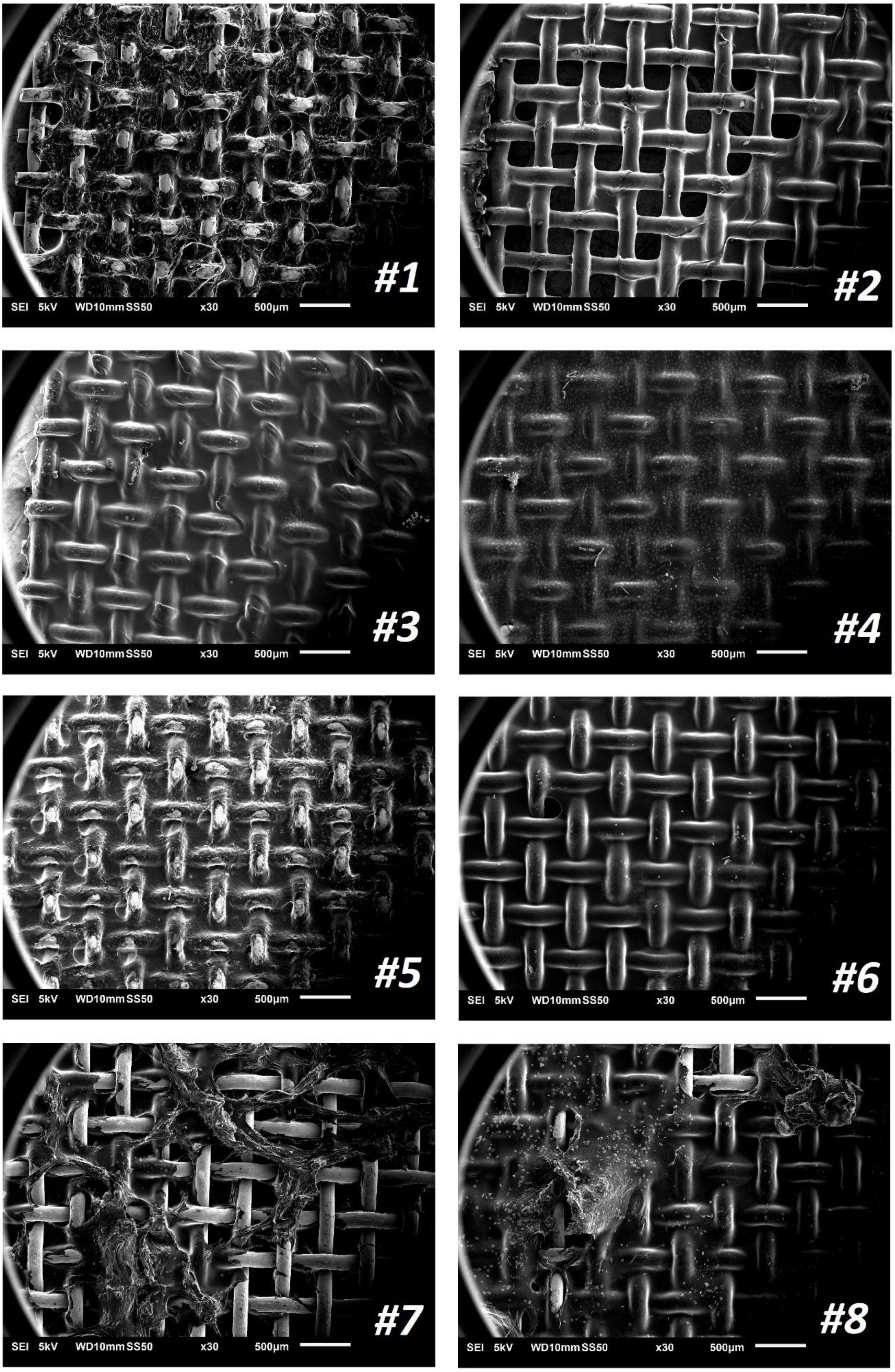

Figure 39 SEM images of the spin-coated samples described in Table 10. All images are taken at a magnification of x30. The stainless steel mesh is shown in grey, while the ionomer solution is shown in black. Samples 1 and 5 have the desired morphology.

4.4.2 Ionomer on BPM and stainless steel

The second selection was done by applying ionomer stainless steel mesh taped to a BPM. With this method 4 samples were produced according to the recipes in Table 11.

Table 11. Preparation methods for the application of ionomer to stainless steel on a BPM.

Sample	Ionomer mass (g)	Rotational speed (RPM)	Duration (min)
# 1	0.32	6000	1
# 2	0.30	6000	1
# 3	0.26	6000	2
# 4	0.22	6000	2

Due to the watery nature of the membrane and the need to be stored in a liquid to prevent structural damage, the ionomer solutions immediately gave a visual whitening after application and immersion in water as shown below (fig. 40):

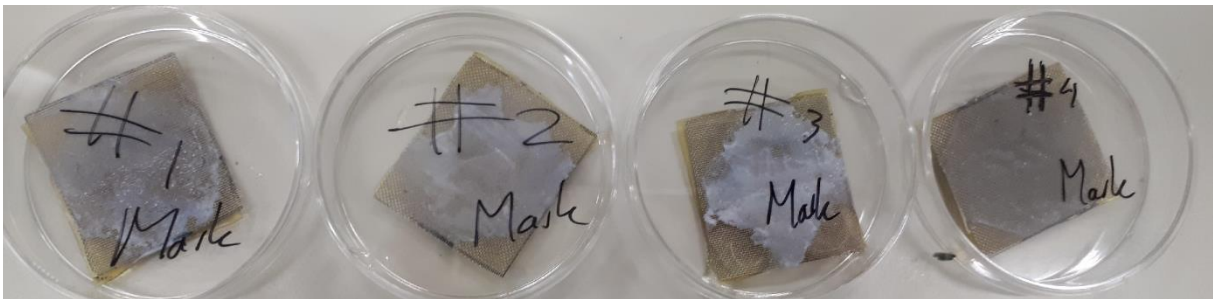

Figure 40. Visual whitening of the ionomer solution after immersion in water. Sample #4, which has the lowest ionomer loading, shows the smallest visual alteration.

Although these samples did not look very promising, the SEM images in fig. 41 were taken nonetheless.

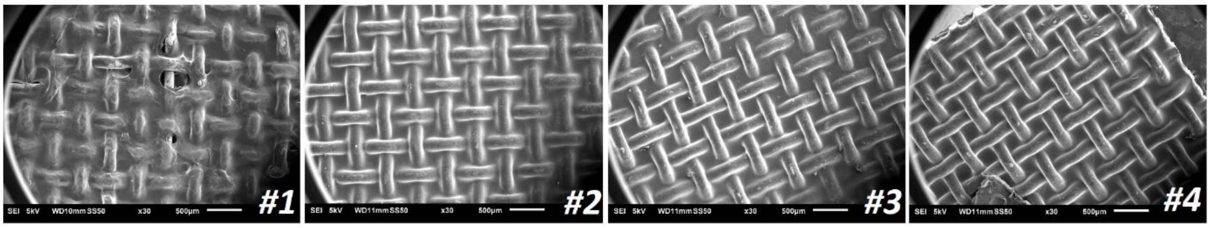

Figure 41 SEM images of the BPM + stainless steel + ionomer samples. All samples shown full coverage of the surface. Sample #1 shows minor defects and inconsistencies, the others show total coverage by ionomer.

As can be seen from fig. 41 none of the samples made with this method seem useful for the desired purpose. This shows that the method used for ‘dry’ stainless steel samples is not 1 to 1 transferable to the stainless steel + BPM case. This lead to a final test of stainless steel samples, in which again a more arbitrary approach was taken.

4.4.3 Ionomer on BPM and stainless steel with additional processing

In this final try to produce a repetitive heterogeneous layer of ionomer on top of the stainless steel + BPM 4 samples were made with the knowledge of the previous samples. One of the ideas to improve the heterogeneity of the surface was applying ethanol to the top layer to thin/remove some of the ionomer after spin-coating (Samples #1 and #2) and another was to scrape off as much ionomer as possible before spin-coating (Samples #3 and #4). All samples are put in water afterwards to stabilize the BPM. The recipes are shown in Table 12. The SEM images of these samples are shown in fig. 42.

Table 12 Final ionomer + stainless steel + BPM samples. Samples #1 and #2 are treated with ethanol after spin-coating. Samples #3 and #4 scraped off as much ionomer from the surface after application (hence the low loading).

Sample	Ionomer mass (g)	Rotational speed (RPM)	Duration (min)
# 1	0.36	6000	1
# 2	0.42	6000	2
# 3	0.24	6000	2
# 4	0.20	6000	1

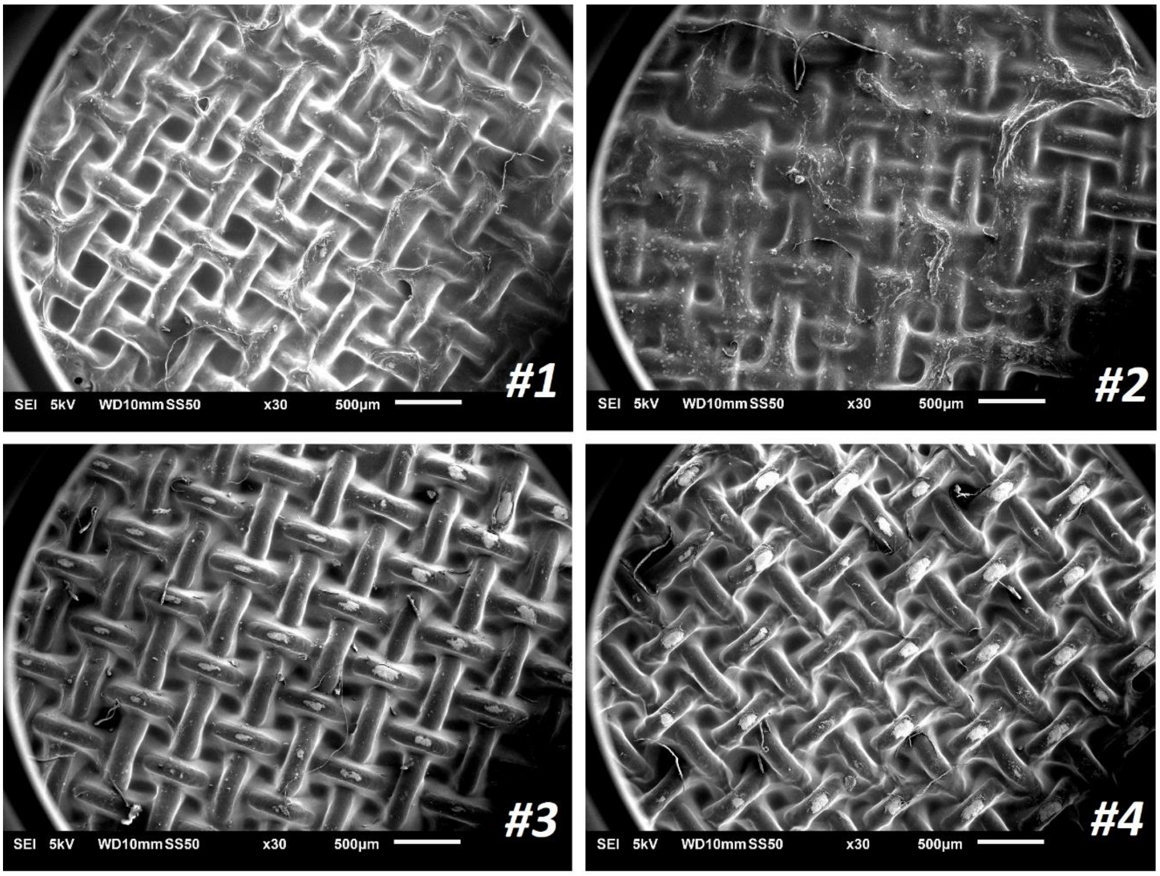

Figure 42 SEM images of the final ionomer + stainless steel + BPM. Samples #1 and #2 show irregularities. Samples #3 and #4 are almost uniform, but do show the heterogeneity of the surface.

From these SEM images it was determined that the ethanol application to the top (#1 and #2) resulted in too many irregularities. Scraping off the ionomer solution as done to sample #3 and #4 showed to be an effective way of giving way to relatively uniform three phase regions.

4.5 Chronoamperometry of the ionomer BPMEA

After determining the best method of ionomer application to the stainless steel mesh, it was time to transfer the best spin-coating method to the Ag-mesh. Since it was also found that titanium cathode/GDE sample holder had a high HER activity, it was decided to apply the Ag-mesh directly to the big BPM, as was used in section 4.3.2. The previous use of the big BPM was not effective, producing only sub-mA currents. Since this was attributed to the distance between the membrane and the Ag catalyst, it is expected that when the BPM and Ag-mesh are 'glued' together much higher currents can be achieved. The application method of ionomer was as follows:

Edges of the membrane were taped tight against a flat surface. The Ag-mesh was put in the centre of the big BPM and edges of the mesh were taped to the BPM. 0.20 g of ionomer was applied and spread using a flat-end spatula. The top was scraped off vigorously, since that gave the best results in the most similar situation regarding stainless steel. The sample is then spin-coated for 1 minute at 6000 RPM. A final rinsing of water was done before storing the ionomer BPMEA in the membrane container. The ionomer BPMEA is shown in fig. 43.

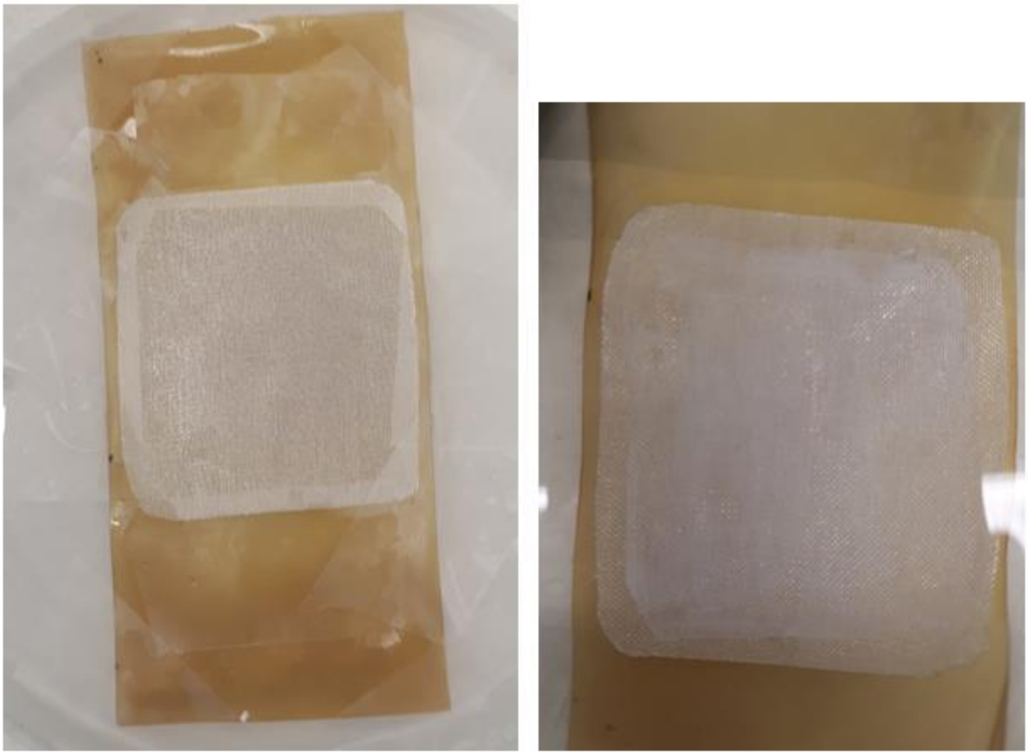

Figure 43 Left: taped Ag-mesh on immobile BPM. Right: finished ionomer BPMEA system with a thin, scraped layer of ionomer.

When the 1 hour chronoamperometry at 2.5 V_{cell} on this sample was performed the GC was out of order, thus no product measurements were taken. The results of doing the experiment was, however, surprising. In fig. 44 the chronoamperometry is shown. On the left of the graph the first 20 seconds are shown separately, since these values drowned out the majority of the measurement. Before starting the experiment the cell is flushed with 1M KOH on the anode side, and 12.6 sccm CO_2 on the anode side. The membrane already provides the Ag-mesh with an initial proton concentration, as well as possible reactive contaminants from the ionomer solution. This causes the current to spike up to 650 mA at the start of the experiment, but rapidly diminish to 50 mA over the first 100 s. After the initial overexpression the system recovers slightly and shows a standard curve for degradation over time.

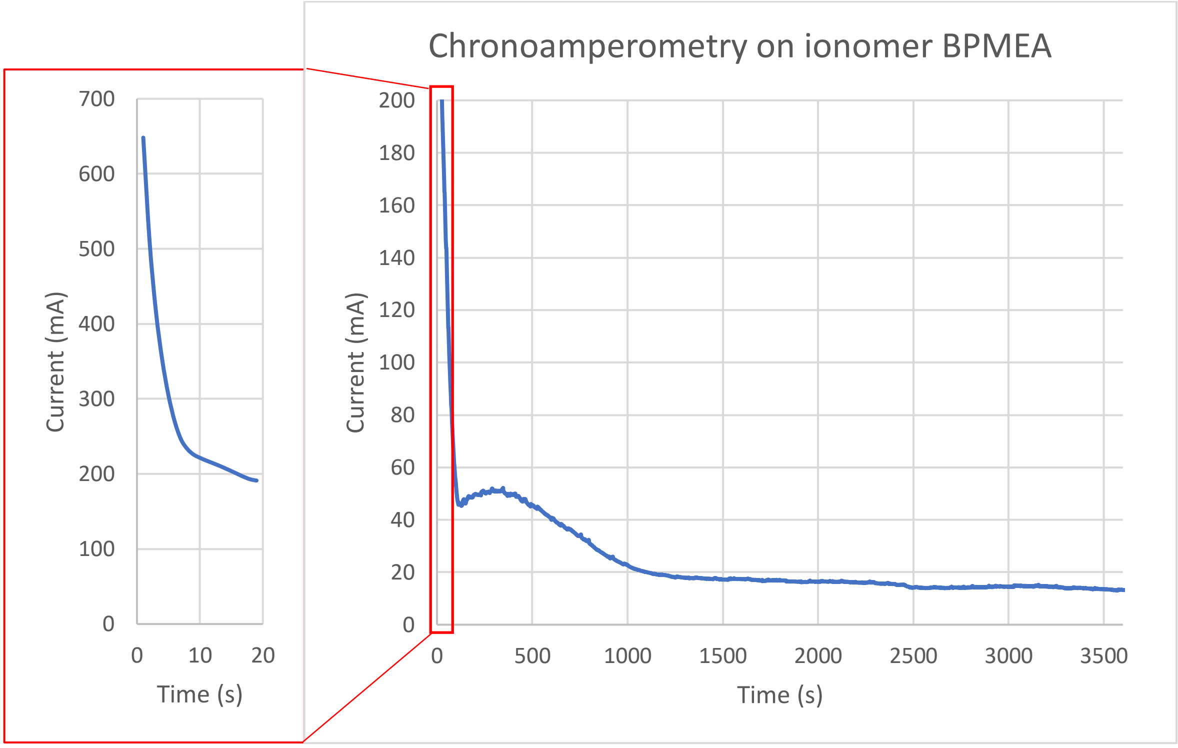

Figure 44. Chronoamperometry of the ionomer BPMEA system. On the left the first 20 s of the measurement are shown. A peak of 650 mA occurs as the experiment is started, but this value reduced quickly to 50 mA in the first 100 seconds of reaction. After a 1000 s the current slowly degrades from 20 mA to 13 mA over the rest of the experiment.

This experiment shows that the ionomer BPMEA configuration is able to produce a high current, but only briefly before degrading. The anode side of the BPM after reaction (fig. 45) indicates that the BPM got deformed during operation, while the ionomer side of the Ag-mesh remains intact.

Figure 45 The ionomer BPMEA configuration after 1 h chronoamperometry. Extreme bubble formation on the anode side of the membrane is found, while the cathode side only shows no irregularities, aside of some carbon paper stuck to the Ag-mesh.

After the experiment the ionomer BPMEA was kept in water for a day to maintain the structure of the BPM before taking SEM images. During the interval between the experiment and performing SEM the ionomer BPMEA visually changed even further, as can be seen in fig. 46.

Figure 46 The ionomer BPMEA configuration after 1 day in water. On the left the partially delaminated bipolar membrane turned black at the interface region. On the right a brownish colour appeared where the ionomer was applied, the taped off edges do not show this colour change.

It is not certain what the black substance on the interface layer is nor what the brownish substance on the ionomer solution is. To gain more knowledge about the structure SEM images are taken of the intact BPM area, the delaminated AEM layer of the membrane interface, the delaminated CEM layer of the membrane interface and the top of the ionomer-Ag-mesh interface (fig. 47).

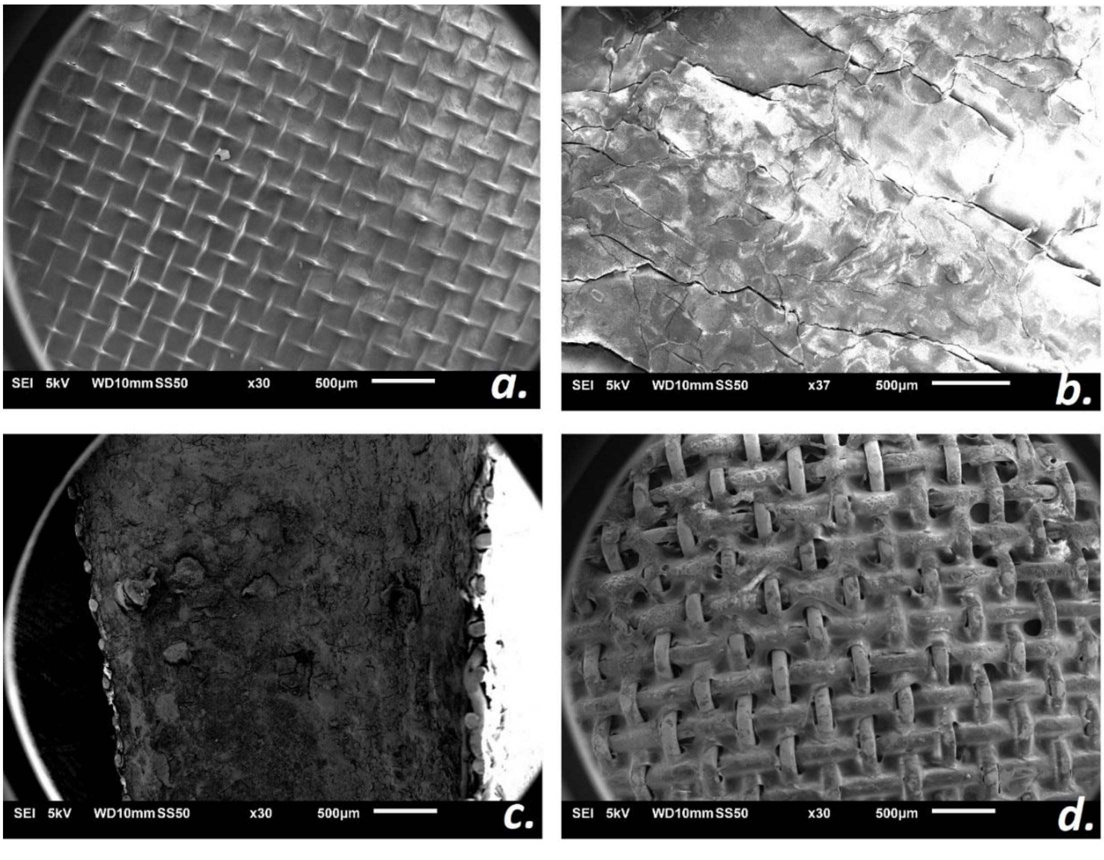

Figure 47 SEM images of the ionomer BPMEA 1 day after experiments. a. intact BPM, b. delaminated AEM of the BPM interface, c. delaminated CEM of the BPM interface, d. Ag-mesh with ionomer as produced through spin-coating.

As can be seen from fig. 47a, the BPM seems intact seen from the AEM side. Despite of this, the delamination at the AEM-CEM interface (shown in 47b-c) displays ruptures and defects, which introduced the black material to be deposited mainly on the CEM layer. This only happened after operation since fig. 45 did not show this black material. It is possible that the carbon paper shown on edge of the ionomer side in fig. 45 dissolved and relocated into the CEM-AEM layer, since the same carbon paper is much less visible a day later in fig. 46. As for fig. 47d, although it is uncertain whether the Ag-mesh with ionomer structure was altered due to the reaction, the application of ionomer seems to have been performed as desired, since a repetitive heterogeneous layer of combined ionomer, Ag-mesh and access to the gas phase is visible. The adhesion of the ionomer to the CEM appeared to be intact as well.

4.6 Alternative approach: Gas diffusion electrode

No stable CO selective setup has been produced this far while using the Ag-mesh as a catalyst. Although it is likely the Ag-mesh is capable of producing CO, the physical restrains from using three separate layers prevented this reaction from occurring to an effective quantity. To show that the EC MFC cell is able to provide a stable current without using the cathode/GDE sample holder a final experiment was set up. Prior to the ionomer BPMEA experiment, an attempt was made to produce a big BPM – Ag-mesh – GDL system between two rubber gaskets. Due to the non-cohesion between the three layers a leak-proof system could not be achieved. As an alternative approach a final experiment more in-line with the current development of gas utilizing electrodes was set up. Instead of using a MEA the Ag-mesh was removed and a thin 100 nm layer of silver was sputtered on top of the microporous layer of the Sigracet 39BC, thereby effectively creating a gas diffusion electrode (GDE). The sputtered Ag GDE is shown in fig. 47.

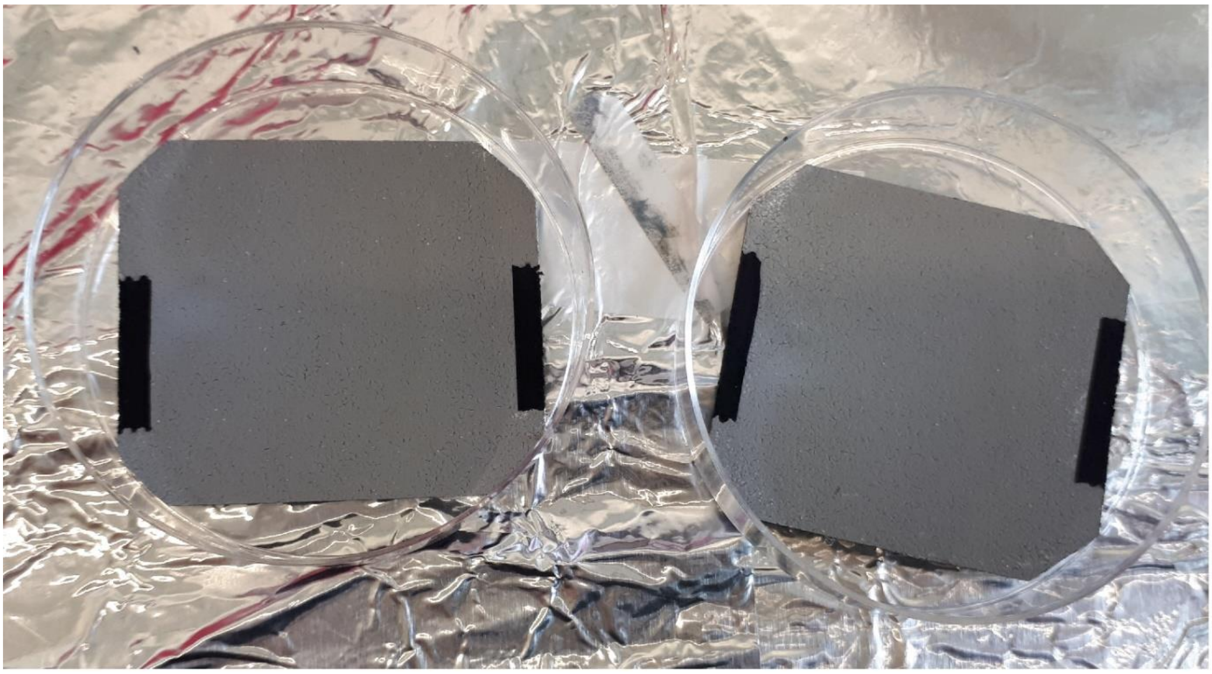

Figure 48 Ag sputtered on the microporous layer of the GDL. The edges of the MPL were taped against the sputter sample holder and therefore the MPL underneath is still visible. The size of the samples is 5 mm larger on all sides in comparison to the 10 cm^2 rubber gasket opening on the gas side.

The GDE was pressed against the big BPM and an electrical connection was made via the backside of the GDL using copper tape. During the chronoamperometry experiment the GC was operational for the first 30 minutes, but during this time TCD-3 did not function properly, making it hard to identify H_2 accurately. After 30 minutes a continuous increase in overpressure was noted on the mass flow controller. Normally this value should stay between 100 and 200 mbar overpressure, yet this time the pressure exceeded to over 500 mbar. When this was noted the GC measurement was stopped but the 1h chronoamperometry was continued and repeated twice afterwards, since a stable current was not reached yet. The chronoamperometries are shown in fig. 48. During the first two measurements the current steadily increased to a value of 95 mA where it started to level off. A short period of time was present between the second and third measurement, after which the third experiment showed a gradual decrease in activity.

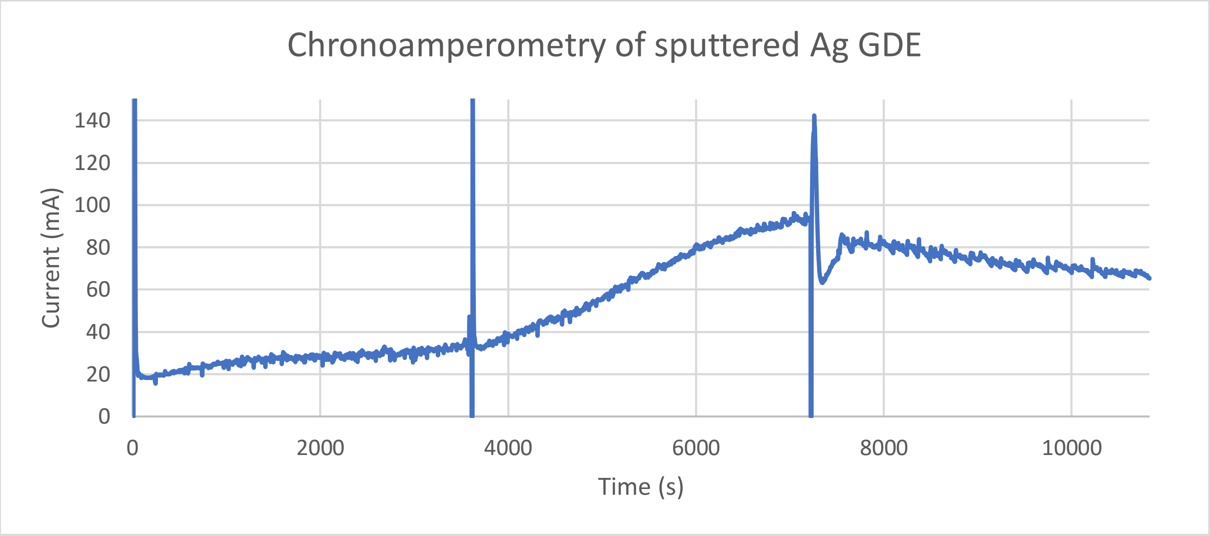

Figure 49 Chronoamperometry of the sputtered Ag GDE over 3 hours. The current produced by the GDE initially is lower than expected. Over time the current increases to 35 mA during the first measurement. Immediately after the first 3600 s experiment a second experiment is started (indicated by the first spike). During the second measurement the current started where the first experiment ended, but then increased to 95 mA. The third measurement was started a minute after the second experiment started and shows a dampened decrease in current from 85 to 65 mA over its duration.

The increase in current during the first two experiments is likely to be correlated to the big BPM experiment, where the catalyst and membrane were not in direct contact. Although partial direct contact is established between the BPM and the GDE, the conductivity of protons in the interface is low at the start. It is speculated that during the course of the first two hours the interfacial layer becomes more humidified, resulting in a more effective transport of protons to the active catalyst. During the third hour of this experiment is it considered that either the sputtered Ag on the GDL becomes less stable, or that the hydrophobic nature of the GDL becomes compromised. In Table 13 the first 30 minutes of the GC measurements are shown. Note that the GC was malfunctioning and these values are likely incorrect, but do display that some CO is produced in this system.

Table 13 Cathodic GC measurement of a sputtered Ag GDE. during the first 30 minutes of the experiment. The first two measurements are blanks taken before the potentiostat was turned on. Due to a malfunction in the GC the H_2 data was taken from the less accurate TCD-2 instead of TCD-3. A fraction of the current is measured as CO product in the gas phase.

Time of meas.	**H_2 in ppm**	**Faradaic Efficiency**		**Time of meas.**	**CO in ppm**	**Faradaic Efficiency**
0	n.a.	n.a.		0	n.a.	n.a.
190	n.a.	n.a.		190	n.a.	n.a
380	388	2,92		380	95	0,72
570	776	5,58		570	160	1,15
760	768	5,28		760	130	0,89
950	693	4,57		950	112	0,74
1140	694	4,39		1140	95	0,60
1330	722	4,39		1330	88	0,54
1520	739	4,50		1520	74	0,45
1710	790	4,81		1710	59	0,36
1900	923	5,41		1900	102	0,60

5. Discussion

The goal of this research was to build and test three different MEA configurations in a flow cell system. To compare these configurations the following research questions were developed, while keeping in mind three base factors of cell performance: activity, selectivity and stability.

- Which of the tested MEA setups provides the highest current at a fixed cell potential?
- What are the effects of altering different components in an MEA setup in terms of reaction selectivity and stability?
- How does the bipolar membrane impact the current density in respect to the anion exchange membrane?

The first question directly relates to the activity of the system as a whole and can be answered by simply comparing the chronoamperometry data for the different systems. This information on its own, however, does not tell us which configuration is best suited for the application, since high activity is not always accompanied by stable operation or product selectivity. To this end, the second question was designed to support the first question by taking a look at both stability over a 1-hour period and selectivity through product identification. The third question acted as a control addressing the impact of the membrane between the BPMEA and the AEMEA systems.

The first goal was identifying a method to compare each of the different systems, without creating a bias for a system that works better under the set circumstances. It was chosen to set the potential to a value at which the BPMEA setup, being the main comparison standard, would produce a current of about 100 mA. During the first CVs it was found that at a potential of 2.5V would suffice to obtain the target current in the BPMEA system.

When the set potential of 2.5 V was used to compare the activity (and stability) of the BPMEA and AEMEA in a chronoamperometry it was found that the activity of the BPMEA was 4 to 6 times higher than under identical circumstances (BPMEA: 90-140 mA – AEMEA: 20-25 mA). This indicates that the use of a BPM is more beneficial to the activity than the AEMEA, regardless of whether the CO_2RR or the HER was performed. Since both the CO_2RR and the HER require protons for their reaction to take place, their activities are both directly linked to the local proton concentration near the cathode. In case of the AEMEA the AEM allows unhindered transport of hydroxyls, resulting in only a minor OH^- gradient between the cathode, where hydroxyls are formed, and the bulk, which consists of 1M KOH. This results in both the CO_2RR and HER having to perform a proton dependent reaction in a proton deprived (pH 14) region. As a result, the reaction can only occur if a proton can be directly obtained from H_2O dissociation near the cathode active area, which requires additional potential, thus increasing the onset potential. In the case of the BPMEA the proton saturated CEM layer (internal pH 0) of the BPM was directed towards the cathode. Since the cathode reactions produce OH^- and/or consume H^+ it is not certain what the exact local pH near the cathode is. Despite this uncertainty, the increase in current for the BPMEA vs the AEMEA at a fixed potential implies that the BPM causes a significant increase in local proton concentration near the cathode, which benefits both cathodic reactions at 2.5 V. Increasing the fixed potential will have a positive effect on the activity but will also influence the selectivity of the reaction. In other studies, it was found that the optimal Faradaic efficiency towards CO (90%) was achieved in the range of 1 to 1.2 V vs RHE for Ag gas diffusion electrodes [70]. It might be interesting for future experiments to operate in this region when utilizing a gas diffusion electrode.

One possible consequence of the low pH environment resulting from the use of a BPMEA rather than an AEMEA, is that an extremely low pH near the cathode would benefit the HER more than the CO_2RR, thus reducing the selectivity towards CO. To this end, and to answer the second research question, GC measurements were taken during the experiments.

When the cathodic GC measurements were studied for the BPMEA, only a fraction of all current could be accounted for in terms of H_2, but no CO was detected. The AEMEA showed similar H_2 concentrations at much lower currents (indicating higher Faradaic efficiencies), but unlike the BPMEA case small quantities (<1%) of CO were detected. Although this partially confirms the hypothesis of higher product selectivities towards CO in a locally alkaline environment, the quantities of Faradaic efficiencies and measured concentrations were too low to be conclusive. The results of the cathodic GC measurements combined with the found currents implied that most products formed on the cathode were escaping from the cell elsewhere.

When the anodic GC measurements for the AEMEA and BPMEA were taken, it was not only found that in both cases almost exclusively hydrogen was produced, instead of CO, but that almost all cathode products crossed over to the anode compartment. Looking deeper into this issue it was found in a blank control measurement of the system that the cathode/GDE, made of titanium, accounted for nearly all of the cathode current in the form of exclusively hydrogen. Thus, any products which may have been created on the Ag-mesh would be masked by hydrogen evolution on titanium.

When the research was started it was assumed titanium could not produce hydrogen to such an extent due to passivation after forming a TiO_2 layer at low potentials. Another study showed that although the activity for titanium towards the HER is lower than that of other metals like nickel, activities that explain the found current can be obtained from pure titanium in a 1M KOH solution [71]. Interestingly enough, the use of a BPM instead of an AEM did have a positive effect on the current, despite the electrolyte being in direct contact with the cathode/GDE sample holder without having to pass the membrane. This indicated that the HER did happen somewhere near the membrane (at least in the BPMEA), otherwise the observed difference in current between the BPMEA and AEMEA would not have been visible. It is likely that the previously mentioned local pH effect caused by the BPM is the main driver for this change in activity.

The extreme cathodic product crossover found through the cathode and anode GC measurements indicated that the products were much more likely to traverse the cell to the cathode rather than move to the gas phase. This issue brought up two main concerns:

First, the reaction occurred **near** the GDL but not **on** the GDL. The distance between the reactive surface, which turned out to be the titanium sample holder, and the GDL caused the products to form bubbles in the liquid phase instead of diffusion directly to the GDL and being taken up by the gas phase. It is likely that the CO_2RR is still limited by the lack of available CO_2 near the Ag catalyst, due to the low solubility and diffusivity of CO_2 in the electrolyte.

Second, the mentioned formation of product in the liquid electrolyte had no incentive to travel towards the GDL and accumulated until a bubble was formed. The bubble would travel upwards along the Ag-mesh until the top of the sample holder was met, where it got stuck between the sample holder and the BPM – Ag-mesh – GDL components. As could be seen from the BPMEA configuration (fig. 28), the separate components were manually cut to the size of the cathode/GDE sample holder. It is believed that, due to human error, some layers did not connect perfectly along the edges of the sample holder, despite being leak proof towards the gas phase. This allowed the gas products accumulated in the top of the BPMEA to slip past the BPM and be taken away by the flowing electrolyte to the anolyte compartment, where the gas and liquid phases separated.

In order to put this hypothesis to the test and prevent crossover the Big BPM experiment was performed. It was found that product crossover could be avoided at which point some CO was detected at the cathode, opposing the results found in the initial BPMEA case. The downside, however, was that only currents below 1 mA were obtained, two orders of magnitude less than the original BPMEA case. It is believed that in the Big BPM case there was an increased spatial distance between the BPM and either active component in the cathode/GDE (either titanium or Ag-mesh). This caused the cathode side of the BPM to contain a marginal amount of liquid, thus reducing the proton transport near the cathode to near-zero. In retrospect, it would have been beneficial to introduce a cathodic electrolyte (e.g. bicarbonate) to the cathode compartment to increase ionic and electrical conductivity.

Some attempts were made to revise the initial BPMEA and AEMEA experiments while excluding the titanium cathode/GDE sample holder to determine the exact activity and selectivity of the Ag-mesh. It was deemed not possible to make a leakproof system of three individual layers between two gaskets.

It was decided to move forward to experimenting with the ionomer solution to see if this would have a beneficial effect on the system. After a long series of practicing with ionomer spin-coating on stainless steel, the best application method was transferred to the Ag-mesh on a BPM with similar dimensions as used in the Big BPM experiment. As a first pleasant surprise it was found that the immobilisation of the Ag-mesh on the BPM caused the ionomer BPMEA system to be leakproof between two gaskets. When this sample was tested at 2.5 V it showed an unprecedented current peak of 650 mA (65 mA/cm^2) as the measurement started. This performance did not last for long as it decreased to 200 mA after 20 s, further down to 20 mA after 15 minutes. When the experiment was done and the cell was opened up the membrane was found to be permanently damaged by internal blistering and delamination at multiple locations.

A first hypothesis for this result is that bubbles formed on the Ag-mesh underneath the ionomer surface. The BPM facilitated the transport of protons from the centre of the membrane to the Ag catalyst. Instead of being transported to the three-phase region where it could interact with CO_2 to form CO, the HER was performed at the proton rich ionomer and Ag-mesh interface. While the initial concentration of protons was quickly consumed, the current was rapidly reduced as well. As the formed bubbles on the Ag-mesh accumulated, the pressure built up and the BPM was pushed away from the Ag-mesh.

According to the previously mentioned theory the ionomer should rupture at the Ag-mesh interface where H_2 is formed and thus the ionomer-Ag interface would be damaged. When SEM images were taken it was found that the top side/interface of the ionomer-Ag-mesh remained more-or-less intact and that the SCR, the interface layer of the BPM, had delaminated. Although it is uncertain what caused the delamination, two theories are proposed to have caused this effect. One theory was that the applied ionomer solution made a stronger bond than the internal structure of the BPM. If this is the case the subsurface evolution of hydrogen would penetrate through the CEM and accumulate in the SCR, leading to delamination. This theory does not seem likely since the produced ionomer layer had higher flexibility and lower physical strength than the BPM. The other theory was that the system worked exceptionally well at the start of the experiment, indicated by the extreme current. To maintain this current density a rapid flux of protons would be required from the BPM. As a result, the SCR had to dissociate H_2O into H^+ and OH^- at a highly increased rate, which could have damaged the adhesive layer or caused repelling ion concentrations to occur within the membrane.

When all planned experiments were performed there was some time left to perform an alternative approach to the problem. Instead of producing a MEA configuration with the membrane – Ag-mesh – GDL, a separate GDE was created by sputtering a 100 nm Ag layer on top of the MPL of the GDL. This integration of cathode material and GDL ensured the direct interaction of the gaseous CO_2 reagent, active Ag material and electrolyte on a nanometer scale distance. At the start of this experiment the current was 20 mA, but steadily increased to 95 mA over 2 hours. It is likely this was caused by a similar effect as seen in the Big BPM experiment; due to an initially low amount of liquid in the cathode compartment the current is limited. As the reaction progresses more liquid builds up on the cathode side of the BPM, resulting in increasing currents due to increased active areas. This was the only experiment to achieve a high current while not utilizing the titanium cathode/GDE and thus shows to be a promising method for future experiments, although much is to be learned about the exact functionality of the system.

For future research in the field of either MEA's and GDE's for the CO_2RR it is recommended to make use of (nano)powdered catalyst application methods instead of applying bulky foil or mesh-like materials to increase the activity. To assess MEA's it is of most importance to avoid product crossover and to enable electrical conductivity through a non-reactive material. Damage to the MEA can be expected though blistering and/or delamination when the active catalyst material is embedded too deeply within the membrane.

6. Conclusion

In this research three different membrane electrode assemblies were built in an electrochemical flowcell that utilized gaseous CO_2 in order to increase the activity of the CO_2 reduction. To compare the efficiency of the configurations on a systems level, a set total cell potential of 2.5 V was determined and used throughout all experiments. Although much higher currents were obtained with the BPMEA configuration in comparison to the AEMEA configuration, exclusively hydrogen was produced in both cases. The efficiency of the BPMEA over the AEMEA was attributed to the titanium sample holder performing the HER better in a more acidic environment near the bipolar membrane than near the alkaline anion exchange membrane. Despite the reduced activity, the AEMEA did show slightly higher CO formation, due to the highly alkaline environment suppressing hydrogen evolution. Experiments with a membrane – Ag-mesh – GDL configuration, while excluding the titanium sample holder, either produced low currents or were not able to form a leakproof system.

A cation ionomer solution was applied to the BPM to increase the conductivity of protons towards the active catalyst. Despite the initial excellent activity at the chosen potential, during operation the BPM rapidly blistered and delaminated due to gas accumulation within the membrane. It was found that the use of a Ag-mesh is not practical for utilizing the gaseous CO_2 stream, since the active Ag-mesh was located too far from the gas phase to communicate with gaseous CO_2 properly. In a final attempt to increase the activity for CO, Ag was sputtered directly on the GDL to produce a gas diffusion electrode and thus reduce the distance between the gas phase and the active catalyst. It was found that (without optimisation) higher currents than the MEA systems could be achieved, without the titanium sample holder. Although the results were often obscured by the extent of hydrogen evolution, making it difficult to give any concise conclusion, it is suggested that for future research a mesh-type catalyst is avoided and sprayed/sputtered catalyst nanoparticles are applied to either the membrane or gas diffusion electrode.

7. Acknowledgements

In respect to any of my previous research assignments, this research project required me to be more self-reliant in both planning and experimenting. Nevertheless, I am grateful that during the second half of my thesis some new people joined the MECS group and helped progress my work. First, I'd like to thank ir. Marijn Blommaert for his help with obtaining the ElectroCell MFC system and other materials, planning experiments and discussing their outcomes. Second, I'd like to thank my supervisors dr. ir. David Vermaas for setting up the initial research proposal and dr. Wilson Smith for motivating me and discussing progression.

I'd also like to acknowledge the following people. Post-doc Tom Burdyny for reviewing my thesis as well as providing resourceful discussion and solutions to problems met along the way. My fellow student Nitin Prasad for teaching me how to operate the GC. Our technical staff ir. Herman Schreuder and ir. Joost Middelkoop for performing the sputtering, ordering materials and helping me solve technical obstacles. The TP group for interesting weekly lunch talks, where I saw different angles on solving chemical and physical problems. Last but not least, I'd like to thank the entire MECS group for giving me a great time, for making me feel at home and for allowing me to help the newcomers to integrate within the group structure.

8. References

[1] *Graphic: The relentless rise of carbon dioxide.* NASA, [Online available at]: https://climate.nasa.gov/climate_resources/24/graphic-the-relentless-rise-of-carbon-dioxide/

[2] *Extreme Weather.* NCA, 2014, [Online available at]: https://nca2014.globalchange.gov/highlights/report-findings/extreme-weather

[3] *Kyoto Protocol to the United Nations framework convention on climate change.* United Nations, 1998, [Online available at]: https://unfccc.int/resource/docs/convkp/kpeng.pdf

[4] *The Paris Agreement Summary.* Climate Focus, 2015, [Online available at]: http://www.climatefocus.com/sites/default/files/20151228%20COP%2021%20briefing%20FIN.pdf

[5] *Research Coordination Network: What is CCUS?* American Institute of Chemical Engineers, [Online available at:] https://www.aiche.org/ccusnetwork/what-ccus

[6] *World Energy Scenarios: Composing energy futures for 2050.* World Energy Council, 2013, [Online available at:] *https://www.worldenergy.org/wp-content/uploads/2013/09/World-Energy-Scenarios_Composing-energy-futures-to-2050_Full-report.pdf*

[7] D. Schanke, E. Bergene, A. Holmen. *Fischer-tropsch synthesis.* 2001, US Patent US6211255B1.

[8] Zhang, W., Hu, Y., Ma, L., Zhu, G., Wang, Y., Xue, X., Chen, R., Yang, S., Jin, Z. *Progress and Perspective of Electrocatalylitic CO_2 Reduction for Renewable Carbonaceous Fuels and Chemicals.* Advanced Science, 2018, doi:10.1002/advs.201700275

[9] Verma, S., Kim, B., Jhong, H. , Ma, S., Kenis, P. J.. *A Gross-Margin Model for Defining Technoeconomic Benchmarks in the Electroreduction of CO2*. ChemSusChem, 2016, 9(15), 1972-1979. doi:10.1002/cssc.201600394

[10] Hara, K., Sakata, T. *Large Current Density CO_2 Reduction under High Pressure Using Gas Diffusion Electrodes*. Bulletin of the Chemical Society of Japan, 1997, 70(3), 571-576. doi:10.1246/bcsj.70.571

[11] Li, Y. C., Zhou, D., Yan, Z., Gonçalves, R. H., Salvatore, D. A., Berlinguette, C. P., & Mallouk, T. E. *Electrolysis of CO2 to Syngas in Bipolar Membrane-Based Electrochemical Cells.* ACS Energy Letters, 2016, 1(6), 1149-1153. doi:10.1021/acsenergylett.6b00475

[12] Mahmood, M. N., Masheder, D., & Harty, C. J. *Use of gas-diffusion electrodes for high-rate electrochemical reduction of carbon dioxide. I. Reduction at lead, indium- and tin-impregnated electrodes.* Journal of Applied Electrochemistry, 1987, 17(6), 1159-1170. doi:10.1007/bf01023599

[13] Ferrer, I.M., McCrory, C.C.L., Peters, J.C., Jaramillo, T.F. *Benchmarking of Heterogeneous CO_2 Reduction Reaction Electrocatalysts.* The Electrochemical Society, 2015, 8, 1755.

[14] Ma, M., Trześniewski, B. J., Xie, J., Smith, W. A. *Selective and Efficient Reduction of Carbon Dioxide to Carbon Monoxide on Oxide-Derived Nanostructured Silver Electrocatalysts.* Angewandte Chemie International Edition, 2016, 55(33), 9748-9752. doi:10.1002/anie.201604654

[15] Zhu, W., Michalsky, R., Metin, Ö, Lv, H., Guo, S., Wright, C., Sun, S. *Correction to "Monodisperse Au Nanoparticles for Selective Electrocatalytic Reduction of CO2 to CO".* Journal of the American Chemical Society, 2017, 139(27), 9408-9408. doi:10.1021/jacs.7b05685

[16] Hammer, B., Morikawa, Y., Nørskov, J. K. *CO Chemisorption at Metal Surfaces and Overlayers.* Physical Review Letters, 1996, 76(12), 2141-2144. doi:10.1103/physrevlett.76.2141

[17] Kuhl, K. P., Cave, E. R., Abram, D. N., Jaramillo, T. F. *New insights into the electrochemical reduction of carbon dioxide on metallic copper surfaces.* Energy & Environmental Science, 2012, 5(5), 7050. doi:10.1039/c2ee21234j

[18] Ma, M. *Selective Electrocatalytic CO_2 Conversion on Metal Surfaces.* TU Delft Repository, 2017. doi:10.4233/uuid:8b16b984-197d-4486-a139-02cbf9b80e69

[19] Lu, Q., Jiao, F. *Electrochemical CO_2 reduction: Electrocatalyst, reaction mechanism, and process engineering*. Nano Energy, 2016, 29, 439-456. doi:10.1016/j.nanoen.2016.04.009

[20] Schouten, K. J., Kwon, Y., C. J. M. Van Der Ham, Qin, Z., Koper, M. T. *A new mechanism for the selectivity to C1 and C2 species in the electrochemical reduction of carbon dioxide on copper electrodes.* Chemical Science, 2011, 2(10), 1902. doi:10.1039/c1sc00277e

[21] Weinberg, D. R., Gagliardi, C. J., Hull, J. F., Murphy, C. F., Kent, C. A., Westlake, B., Meyer, T. J. *Proton-Coupled Electron Transfer.* Chemical Reviews, 2007, 107(11), 5004–5064. doi:10.1021/cr0500030

[22] Firet, N. J., Smith, W. A. *Probing the Reaction Mechanism of CO2 Electroreduction over Ag Films via Operando Infrared Spectroscopy.* ACS Catalysis, 2016, 7(1), 606-612. doi:10.1021/acscatal.6b02382

[23] Schouten, K. J., Qin, Z., Gallent, E. P., Koper, M. T. *Two Pathways for the Formation of Ethylene in CO Reduction on Single-Crystal Copper Electrodes.* Journal of the American Chemical Society, 2012, 134(24), 9864-9867. doi:10.1021/ja302668n

[24] Doyle, R. L., Lyons, M. E. *The Oxygen Evolution Reaction: Mechanistic Concepts and Catalyst Design.* Photoelectrochemical Solar Fuel Production, 2016, 41-104. doi:10.1007/978-3-319-29641-8_2

[25] *Nernst Equation.* Encyclopedia of Inorganic Chemistry, 2006, doi:10.1002/0470862106.id553

[26] Back, S., Yeom, M.S., Jung, Y. *Active Sites of Au and Ag Nanoparticle Catalysts for CO_2 Electroreduction to CO*. ACS Catalysis, 2015, 5(9). doi:10.1021/acscatal.5b00462

[27] Martin, A. J., Larrazabal, G. O., Perez-Ramirez, J. *Towards Sustainable Fuels and Chemicals Through the Electrochemical Reduction of CO2: Lessons from Water Electrolysis.* ChemInform, 2016, 47(7). doi:10.1002/chin.201607268

[28] Hori, Y., Wakebe, H., Tsukamoto, T., Koga, O. *Electrocatalytic process of CO selectivity in electrochemical reduction of CO2 at metal electrodes in aqueous media.* Electrochimica Acta, 1994, 39(11-12), 1833-1839. doi:10.1016/0013-4686(94)85172-7

[29] Li, C. W., Kanan, M. W. *CO2 Reduction at Low Overpotential on Cu Electrodes Resulting from the Reduction of Thick Cu2O Films.* Journal of the American Chemical Society, 2012, 134(17), 7231-7234. doi:10.1021/ja3010978

[30] Chen, Y., Kanan, M. W. *Tin Oxide Dependence of the CO2 Reduction Efficiency on Tin Electrodes and Enhanced Activity for Tin/Tin Oxide Thin-Film Catalysts.* Journal of the American Chemical Society, 2012, 134(4), 1986-1989. doi:10.1021/ja2108799

[31] Kuhl, K. P., Cave, E. R., Abram, D. N., Jaramillo, T. F. *New insights into the electrochemical reduction of carbon dioxide on metallic copper surfaces.* Energy & Environmental Science, 2012, 5(5), 7050. doi:10.1039/c2ee21234j

[32] Zhu, W., Michalsky, R., Metin, Ö, Lv, H., Guo, S., Wright, C., Sun, S. *Monodisperse Au Nanoparticles for Selective Electrocatalytic Reduction of CO2 to CO*. Journal of the American Chemical Society, 2013, 135(45), 16833-16836. doi:10.1021/ja409445p

[33] Gao, D., Zhou, H., Wang, J., Miao, S., Yang, F., Wang, G., Bao, X. *Size-Dependent Electrocatalytic Reduction of CO2 over Pd Nanoparticles*. Journal of the American Chemical Society, 2015, 137(13), 4288-4291. doi:10.1021/jacs.5b00046

[34] Kaneco, S., Iiba, K., Hiei, N., Ohta, K., Mizuno, T., Suzuki, T. *Electrochemical reduction of carbon dioxide to ethylene with high Faradaic efficiency at a Cu electrode in CsOH/methanol.* Electrochimica Acta, 1999, 44(26), 4701-4706. doi:10.1016/s0013-4686(99)00262-5

[35] Jhong, H., Ma, S., Kenis, P. J. *Electrochemical conversion of CO2 to useful chemicals: Current status, remaining challenges, and future opportunities.* Current Opinion in Chemical Engineering, 2013, 2(2), 191-199. doi:10.1016/j.coche.2013.03.005

[36] Centi, G., Perathoner, S., Win, G., Gangeri, M. *Electrocatalytic conversion of CO2 to long carbon-chain hydrocarbons.* Green Chemistry, 2007, 9(6), 671. doi:10.1039/b615275a

[37] Salvatore, D. A., Weekes, D. M., He, J., Dettelbach, K. E., Li, Y. C., Mallouk, T. E., Berlinguette, C. P. *Electrolysis of Gaseous CO2 to CO in a Flow Cell with a Bipolar Membrane.* ACS Energy Letters, 2017, 3(1), 149-154. doi:10.1021/acsenergylett.7b01017

[38] Endrődi, B., Bencsik, G., Darvas, F., Jones, R., Rajeshwar, K., Janáky, C. *Continuous-flow electroreduction of carbon dioxide.* Progress in Energy and Combustion Science, 2017, 62, 133-154. doi:10.1016/j.pecs.2017.05.005

[39] van de Krol, R., Grätzel, M., *Photo electrochemical hydrogen production*, Springer, 2011, 102, 321.

[40] Verma, S., Kim, B., Jhong, H., Ma, S., Kenis, P. J. *A Gross-Margin Model for Defining Technoeconomic Benchmarks in the Electroreduction of CO2.* ChemSusChem, 2016, 9(15), 1972-1979. doi:10.1002/cssc.201600394

[41] Salvatore, D. A., Weekes, D. M., He, J., Dettelbach, K. E., Li, Y. C., Mallouk, T. E., Berlinguette, C. P. *Electrolysis of Gaseous CO2 to CO in a Flow Cell with a Bipolar Membrane.* ACS Energy Letters, 2017, 3(1), 149-154. doi:10.1021/acsenergylett.7b01017

[42] *ElectroCell Instruction Manual – Micro Flow Cell.* ElectroCell Europe A/S, 2018. [Available on request at]: http://www.electrocell.com/contact/europe

[43] Endrődi, B., Bencsik, G., Darvas, F., Jones, R., Rajeshwar, K., Janáky, C. *Continuous-flow electroreduction of carbon dioxide.* Progress in Energy and Combustion Science, 2017, 62, 133-154. doi:10.1016/j.pecs.2017.05.005

[44] *fumasep® - ion exchange membranes for water treatment.* FumaTech BWT GmbH, [Online available at]: *http://www.fumatech.com/EN/Membranes/Water%2btreatment/Products%2bfumasep/index.html*

[45] Zeis, R. *Materials and characterization techniques for high-temperature polymer electrolyte membrane fuel cells.* Beilstein Journal of Nanotechnology, 2015, 6, 68–83. doi:10.3762/bjnano.6.8

[46] Gao, X., Lu, F., Liu, Y., Sun, N., Zheng, L. *The facile construction of an anion exchange membrane with 3D interconnected ionic nano-channels.* Chemical Communications, 2017, 53(4), 767-770. doi:10.1039/c6cc08730b

[47] Wilhelm, F. G. *Bipolar Membrane Electrodialysis - Membrane Development and Transport Characteristics*. University of Twente, 2001, Ph.D. thesis. [Online available at]: https://ris.utwente.nl/ws/portalfiles/portal/6074731

[48] Simons, R. *Preparation of a high performance bipolar membrane.* Journal of Membrane Science, 1993, 78(1-2), 13-23. doi:10.1016/0376-7388(93)85243-p

[49] Simons, R., Khanarian, G. *Water dissociation in bipolar membranes: Experiments and theory.* The Journal of Membrane Biology, 1978, 38(1-2), 11-30. doi:10.1007/bf01875160

[50] Bassignana, I., Reiss, H. *Ion transport and water dissociation in bipolar ion exchange membranes.* Journal of Membrane Science, 1983, 15(1), 27-41. doi:10.1016/s0376-7388(00)81360-5

[51] Strathmann, H., Rapp, H., Bauer, B., Bell, C. *Theoretical and practical aspects of preparing bipolar membranes.* Desalination, 1993, 90(1-3), 303-323. doi:10.1016/0011-9164(93)80183-n

[52] Frilette, V. J. *Preparation and Characterization of Bipolar Ion Exchange Membranes.* The Journal of Physical Chemistry, 1956, 60(4), 435-439. doi:10.1021/j150538a013

[53] Byszewski, C. H. *Reclaiming Waste Pickle Acid*. JOM, 1986 38(7), 61-61. doi:10.1007/bf03258720

[54] Yu, L., Guo, Q., Hao, J., Jiang, W. *Recovery of acetic acid from dilute wastewater by means of bipolar membrane electrodialysis.* Desalination, 2000, 129(3), 283-288. doi:10.1016/s0011-9164(00)00068-0

[55] Kassotis, J., Gregor, H. P., Chlanda, F. P. ChemInform Abstract: *Electrodialytic Water Splitting. Conversion of Dilute Sodium Acetate or Acetic Acid into Concentrated Acid*. Chemischer Informationsdienst, 1985, 16(14). doi:10.1002/chin.198514028

[56] Vargas-Barbosa, N. M., Geise, G. M., Hickner, M. A., Mallouk, T. E. *Assessing the Utility of Bipolar Membranes for use in Photoelectrochemical Water-Splitting Cells.* ChemSusChem, 2014, 7(11), 3017-3020. doi:10.1002/cssc.201402535

[57] Vermaas, D. A., Sassenburg, M., Smith, W. A. *Photo-assisted water splitting with bipolar membrane induced pH gradients for practical solar fuel devices.* Journal of Materials Chemistry A, 2015, 3(38), 19556-19562. doi:10.1039/c5ta06315a

[58] Lu, Q., Jiao, F. *Electrochemical* CO_2 *reduction: Electrocatalyst, reaction mechanism, and process engineering.* Nano Energy, 2016, 29, 439-456. doi:10.1016/j.nanoen.2016.04.009

[59] Turner, J., Sverdrup, G., Mann, M.K., Maness, P., Kroposki, B., Ghirardi, M., Evans, R.J., Blake, D. *Renewable hydrogen production*. International Journal of Energy Research, 2008, 32, 379-407. doi:10.1002/er.1372

[60] Verma, S., Hamasaki, Y., Kim, C., Huang, W., Lu, S., Jhong, H. M., Kenis, P. J. *Insights into the Low Overpotential Electroreduction of CO2 to CO on a Supported Gold Catalyst in an Alkaline Flow Electrolyzer.* ACS Energy Letters, 2017, 3(1), 193-198. doi:10.1021/acsenergylett.7b01096

[61] Park, G., Sohn, Y., Yang, T., Yoon, Y., Lee, W., Kim, C. *Effect of PTFE contents in the gas diffusion media on the performance of PEMFC.* Journal of Power Sources, 2004, 131(1-2), 182-187. doi:10.1016/j.jpowsour.2003.12.037

[62] Frey, T., & Linardi, M. *Effects of membrane electrode assembly preparation on the polymer electrolyte membrane fuel cell performance.* Electrochimica Acta, 2004, 50(1), 99-105. doi:10.1016/j.electacta.2004.07.017

[63] Park, J., Oh, H., Ha, T., Lee, Y. I., & Min, K. *A review of the gas diffusion layer in proton exchange membrane fuel cells: Durability and degradation.* Applied Energy, 2015, 155, 866-880. doi:10.1016/j.apenergy.2015.06.068

[64] Jhong, H., Ma, S., Kenis, P. J. *Electrochemical conversion of CO2 to useful chemicals: Current status, remaining challenges, and future opportunities.* Current Opinion in Chemical Engineering, 2013, 2(2), 191-199. doi:10.1016/j.coche.2013.03.005

[65] Kim, B., Hillman, F., Ariyoshi, M., Fujikawa, S., Kenis, P. J. Effects of composition of the micro porous layer and the substrate on performance in the electrochemical reduction of CO_2 to CO. Journal of Power Sources, 2016, 312, 192-198. doi:10.1016/j.jpowsour.2016.02.043

[66] Salvatore, D. A., Weekes, D. M., He, J., Dettelbach, K. E., Li, Y. C., Mallouk, T. E., Berlinguette, C. P. *Electrolysis of Gaseous CO2 to CO in a Flow Cell with a Bipolar Membrane.* ACS Energy Letters, 2017, 3(1), 149-154. doi:10.1021/acsenergylett.7b01017

[67] Schweiss, R., Meiser, C., Damjanovic, T. Galbati, I., Haak, N. *Sigracet® Gas Diffusion Layer for PEM Fuel Cells, Electrolyzers and Batteries.* White Paper by SGL CARBON GmbH, 2016.

[Online available at]: http://www.sglgroup.com/cms/_common/downloads/products/product-groups/su/fuel-cell-components/White-Paper-SIGRACET-GDL-for-Fuel-Cells.pdf

[68] *Parstat 4000 Brochure and specifications.* Princeton Applied Research, 2018. [Online available at]: https://www.unr.edu/Documents/research/ncar/SRF/MCN/PARSTAT-4000-A4.pdf

[69] Cook, R. L., MacDuff, R.C., Sammells, A.F. *High Rate Gas Phase CO_2 Reduction to Ethylene and Methane Using Gas Diffusion Electrodes.* Journal of The Electrochemical Society, 1990, 137(2), 607. doi:10.1149/1.2086515

[70] Vico, F., Mogensen, M. B., Chatzichristodoulou, C., Holtappels, P. *Searching for electrolytes and electrodes for CO_2 reduction below 300 °C.* Department of Energy Conversion and Storage, Technical University of Denmark, 2015. [Online available at]: http://orbit.dtu.dk/files/115359089/Searching_for_electrolytes.pdf

[71] Kwon, K., Park, J., Lee, C.K., Kim, H. *Stability of Ni and Ti in Hydrogen Evolution in the Presence of 1-Butyl-3-methylimidazolium Tetrafluoroborate.* International Journal of the Electrochemical Society, 2012, 7, 9835-9843.

[72] *Technical Data Sheet fumasep® FBM*. Fuel Cell Store, 2018. [Online available at]: http://www.fuelcellstore.com/spec-sheets/fumasep-fbm-pk-technical-specifications.pdf

9. Appendix

A. Technical Data on ElectroCell devices

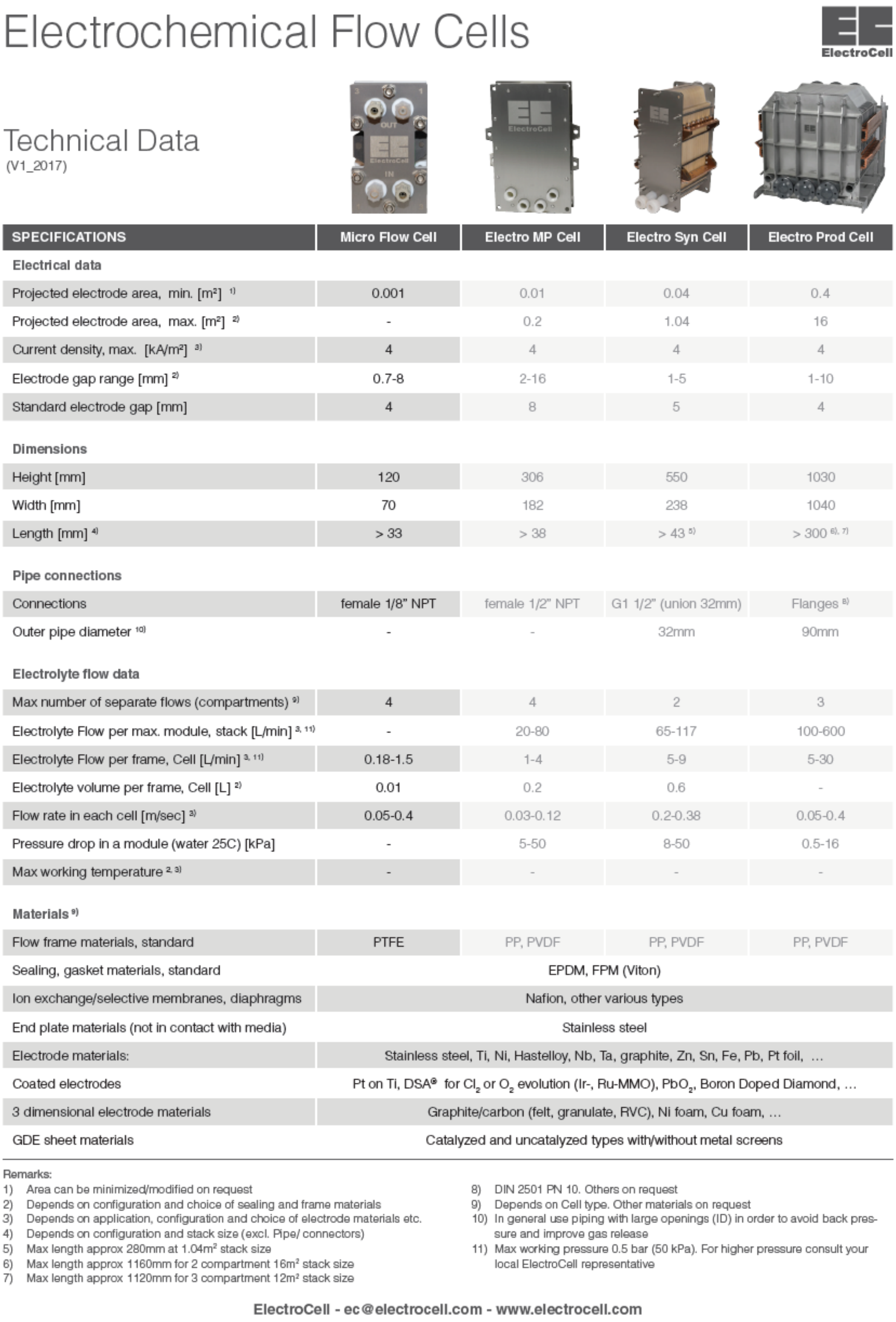

Electrochemical Flow Cells

Technical Data

(V1_2017)

SPECIFICATIONS	Micro Flow Cell	Electro MP Cell	Electro Syn Cell	Electro Prod Cell
Electrical data				
Projected electrode area, min. [m^2] 1)	0.001	0.01	0.04	0.4
Projected electrode area, max. [m^2] 2)	-	0.2	1.04	16
Current density, max. [kA/m^2] 3)	4	4	4	4
Electrode gap range [mm] 2)	0.7-8	2-16	1-5	1-10
Standard electrode gap [mm]	4	8	5	4
Dimensions				
Height [mm]	120	306	550	1030
Width [mm]	70	182	238	1040
Length [mm] 4)	> 33	> 38	> 43 5)	> 300 6), 7)
Pipe connections				
Connections	female 1/8" NPT	female 1/2" NPT	G1 1/2" (union 32mm)	Flanges 8)
Outer pipe diameter 10)	-	-	32mm	90mm
Electrolyte flow data				
Max number of separate flows (compartments) 9)	4	4	2	3
Electrolyte Flow per max. module, stack [L/min] 3, 11)	-	20-80	65-117	100-600
Electrolyte Flow per frame, Cell [L/min] 3, 11)	0.18-1.5	1-4	5-9	5-30
Electrolyte volume per frame, Cell [L] 2)	0.01	0.2	0.6	-
Flow rate in each cell [m/sec] 3)	0.05-0.4	0.03-0.12	0.2-0.38	0.05-0.4
Pressure drop in a module (water 25C) [kPa]	-	5-50	8-50	0.5-16
Max working temperature 2, 3)	-	-	-	-
Materials 9)				
Flow frame materials, standard	PTFE	PP, PVDF	PP, PVDF	PP, PVDF
Sealing, gasket materials, standard	EPDM, FPM (Viton)			
Ion exchange/selective membranes, diaphragms	Nafion, other various types			
End plate materials (not in contact with media)	Stainless steel			
Electrode materials:	Stainless steel, Ti, Ni, Hastelloy, Nb, Ta, graphite, Zn, Sn, Fe, Pb, Pt foil, …			
Coated electrodes	Pt on Ti, DSA® for Cl_2 or O_2 evolution (Ir-, Ru-MMO), PbO_2, Boron Doped Diamond, …			
3 dimensional electrode materials	Graphite/carbon (felt, granulate, RVC), Ni foam, Cu foam, …			
GDE sheet materials	Catalyzed and uncatalyzed types with/without metal screens			

Remarks:

1) Area can be minimized/modified on request
2) Depends on configuration and choice of sealing and frame materials
3) Depends on application, configuration and choice of electrode materials etc.
4) Depends on configuration and stack size (excl. Pipe/ connectors)
5) Max length approx 280mm at 1.04m² stack size
6) Max length approx 1160mm for 2 compartment 16m² stack size
7) Max length approx 1120mm for 3 compartment 12m² stack size
8) DIN 2501 PN 10. Others on request
9) Depends on Cell type. Other materials on request
10) In general use piping with large openings (ID) in order to avoid back pressure and improve gas release
11) Max working pressure 0.5 bar (50 kPa). For higher pressure consult your local ElectroCell representative

ElectroCell - ec@electrocell.com - www.electrocell.com

B. Product details on the BPM, GDL and Ag-mesh

Bipolar membrane [72]:

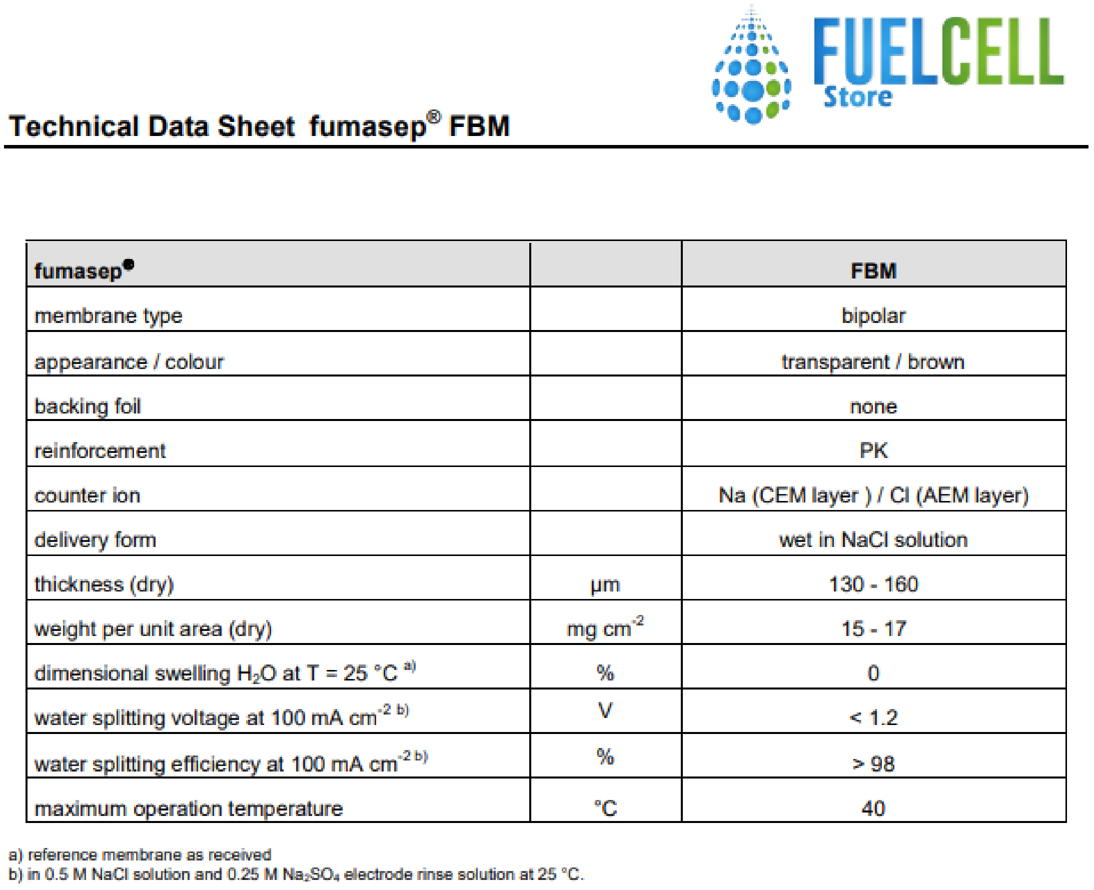

Technical Data Sheet fumasep® FBM

fumasep®		**FBM**
membrane type		bipolar
appearance / colour		transparent / brown
backing foil		none
reinforcement		PK
counter ion		Na (CEM layer) / Cl (AEM layer)
delivery form		wet in NaCl solution
thickness (dry)	µm	130 - 160
weight per unit area (dry)	mg cm^{-2}	15 - 17
dimensional swelling H_2O at T = 25 °C [a)]	%	0
water splitting voltage at 100 mA cm^{-2} [b)]	V	< 1.2
water splitting efficiency at 100 mA cm^{-2} [b)]	%	> 98
maximum operation temperature	°C	40

a) reference membrane as received
b) in 0.5 M NaCl solution and 0.25 M Na_2SO_4 electrode rinse solution at 25 °C.

Gas diffusion layer [67]:

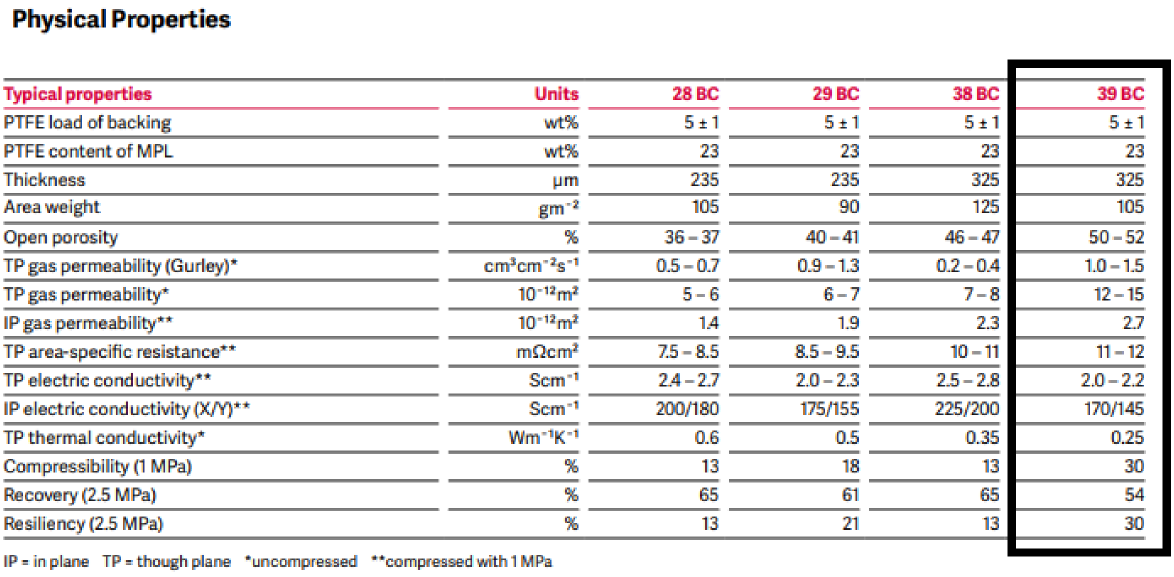

Physical Properties

Typical properties	Units	28 BC	29 BC	38 BC	39 BC
PTFE load of backing	wt%	5 ± 1	5 ± 1	5 ± 1	5 ± 1
PTFE content of MPL	wt%	23	23	23	23
Thickness	µm	235	235	325	325
Area weight	gm^{-2}	105	90	125	105
Open porosity	%	36 – 37	40 – 41	46 – 47	50 – 52
TP gas permeability (Gurley)*	$cm^3cm^{-2}s^{-1}$	0.5 – 0.7	0.9 – 1.3	0.2 – 0.4	1.0 – 1.5
TP gas permeability*	$10^{-12}m^2$	5 – 6	6 – 7	7 – 8	12 – 15
IP gas permeability**	$10^{-12}m^2$	1.4	1.9	2.3	2.7
TP area-specific resistance**	$m\Omega cm^2$	7.5 – 8.5	8.5 – 9.5	10 – 11	11 – 12
TP electric conductivity**	Scm^{-1}	2.4 – 2.7	2.0 – 2.3	2.5 – 2.8	2.0 – 2.2
IP electric conductivity (X/Y)**	Scm^{-1}	200/180	175/155	225/200	170/145
TP thermal conductivity*	$Wm^{-1}K^{-1}$	0.6	0.5	0.35	0.25
Compressibility (1 MPa)	%	13	18	13	30
Recovery (2.5 MPa)	%	65	61	65	54
Resiliency (2.5 MPa)	%	13	21	13	30

IP = in plane TP = though plane *uncompressed **compressed with 1 MPa

SEM images of the Sigracet 39BC (similar to the GDL shown in fig. 13):

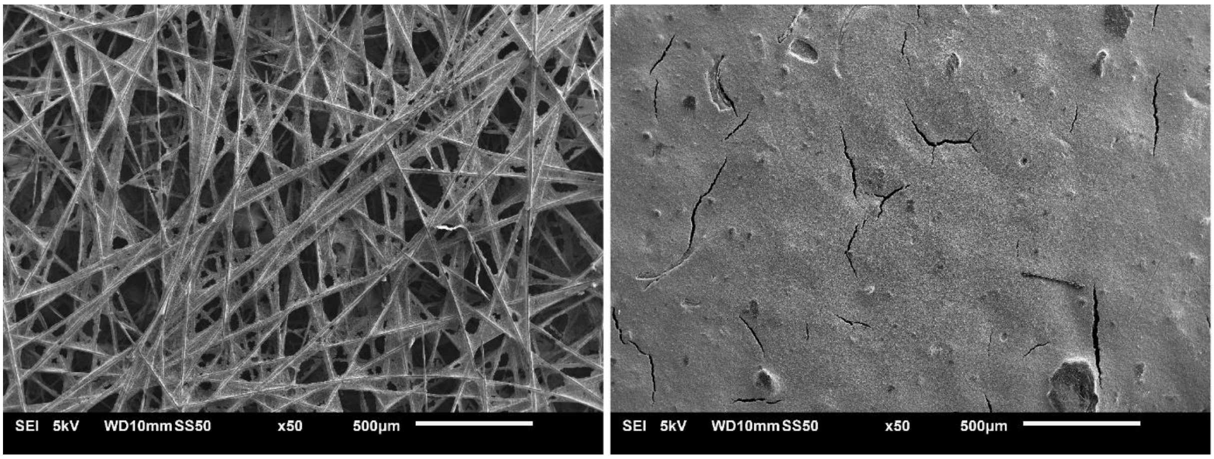

Ag-mesh by MaTeck:

Silver Gauze

Product No.:	900082-1
CAS	7440-22-4
Size	1024 mesh/cm², 0.12 mm wire diameter
purity	99.9%
Quantity	50 x 50 mm
Art. No.	900082-1

According to the size and wire diameter the surface area can be calculated. In order to do so the mesh quantity can be converted to the amount of wires in horizontal and vertical directions:

$$\sqrt{1024\ mesh/cm^2} = 32\ wires/cm$$

To calculate the fraction of planar surface area or the total area, the fraction covered per cm^2 is calculated as such:

$$A_{wire/cm^2} = A_{horizontal} + A_{vertical} - A_{crosssection}$$

$$A_{wire/cm^2} = 32 * 0.012\ cm * 1\ cm + 32 * 0.012\ cm * 1\ cm - (32)^2(0.012\ cm)^2$$

$$A_{wire/cm^2} = 0.384\ cm^2 + 0.384\ cm^2 - 0.147\ cm^2 = 0.621\ cm^2$$

The percentage of planar surface area of the Ag-mesh is therefore 62.1%, or in other words, its porosity is 37.9%.